PUBLICATIONS RELATED TO THESIS A

A.1 KINETICALLY DISTINCT PHASES OF TAU ON MICROTUBULES REGULATE KINESIN MOTORS AND SEVERING ENZYMES

Siahaan, V.*, Krattenmacher, J.*, Hyman, A.A., Diez, S., Hernández-Vega, A., Lansky, Z., Braun, M. Kinetically distinct phases of tau on microtubules regulate kinesin motors and severing enzymes. *Nat Cell Biol* 21, 1086–1092 (2019).

*These authors contributed equally.

Contributions as stated in the article:

A.H.-V. and M.B. first observed the islands and initiated the project; A.H.-V., A.A.H., S.D., Z.L. and M.B. conceived the experiments; A.H.-V. generated the tau(ΔN)–meGFP construct; V.S., J.K., A.H.-V. and M.B. generated the proteins, performed and analysed the experiments and V.S., J.K., S.D., Z.L. and M.B. wrote the manuscript. All authors discussed the results and commented on the manuscript.

In detail: V.S. optimized the methods and performed all experiments of figures 1 and 2, part of figure 3 (specifically, multiple repeats from 3a and 3b were performed by V.S.), part of figure 4 (specifically 4a and 4b were optimized and performed by V.S.), and all experiments of figure 5. All experiments were performed using TIRF microscopy. All of the analysis was optimized and carried out by J.K., with help from V.S. All analysis was done using ImageJ, Excel, and Matlab. Tau-GFP, tau-mCherry, and katanin-GFP constructs were generated by V.S. with help from J.K. The manuscript was written by V.S., J.K., S.D., Z.L. and M.B.

LETTERS
https://doi.org/10.1038/s41556-019-0374-6

nature cell biology

Kinetically distinct phases of tau on microtubules regulate kinesin motors and severing enzymes

Valerie Siahaan[1,5], Jochen Krattenmacher[1,5], Anthony A. Hyman[2,3,6], Stefan Diez[2,3,4,6], Amayra Hernández-Vega[2,6*], Zdenek Lansky[1,6*] and Marcus Braun[1,4,6*]

Tau is an intrinsically disordered protein, which diffuses on microtubules[1]. In neurodegenerative diseases, collectively termed tauopathies, malfunction of tau and its detachment from axonal microtubules are correlated with axonal degeneration[2]. Tau can protect microtubules from microtubule-degrading enzymes such as katanin[3]. However, how tau carries out this regulatory function is still unclear. Here, using in vitro reconstitution, we show that tau molecules on microtubules cooperatively form cohesive islands that are kinetically distinct from tau molecules that individually diffuse on microtubules. Dependent on the tau concentration in solution, the islands reversibly grow or shrink by addition or release of tau molecules at their boundaries. Shielding microtubules from kinesin-1 motors and katanin, the islands exhibit regulatory qualities distinct from a comparably dense layer of diffusible tau. Superprocessive kinesin-8 motors penetrate the islands and cause their disassembly. Our results reveal a microtubule-dependent phase of tau that constitutes an adaptable protective layer on the microtubule surface. We anticipate that other intrinsically disordered axonal proteins display a similar cooperative behaviour and potentially compete with tau in regulating access to the microtubule surface.

Tau is an intrinsically disordered microtubule-associated protein (MAP), which localizes preferentially to neuronal axons and is involved in neurodegenerative diseases[4–6]. Tau enhances the stability of microtubules directly by its presence[7], and by regulating the interactions of other MAPs with microtubules[8–13]. Tau mislocalization during the onset of Alzheimer's disease leaves axonal microtubules unprotected against microtubule-severing enzymes such as katanin[3], leading to microtubule destabilization and the eventual degeneration of the axon. The molecular mechanism underlying this regulatory function of tau is unknown. Here we demonstrate how microtubule-associated tau molecules can collectively regulate molecular motors and severing enzymes.

To study microtubule-associated tau molecules, we immobilized Atto 647-labelled microtubules on a coverslip, added full-length, human tau 441 isoform (encoded by 2N4R), fluorescently labelled on the C terminus with either monomeric enhanced green fluorescent protein (tau–meGFP) or mCherry (tau–mCherry) and performed time-lapse imaging using total internal reflection fluorescence (TIRF) microscopy (Fig. 1a and Methods). After the addition of 20 nM tau–meGFP, we observed the formation of high-density tau–meGFP islands on the microtubules, surrounded by regions of low-density tau–meGFP (Fig. 1b–d and Supplementary Video 1). Tau–meGFP islands originated from diffraction-limited spots, appearing within tens of seconds after the addition of tau (Supplementary Fig. 1a). The islands grew intermittently at their boundaries with variable velocities in the order of 25 nm s^{-1}, corresponding to about 10 molecules added per s (Supplementary Fig. 1b) to highly variable lengths (Supplementary Fig. 1c), progressively covering the microtubules (Fig. 1e and Supplementary Fig. 1d). During experimentally accessible time scales (approximately 1 h), island growth did not cease (Supplementary Fig. 1e). Notably, the tau density in the islands stayed constant during the period of growth (Fig. 1f and Supplementary Fig. 1f), suggesting that the islands grow by the addition of tau molecules at their boundaries, reminiscent of epitaxial growth of thin films. When the boundaries of neighbouring growing islands came into contact, the islands merged (Fig. 1c). At these instances, we never observed an increase in the tau density, suggesting that islands are formed by a well-defined tau layer occupying the entire accessible surface of the microtubule. When tau was removed from solution (Fig. 1g and Supplementary Video 2), tau molecules unbound rapidly and uniformly from all regions outside of islands (the 'island surroundings'), with a time constant of about 2 s, as inferred from the decay of the fluorescence signal (Fig. 1h, Supplementary Fig. 1g and Methods). By contrast, islands prevailed over several minutes, without substantial changes in the initial tau density, while slowly disassembling from their boundaries until they fully disappeared (Fig. 1g,h and Supplementary Fig. 1f). The island boundaries receded with an average velocity of approximately two tau molecules unbinding per second (Supplementary Fig. 1h and Methods). During disassembly, the islands occasionally underwent fission (Supplementary Fig. 1i). In contrast to the fast unbinding of tau from outside the islands, tau molecules unbound from the disassembling islands orders of magnitude slower—on the timescale of tens of minutes (Fig. 1h, Supplementary Fig. 1g and Methods). This extremely low unbinding rate explains the preservation of the islands in the absence of tau in solution and suggests that the occasional island fissions observed during disassembly occur after rare events of tau molecules unbinding from inside the island. Islands thus predominantly disassemble at their boundaries. The marked difference in the tau-unbinding rates inside and outside the islands, together with the assembly and disassembly kinetics at the island boundaries, strongly suggest that tau molecules in the islands cooperate, forming a cohesive layer on the microtubule surface. Because the N terminus of tau mediates

[1]Institute of Biotechnology of the Czech Academy of Sciences, BIOCEV, Prague West, Czech Republic. [2]Max Planck Institute of Molecular Cell Biology and Genetics, Dresden, Germany. [3]Cluster of Excellence Physics of Life, Technische Universität Dresden, Dresden, Germany. [4]B CUBE—Center for Molecular Bioengineering, Technische Universität Dresden, Dresden, Germany. [5]These authors contributed equally: Valerie Siahaan, Jochen Krattenmacher. [6]These authors jointly supervised this work: Anthony A. Hyman, Stefan Diez, Amayra Hernández-Vega, Zdenek Lansky, Marcus Braun. *e-mail: hernande@mpicbg.de; zdenek.lansky@ibt.cas.cz; marcus.braun@ibt.cas.cz

tau–tau interactions[14], we repeated the experiments using a tau construct with a truncated N terminus (tau(ΔN)–meGFP; Supplementary Fig. 1j). Although tau(ΔN)–meGFP interacted with the microtubules, we did not observe any island formation even at tau(ΔN)–meGFP concentrations as high as 0.5 µM. Combined, these results show that full-length tau on microtubules can separate into two kinetically distinct phases, islands of high-density tau with slow turnover surrounded by regions of low-density tau with rapid turnover. Similar observations are reported in a complementary study by Tan et al.[15].

To investigate the dynamics of tau molecules in the islands, we incubated microtubules with 20 nM tau–mCherry and, after 15 min of incubation, replaced the assay buffer with a solution containing 20 nM tau–meGFP (Fig. 2a, Supplementary Fig. 2a and Supplementary Video 3). Tau–meGFP molecules exchanging with the leaving tau–mCherry, bound rapidly to the regions surrounding the islands, while binding with a slower time constant into the islands. In both islands and their surroundings, the turnover from tau–mCherry to tau–meGFP occurred without any positional preferences. Outside the islands, tau–mCherry rapidly dissociated from the microtubules with a time constant of about 3 s, comparable to the value estimated above when tau–meGFP was removed from solution (Supplementary Fig. 2b). Inside the islands, tau–mCherry dissociated with a time constant of about 20 s (Fig. 2b and Supplementary Fig. 2b), which, although an order of magnitude slower than outside the islands, was nevertheless substantially faster than the approximately 1,300 s measured in the absence of tau–meGFP in solution (Fig. 2b). At higher tau concentration (100 nM), we observed a further decrease in the time constant of tau–mCherry unbinding from the islands by about twofold, demonstrating that tau unbinding from the islands depends on the tau concentration in solution (Fig. 2b, Supplementary Fig. 2c and Methods). We did not observe such a trend in the low-density regions (Supplementary Fig. 2d).

To study the spatio-temporal dynamics of tau, we formed islands using a mixture of 20 nM tau–mCherry and 1 nM tau–meGFP, enabling us to observe the motion of individual tau–meGFP particles in an environment dominated by tau–mCherry (Fig. 2c). Fluorescence-intensity histograms of individual tau–meGFP particles has a single-Gaussian profile showing that tau–meGFP was incorporated in the islands as single molecules, highlighting that tau–tau interactions occurred only on the microtubule lattice (Supplementary Fig. 2e). Outside the islands, single tau–meGFP molecules diffused rapidly with a diffusion constant of $0.27 \pm 0.15\,\mu m^2 s^{-1}$ (linear fit coefficient ± 95% confidence bounds, Fig. 2c, Supplementary Fig. 2f and Methods), comparable to previously reported values[1]. By contrast, the tau–meGFP molecules in the islands were stationary, with a negligible diffusion constant of $0.027 \pm 0.016\,\mu m^2 s^{-1}$ (linear fit coefficient ± 95% confidence bounds, Fig. 2c and Supplementary Fig. 2f). Occasionally, single tau–meGFP molecules initially diffusing outside an island became

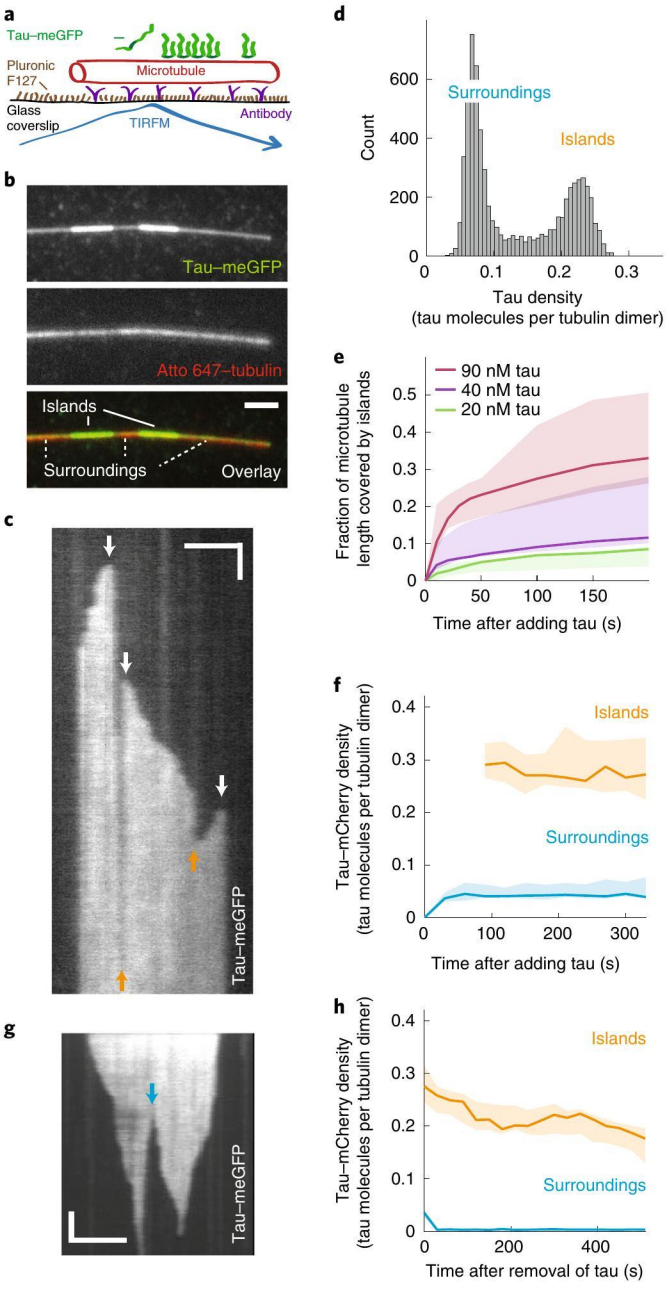

Fig. 1 | Tau on microtubules separates into two kinetically distinct phases. **a**, Schematics depicting the assay geometry. **b**, Multichannel fluorescence micrograph showing islands of high-density tau–meGFP (bright green) surrounded by regions of low-density tau–meGFP (less intense green) on an Atto 647-labelled microtubule (red). Images taken 5 min after the addition of 20 nM tau–meGFP. **c**, Kymograph showing the fluorescence signal of tau–meGFP on a microtubule after the addition 20 nM tau–meGFP. Initially, the microtubule is covered by low tau–meGFP density. Over time, high-density tau–meGFP islands start to assemble. White arrows indicate positions of nucleation. Orange arrows indicate the merging of neighbouring islands growing towards each other. **d**, Distribution of fluorescence intensity of tau–meGFP along microtubules such as the one shown in **c**, showing two distinct populations. **e**, Fraction of microtubule length covered by tau islands after the addition of tau–meGFP ($n = 3$ experiments per condition, 131 microtubules). For statistics calculated over individual microtubules, see Supplementary Fig. 1d. **f**, Example time trace of the tau–mCherry density in the islands and their surroundings (Methods) after the addition of tau–mCherry ($n = 5$ microtubules). The tau–mCherry density within the islands was constant during the experiment. For quantification, see Supplementary Fig. 1f. **g**, Kymograph showing the fluorescence signal of tau–meGFP on the microtubule after the removal of tau–meGFP from solution, visualizing island disassembly. The blue arrow indicates a fission event. **h**, Example time trace of the tau–mCherry density inside and outside the islands after the removal of tau–mCherry from solution ($n = 9$ microtubules). Unbinding rates outside and inside the islands markedly differed and were in the order of seconds and tens of minutes, respectively (for quantification see Fig. 2b and Supplementary Figs. 1g and 2d). Experiments in **g** and **h** were performed with reduced framerate to minimize photobleaching (Methods). Experiments were repeated independently 438 (**b**), 343 (**c**,**d**), 22 (**f**), 115 (**g**) and 16 (**h**) times with similar results. In **e**, thick lines show the median and shaded areas indicate the full range of values; in **f** and **h**, thick lines show the median and shaded areas indicate the range between first and third quartiles. All scale bars, vertical 5 s, horizontal 2 µm.

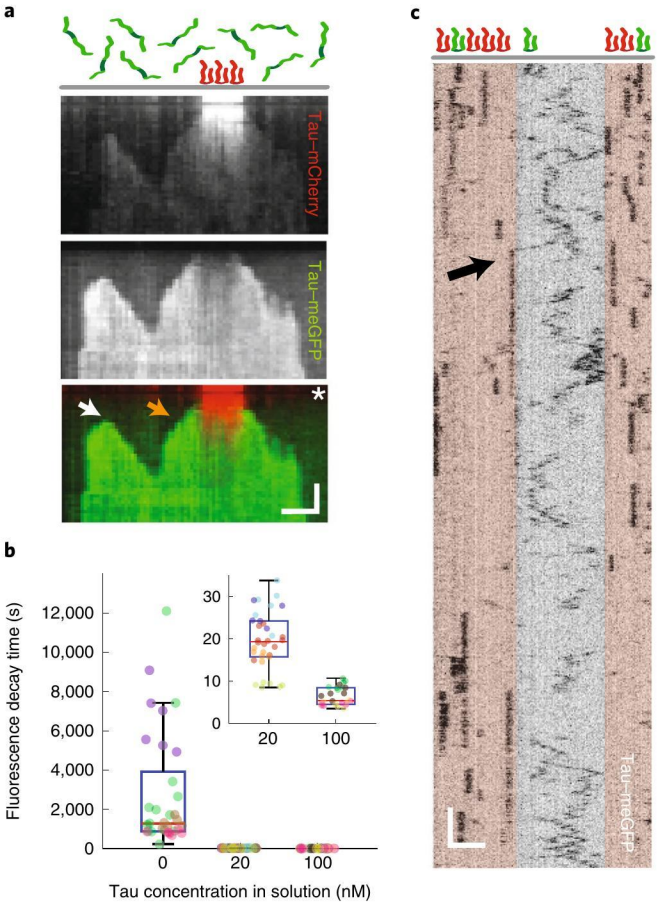

Fig. 2 | Tau molecules in the islands are stationary but exchange with tau in solution. a, Multichannel kymograph showing an island pre-formed in the presence of 20 nM tau-mCherry (red). After removing most of the tau-mCherry from solution by adding of 20 nM tau-meGFP (green; time of addition marked by white asterisk), we observed the exchange of tau-mCherry for tau-meGFP inside and outside of the islands. This exchange occurred along the entire length of the islands. Additionally, islands resumed their growth with the addition of tau-meGFP to their boundaries (an example is marked by an orange arrow). New islands also started to assemble (an example is marked by a white arrow). Scale bars: vertical 20 s, horizontal 2 µm. This experiment was repeated 15 times with similar results. **b**, The dwell time of fluorescently labelled tau in the islands decreases with increasing concentration of tau in solution (0 nM tau: dwell time 45 ± 46 min (mean ± s.d.), $n = 33$ microtubules in 4 experiments; 20 nM tau: dwell time 20 ± 7 s (mean ± s.d., $n = 34$ microtubules in 5 experiments; 100 nM tau: dwell time 6.4 ± 2.1 s (mean ± s.d.), $n = 26$ microtubules in 4 experiments). The inset shows the 20 nM and 100 nM boxes on a magnified *y* scale. The data points are colour-coded by experiments. Typical time traces and corresponding fits underlying these data are shown in Supplementary Figs. 1g, 2b,c. For a description of all box-plot elements see Methods. **c**, Intensity-inverted kymograph showing single tau-meGFP molecules interacting with a microtubule containing two tau-mCherry islands (indicated by beige transparent boxes). Outside the islands, tau-meGFP diffuses rapidly, whereas inside the islands, tau-meGFP is stationary. Occasionally, we observed a diffusing tau-meGFP molecule stopping as it associated with an island (black arrow). Scale bars: vertical 1 s, horizontal 2 µm. This experiment was repeated 65 times with similar results.

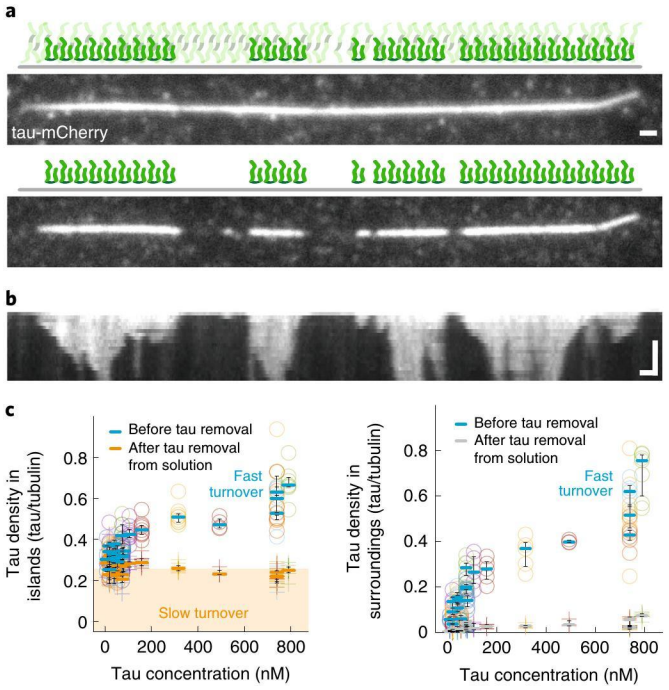

Fig. 3 | Tau islands are characterized by tau cohesion. a, Fluorescence micrographs showing the coverage of a microtubule by tau-mCherry. Top: uniform coverage at high (0.8 µM) concentration 5 min after the addition of tau-mCherry. Bottom: islands, 30 s after the removal of tau-mCherry from solution. This experiment was repeated 17 times with similar results. **b**, Kymograph of the experiment presented in **a**, showing the disassembly of the islands after the removal of tau-mCherry from solution. **c**, Tau densities in regions covered by islands and the surrounding regions established at various tau-meGFP concentrations, before and after the removal of tau-meGFP from solution ($n = 150$ microtubules, 21 experiments). Points are colour-coded by experiment, horizontal lines indicate the three quartiles of each experiment. The characteristic island density (main text, Methods) is indicated by the height of the shaded area (left panel). Scale bars: vertical 5 min, horizontal 1 µm.

stationary when associating with an island boundary (Fig. 2c). We conclude that the tau molecules localizing in the islands are stationary; nevertheless, as demonstrated above in bulk experiments (Fig. 2b) they can exchange with tau in solution.

To investigate the dependence of island formation on the concentration of tau, we performed experiments with repeated cycles of microtubule incubation with increasing concentrations of tau–meGFP followed by tau–meGFP removal from solution. Below a tau–meGFP concentration of approximately 5 nM, we did not observe any island formation ($n = 245$ microtubules in five experiments). Above this concentration, the tau–meGFP density outside and inside the islands increased with increasing tau–meGFP concentration in solution. After each removal of tau–meGFP, the tau density in the regions surrounding the islands returned to the background level within several seconds (Supplementary Fig. 3a; consistent with the data shown in Fig. 1h). By contrast, after each removal of tau–meGFP, the tau density in the islands decayed in two stages: within a few seconds, a fast density drop occurred uniformly along the whole length of the islands, followed by a slow density decrease, the latter consistent with the data shown in Fig. 1h (Supplementary Fig. 3a). Above a tau–meGFP concentration of approximately 0.5 µM, the tau density on the microtubules reached saturation (Supplementary Fig. 3b), as previously reported[16], suggesting that tau associates with a finite number of interaction sites on the microtubule. In this regime, the islands became apparent only after tau–meGFP was removed from solution, following which tau–meGFP rapidly unbound from the surroundings and islands became discernable (Fig. 3a,b). Of note, in all experiments, the tau–meGFP

density in the islands, after the fast density drop, had the same value of 0.26 ± 0.05 tau molecules per tubulin dimer (mean ± s.d., $n = 101$ microtubules, 14 experiments; Methods), independent of the initial tau concentration in solution (Fig. 3c). Together with the results in Figs. 1 and 2, these experiments show that cohesive islands on microtubules are formed by tau molecules that bind cooperatively and, consequently, turn over slowly. At physiological tau concentrations[17] in the range of 0.5–1.5 µM, tau molecules, which turn over rapidly, co-localize with islands. These tau molecules, whose density depends on the tau concentration in solution in a similar way as the tau density outside the islands (Supplementary Fig. 3c), do not appear to participate in the cooperative island formation.

To investigate how the tau islands may regulate the interaction of other MAPs with microtubules, we formed tau islands using tau–mCherry and tested their effect on GFP-tagged MAPs. First, we tested the molecular motor kinesin-1. After addition of 60 nM kinesin-1–GFP (Methods) to microtubules in the presence of tau–mCherry, we observed processive movement of single motors outside the islands (Fig. 4a and Supplementary Fig. 4a,b). On reaching the island boundaries, the motors dissociated instantaneously from the microtubules (Fig. 4a), similar to previous observations of kinesin-1 encountering static obstacles[18,19]. The kinesin-1 landing rate in the islands was about an order of magnitude lower than in their surroundings (Supplementary Fig. 4c). Notably, at all studied tau concentrations, no kinesin-1 molecules landing inside an island moved processively (total number of 553 molecules in 23 experiments); instead, these transient interactions were static. Second, we tested the microtubule-severing enzyme katanin. After the addition of 200 nM katanin–GFP (subunits p60 and p80[20]) to microtubules in the presence of 20 nM tau–mCherry, we observed katanin–GFP binding and microtubule severing predominantly outside the islands, leading to the disintegration of these microtubule regions (Fig. 4b, Supplementary Fig. 4d and Supplementary Video 4), while island-covered regions prevailed. On longer time scales, the island-covered regions of the microtubules started to disassemble slowly from their boundaries, with only occasional isolated cut observed in the island-covered microtubules (Fig. 4b, Supplementary Fig. 4e and Supplementary Video 4). Whereas non-island microtubule regions disassembled within 1 min, the island-protected microtubule stretches persisted on the timescale of tens of minutes. Third, we tested the effect of the tau islands on superprocessive motors. We used *Saccharomyces cerevisiae* Kip3, the best described member of the kinesin-8 family. Unlike kinesin-1[18,19], Kip3 does not dissociate from the microtubule when the next binding site ahead is occupied, but rather pauses for extended periods of time[21], leading to the formation of 'traffic jams'[22]. As the kinesin- and tau- interaction sites on microtubules overlap[23], we hypothesized that traffic jams might form in front of tau islands. We formed islands using 20 nM or 100 nM tau–mCherry. After the addition of 15 nM Kip3–GFP, we observed Kip3–GFP molecules moving in the low-density tau regions. In contrast to kinesin-1, we also detected Kip3–GFP motility inside the tau islands, albeit at decreased velocity and

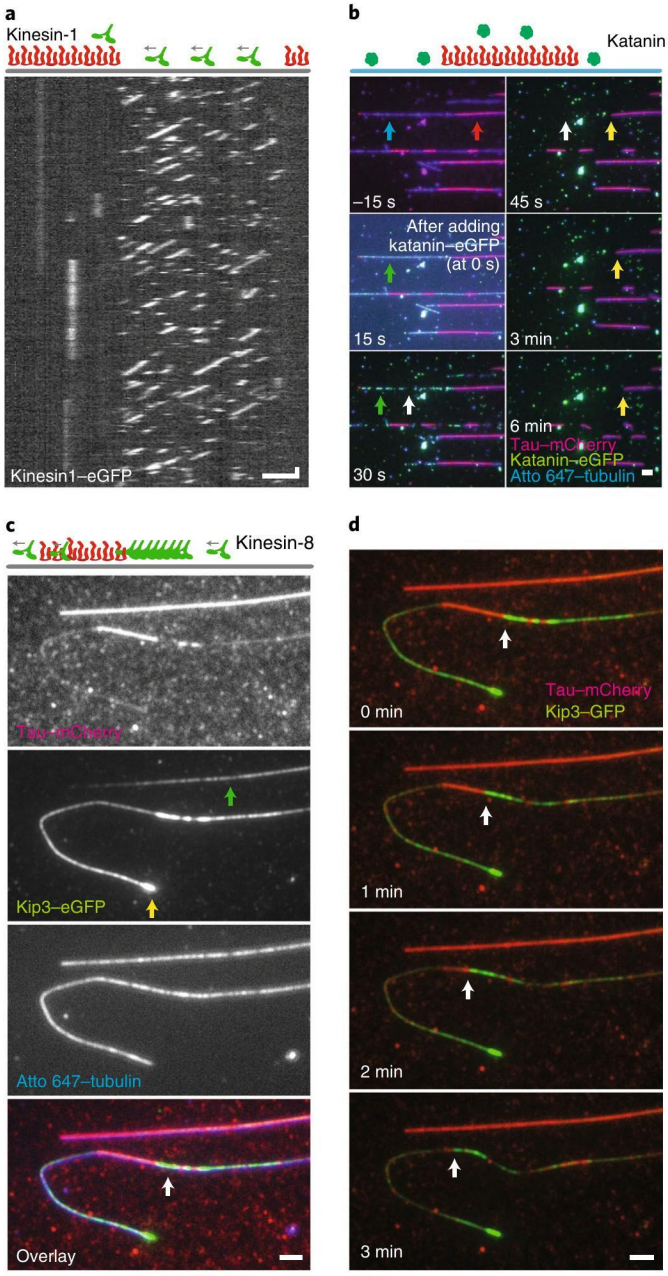

Fig. 4 | Tau islands constitute a protective layer around microtubules. **a**, Fluorescence kymograph showing kinesin-1-GFP molecules moving processively outside the islands and immediately dissociating from the microtubule when reaching the island boundaries (island positions indicated by schematics above the kymograph). No kinesin-1-GFP molecules moved processively inside the islands. This experiment was repeated 124 times with similar results. For quantification of the kinesin-1-GFP landing rates inside and outside the islands, and velocities and dwell times outside the islands at different tau concentrations, see Supplementary Fig. 4a–c. **b**, Multichannel fluorescence micrographs showing katanin-GFP-driven (green, example position indicated by green arrow) severing of Atto 647 microtubules (blue) decorated with tau-mCherry islands (red, example indicated by red arrow) interspersed by regions of low tau-meGFP density (indicated by blue arrow). Katanin-GFP was added at time = 0 s. Initially, microtubule severing and disassembly occurred only in the regions surrounding the islands (example indicated by white arrow). On longer time scales katanin-GFP induced shortening of the island-covered regions of the microtubule (example indicated by yellow arrow). This experiment was repeated 11 times with similar results. **c**, Multichannel fluorescence micrographs showing that Kip3-GFP (kinesin-8, green) localizes both outside and inside the tau-mCherry (red) islands (exemplary localization of Kip3-GFP in the island indicated by green arrow) on Atto 647-labelled microtubules (blue) and accumulates at the microtubule ends (yellow arrow) and in front of the islands (white arrow). This experiment was repeated seven times with similar results. **d**, Multichannel fluorescence micrographs showing that Kip3-GFP (green) accumulating in front of a tau-mCherry island (red) can remove the island by displacing tau-mCherry from the island edge (receding of the island boundary indicated by white arrow). Scale bars: vertical 1 s, horizontal 2 µm.

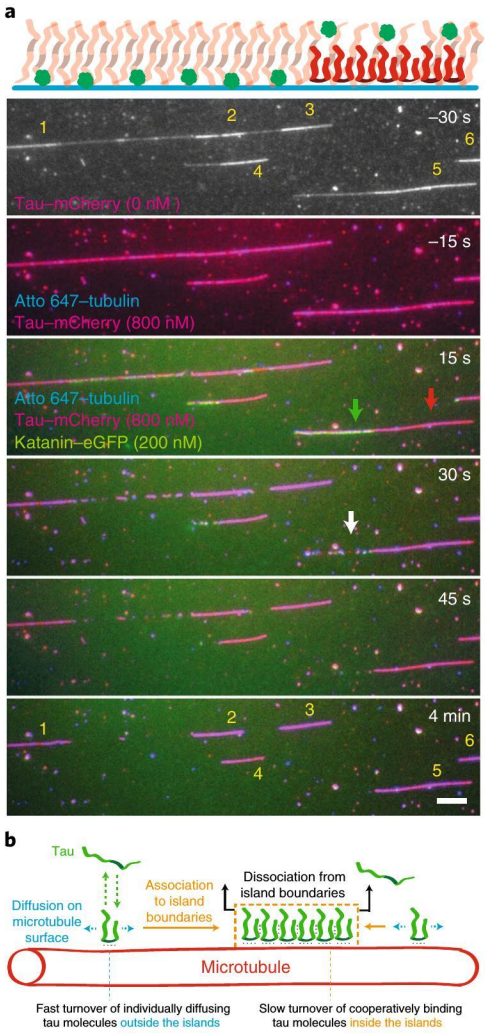

Fig. 5 | Microtubule shielding depends on tau cohesion in the islands. **a**, Multichannel fluorescence micrographs showing katanin-GFP-driven (green) severing of Atto 647-microtubules (blue) decorated with tau-mCherry islands (red) formed at 0.8 µM tau-mCherry. The island positions (indicated by numbers) were determined after a brief removal of tau-mCherry from solution (time = –30 s, Methods). After 0.8 µM tau-mCherry was re-introduced, microtubules became uniformly covered by tau-mCherry (time = –15 s). Katanin-GFP was added at time = 0 s. Katanin-GFP was recruited to regions outside the islands (example indicated by green arrow) and excluded from the islands (example indicated by red arrow). Microtubule severing and disassembly occurred initially only in the regions outside the islands (example indicated by white arrow). Over longer time scales, islands disassembled from their boundaries (compare to Fig. 4b). Scale bar, 2 µm. This experiment was repeated 11 times with similar results. **b**, Schematic representation of island formation. Tau molecules bind and unbind with high rates to microtubules, on which they diffuse (fast turnover). When encountering an island (dashed orange box), tau molecules cooperatively associate with the island at its boundaries, rendering the tau molecules stationary, decreasing their unbinding rate (slow turnover), and causing the island to grow in size laterally. Tau molecules from solution can only bind to the inside of an island via displacement of an island-associated tau molecule, resulting in the observed concentration-dependent turnover of tau inside islands. After removal of tau from solution, tau molecules dissociate from the island boundaries, making the island shrink in size laterally.

density (Fig. 4c,d, Supplementary Fig. 4f–h and Supplementary Video 5). Notably, we observed that Kip3–GFP moving in the low-density tau regions accumulated at the boundaries of the tau islands (Fig. 4c). The resulting high-density traffic jams caused enhanced unbinding of tau–mCherry at these positions, eventually leading to the displacement of the islands (Fig. 4d) at velocities comparable to Kip3–GFP walking within islands (Supplementary Fig. 4g and Supplementary Fig. 4i). These combined results show that tau islands constitute a protective layer on the microtubule surface, which blocks kinesin-1-based transport and obstructs the severing activity of katanin, and that the activity of superprocessive motors can displace existing islands from the microtubule surface.

Because the island and non-island regions exhibited similar tau densities under saturating, physiological tau concentrations (Fig. 3), we considered whether, under these conditions, the diffusible tau molecules in the non-island regions could shield the microtubules against severing. We therefore: (1) formed islands using 0.8 µM tau–mCherry, (2) after 5 min, briefly removed tau–mCherry from solution to note the position of the islands, and (3) re-introduced 0.8 µM tau–mCherry. We then immediately exposed these tau–mCherry fully decorated microtubules to 200 nM katanin–GFP analogously to the experiment presented in Fig. 4b. We observed, similarly to Fig. 4b, that the non-island regions were severed and rapidly disassembled, whereas the island-covered microtubules persisted and only slowly disassembled from their boundaries with an occasional cut in the islands (Fig. 5a, Supplementary Fig. 4d,e and Supplementary Video 6). These experiments show that the density of tau does not determine whether tau forms a protective layer around microtubules. Rather, the microtubule protection is enabled by the cohesion between the cooperatively binding tau molecules that make up the islands (Fig. 5b).

Tau islands displayed a characteristic density of about 0.26 tau molecules per tubulin dimer, suggesting that tau molecules bind to the microtubule in an ordered monolayer, presumably engaging all four microtubule-binding repeats, whose positions at a similar density were shown recently using cryo-electron microscopy[23]. At physiological tau levels (0.5 µM and above), rapidly turning-over tau co-localized with the islands. The transience of these interactions explains why this pool of tau could not be captured by cryo-electron microscopy. Our results suggest that the integrity of the islands depends on cooperativity between the constituent tau molecules. Consistent with this notion, tau molecules on microtubules interact with each other[9,24], in solution can undergo liquid–liquid phase separation[25] or, when hyperphosphorylated, form neurofibrillary tangles[6]. It seems plausible that tau–tau interactions, in addition to the binding of the four tau repeats to the microtubule, underpin the formation of islands. Alternatively, or in addition, cooperativity could depend on the number of microtubule protofilaments, as observed for doublecortin[26], and/or on a local tau-induced modification of the microtubule surface translating along the microtubule lattice into adjacent binding sites and locally increasing the affinity for incoming tau molecules.

Tau unbinding from the islands increases with increasing tau concentration in solution. This observation cannot be attributed to the pool of rapidly turning-over tau, which colocalizes with the island-incorporated tau at high concentrations (Fig. 3). At the concentrations tested (20 nM and 100 nM), this pool accounts for only approximately 20% and 40% of the total number of tau in the islands (Fig. 3c), respectively, whereas the average unbinding time decreases by two orders of magnitude. We interpret this phenomenon as the consequence of a multivalent attachment of island-incorporated tau mediated by the four microtubule-binding repeats of tau and tau–tau interaction sites. These bonds individually undergo transient cycles of unbinding and rebinding. At low tau concentration, transiently released bonds are probably re-established, as a partially bound tau molecule remains anchored to the microtubule via its persisting binding sites, keeping the released binding interfaces in close proximity. With increasing tau concentration in solution however, it becomes increasingly probable that a binding site

of a tau molecule from solution establishes a bond to a temporarily-vacated binding site on the microtubule and thereby, might replace an island-incorporated tau molecule, one bond at a time. Unbinding rates that depend on the concentration of ligands in solution, as previously reported for other multivalently interacting macromolecules[27,28], may also explain the kinesin-8-driven island disassembly. Kinesin-8 does not dissociate when an adjacent binding site on the microtubule is occupied. Instead, the motor pauses in front of a bound tau molecule until, stochastically, this next binding site becomes available by transient unbinding of a microtubule-binding repeat of tau. Kinesin-8 is then favourably positioned to occupy this site on the microtubule and thereby sequentially replace all the microtubule-binding repeats of a tau molecule. In this way, super-processive motors might regulate the localization of tau in neurons. Reciprocally, these motors might be regulated by tau islands, by the formation of traffic jams at their boundaries and reduction of their speed in the island-covered regions.

Highly curved microtubule regions show increased tau binding[29], similar to that of doublecortin[30]. Indeed we observed that tau in regions of highly curved microtubules (radius < 2.5 µm) exhibited higher density than in surrounding regions, but lower than in the islands on straight microtubule regions (Supplementary Fig. 5a (top),b, c). Of note, the highly curved regions were not protected from katanin-mediated severing (Supplementary Fig. 5a,d, Supplementary Video 7), demonstrating that tau molecules in the highly curved regions do not form a cohesive layer. Also, tau–meGFP binding in the curved regions was distinct from island formation on straight microtubules (Supplementary Fig. 5e–h). These results suggest suggest that high microtubule curvatures, though attracting tau, prevent the formation of cohesive tau islands.

In summary, we show that tau on microtubules can coexist in two kinetically distinct phases, resulting in the formation of cohesive tau islands. Complementary work by Tan et al. confirms the existence of these cohesive regions and demonstrate their significance for the regulation of cytoplasmic dynein and spastin[15]. We hypothesize that islands may act as a readout of post-translational tubulin modifications, rendering these regions differentially accessible to other MAPs. Furthermore, other intrinsically disordered proteins, analogously, might also be able to form cohesive islands on microtubules, which could add a further layer of MAP sorting and regulation on microtubules, as suggested recently[31]. It is an intriguing possibility that in neurodegenerative diseases, diminished island assembly—triggered, for example, by hyperphosphorylation of tau—could cause various downstream pathophysiological effects.

Online content

Any methods, additional references, Nature Research reporting summaries, source data, statements of code and data availability and associated accession codes are available at https://doi.org/10.1038/s41556-019-0374-6.

Received: 6 November 2018; Accepted: 18 July 2019;
Published online: 2 September 2019

References

1. Hinrichs, M. H. et al. Tau protein diffuses along the microtubule lattice. *J. Biol. Chem.* **287**, 38559–38568 (2012).
2. Kneynsberg, A., Combs, B., Christensen, K., Morfini, G. & Kanaan, N. M. Axonal degeneration in tauopathies: disease relevance and underlying mechanisms. *Front. Neurosci.* **11**, 572 (2017).
3. Qiang, L. Tau protects microtubules in the axon from severing by katanin. *J. Neurosci.* **26**, 3120–3129 (2006).
4. Morris, M., Maeda, S., Vossel, K. & Mucke, L. The many faces of tau. *Neuron* **70**, 410–426 (2011).
5. Gao, Y.-L. et al. Tau in neurodegenerative disease. *Ann. Transl. Med.* **6**, 175–175 (2018).
6. Iqbal, K., Liu, F. & Gong, C.-X. Tau and neurodegenerative disease: the story so far. *Nat. Rev. Neurol.* **12**, 15–27 (2016).
7. Drechsel, D. N., Hyman, A. A., Cobb, M. H. & Kirschner, M. W. Modulation of the dynamic instability of tubulin assembly by the microtubule-associated protein tau. *Mol. Biol. Cell* **3**, 1141–1154 (1992).
8. Chaudhary, A. R., Berger, F., Berger, C. L. & Hendricks, A. G. Tau directs intracellular trafficking by regulating the forces exerted by kinesin and dynein teams. *Traffic* **19**, 111–121 (2018).
9. Dixit, R., Ross, J. L., Goldman, Y. E. & Holzbaur, E. L. F. Differential regulation of dynein and kinesin motor proteins by Tau. *Science* **319**, 1086–1089 (2008).
10. Vershinin, M., Carter, B. C., Razafsky, D. S., King, S. J. & Gross, S. P. Multiple-motor based transport and its regulation by Tau. *Proc. Natl Acad. Sci. USA* **104**, 87–92 (2007).
11. Seitz, A. et al. Single-molecule investigation of the interference between kinesin, tau and MAP2c. *EMBO J.* **21**, 4896–4905 (2002).
12. Trinczek, B., Ebneth, A., Mandelkow, E. M. & Mandelkow, E. Tau regulates the attachment/detachment but not the speed of motors in microtubule-dependent transport of single vesicles and organelles. *J. Cell Sci.* **112**, 2355–2367 (1999).
13. Ebneth, A. et al. Overexpression of tau protein inhibits kinesin-dependent trafficking of vesicles, mitochondria, and endoplasmic reticulum: implications for Alzheimer's disease. *J. Cell Biol.* **143**, 777–794 (1998).
14. Gamblin, T. C., Berry, R. W. & Binder, L. I. Tau polymerization: role of the amino terminus. *Biochemistry* **42**, 2252–2257 (2003).
15. Tan, R. et al. Microtubules gate tau condensation to spatially regulate microtubule functions. *Nat. Cell Biol.* https://doi.org/10.1038/s41556-019-0375-5 (2019).
16. Makrides, V., Massie, M. R., Feinstein, S. C. & Lew, J. Evidence for two distinct binding sites for tau on microtubules. *Proc. Natl Acad. Sci. USA* **101**, 6746–6751 (2004).
17. Wegmann, S. et al. Tau protein liquid–liquid phase separation can initiate tau aggregation. *EMBO J.* **37**, e98049 (2018).
18. Schneider, R., Korten, T., Walter, W. J. & Diez, S. Kinesin-1 motors can circumvent permanent roadblocks by side-shifting to neighboring protofilaments. *Biophys. J.* **108**, 2249–2257 (2015).
19. Telley, I. A., Bieling, P. & Surrey, T. Obstacles on the microtubule reduce the processivity of Kinesin-1 in a minimal in vitro system and in cell extract. *Biophys. J.* **96**, 3341–3353 (2009).
20. Jiang, K. et al. Microtubule minus-end regulation at spindle poles by an ASPM–katanin complex. *Nat. Cell Biol.* **19**, 480–492 (2017).
21. Varga, V., Leduc, C., Bormuth, V., Diez, S. & Howard, J. Kinesin-8 motors act cooperatively to mediate length-dependent microtubule depolymerization. *Cell* **138**, 1174–1183 (2009).
22. Leduc, C. et al. Molecular crowding creates traffic jams of kinesin motors on microtubules. *Proc. Natl Acad. Sci. USA* **109**, 6100–6105 (2012).
23. Kellogg, E. H. et al. Near-atomic model of microtubule–tau interactions. *Science* **360**, 1242–1246 (2018).
24. McVicker, D. P., Hoeprich, G. J., Thompson, A. R. & Berger, C. L. Tau interconverts between diffusive and stable populations on the microtubule surface in an isoform and lattice specific manner. *Cytoskeleton* **71**, 184–194 (2014).
25. Hernández-Vega, A. et al. Local nucleation of microtubule bundles through tubulin concentration into a condensed Tau phase. *Cell Rep.* **20**, 2304–2312 (2017).
26. Bechstedt, S. & Brouhard, G. J. Doublecortin recognizes the 13-protofilament microtubule cooperatively and tracks microtubule ends. *Dev. Cell* **23**, 181–192 (2012).
27. Sing, C. E., Olvera de la Cruz, M. & Marko, J. F. Multiple-binding-site mechanism explains concentration-dependent unbinding rates of DNA-binding proteins. *Nucleic Acids Res.* **42**, 3783–3791 (2014).
28. Lansky, Z. et al. Diffusible crosslinkers generate directed forces in microtubule networks. *Cell* **160**, 1159–1168 (2015).
29. Samsonov, A., Yu, J.-Z., Rasenick, M. & Popov, S. V. Tau interaction with microtubules in vivo. *J. Cell Sci.* **117**, 6129–6141 (2004).
30. Bechstedt, S., Lu, K. & Brouhard, G. J. Doublecortin recognizes the longitudinal curvature of the microtubule end and lattice. *Curr. Biol.* **24**, 2366–2375 (2014).
31. Monroy, B. Y. et al. Competition between microtubule-associated proteins directs motor transport. *Nat. Commun.* **9**, 1714 (2018).

Acknowledgements

We thank A. Akhmanova and K. Jiang for the generous gift of the katanin plasmid, R. McKenney for feedback and sharing of data, V. Henrichs, I. Zhernov and L. Grycova for help with protein preparation, and Y. Bobrova, S. Dijkstra and C. Bräuer for technical support. We acknowledge the financial support from the Czech Science Foundation (grant no. 18-08304S to Z.L. and 17-12496Y to M.B.), the Introduction of

New Research Methods to BIOCEV (CZ.1.05/2.1.00/19.0390) project from the ERDF, the institutional support from the CAS (RVO: 86652036) and the Imaging Methods Core Facility at BIOCEV, an institution supported by the Czech-BioImaging large RI projects (LM2015062 and CZ.02.1.01/0.0/0.0/16_013/0001775, funded by MEYS CR) for their support in obtaining imaging data presented in this paper.

Author contributions

A.H.-V. and M.B. first observed the islands and initiated the project; A.H.-V., A.A.H., S.D., Z.L. and M.B. conceived the experiments; A.H.-V. generated the tau(ΔN)–meGFP construct; V.S., J.K., A.H.-V. and M.B. generated the proteins, performed and analysed the experiments and V.S., J.K., S.D., Z.L. and M.B. wrote the manuscript. All authors discussed the results and commented on the manuscript.

Competing interests

The authors declare no competing interests.

Additional information

Supplementary information is available for this paper at https://doi.org/10.1038/s41556-019-0374-6.

Reprints and permissions information is available at www.nature.com/reprints.

Correspondence and requests for materials should be addressed to A.H.-V., Z.L. or M.B.

Publisher's note: Springer Nature remains neutral with regard to jurisdictional claims in published maps and institutional affiliations.

Methods

Protein purification. meGFP- or mCherry-tagged tau and tau(ΔN), kinesin-1, Kip3 and katanin were expressed and purified as described previously[20,25,32,33].

In vitro tau–microtubule binding assay. Microtubules and flow chambers were prepared as described previously[33,34]. Biotinylated, paclitaxel-stabilized, Atto 647-labelled microtubules in BRB80T (80 mM PIPES–KOH pH 6.9, 1 mM $MgCl_2$, 1 mM EGTA and 10 μM paclitaxel) were immobilized in a flow chamber using biotin antiboy (Sigma B3640, 20 μg ml^{-1} in PBS). Subsequently, the buffer in the flow chamber was exchanged for assay buffer (20 mM HEPES pH 7.4, 1 mM EGTA, 75 mM KCl, 2 mM $MgCl_2$, 1 mM Mg–ATP, 10 mM dithiothreitol, 0.02 mg ml^{-1} casein, 10 μM paclitaxel, 20 mM D-glucose, 0.22 mg ml^{-1} glucose oxidase and 20 μg ml^{-1} catalase). Tau in assay buffer was then flushed into the flow chamber at the final assay concentration as indicated in the text. To test the robustness of island assembly, we observed island assembly under different conditions of ionic strength (0–125 mM KCl additional to the assay buffer), pH (6.8–7.4) and buffering agent (20 mM HEPES, 50 mM HEPES and 80 mM PIPES). In experiments including multiple subsequent tau additions, the flow chamber was rinsed between each tau addition with high ionic strength buffer (125 mM KCl additional to the assay buffer). To remove tau from solution, the chamber was perfused with approximately four times the chamber volume using assay buffer without tau. For high concentrations of tau (>200 nM), higher volumes (up to ten times the chamber volume) were used to remove tau. In experiments involving kinesin-8, katanin or kinesin-1, islands were first pre-formed before the respective protein was added to the solution (keeping the tau concentration constant). For the katanin experiment at elevated tau concentration (Fig. 5), microtubules were first incubated with 0.8 μM tau–mCherry for 5 min. Tau–mCherry was then briefly removed from the measurement chamber (less than 1 min) for the positions of the islands to be recorded (they were obscured by the high tau–mCherry density in the island surroundings). Tau–mCherry was then added at 0.8 μM. Subsequently, 200 nM katanin–GFP was added to the solution (while maintaining the tau concentration at 0.8 μM). All experiments were performed at room temperature.

Imaging. Atto 647-labelled microtubules and mCherry- and meGFP-labelled proteins were visualized sequentially by switching between the Cy5, TRITC and GFP channels (Chroma filter cubes) on a Nikon-Ti E microscope equipped with a ×100 Nikon TIRFM objective and either Hamamatsu Orca Flash 4.0 sCMOS or Andor iXon EMCCD cameras. The acquisition rate varied between 1 frame per 30 ms to 1 frame per 10 min, depending on the experiment and is indicated in the corresponding figure. Imaging conditions in experiments used for quantitative estimation of kinetic parameters were set such that photobleaching effects were negligible (<2% fluorescent intensity loss during the experiment). Experiments were performed over several months by three researchers. Each experiment was repeated at least on three days. No data was excluded from the study.

Image analysis. Data was analysed using FIJI v.1.52[35] and custom Matlab (Mathworks) routines.

Tau density estimation. Kymographs (using FIJI KymographBuilder plugin, modified to compute integrated intensity instead of finding the maximum intensity) along the microtubule length were used to read out the meGFP or mCherry fluorescent signal and to estimate the integrated signal intensity of meGFP- or mCherry-labelled tau bound to the microtubule (if necessary, time series were drift-corrected with the FIJI plugin 'image stabilizer'). The meGFP signal in regions directly adjacent to the microtubule was estimated in the same way, smoothed with a moving median along the microtubule length and subtracted as background signal. The kymograph pixels were then manually categorized according to the type of microtubule region they covered (islands, regions surrounding the islands, or regions of highly curved microtubules with an increased tau density). The integrated intensity of tau for a region on a microtubule was then computed for each frame by taking the sum of the categorized kymograph pixels. The density of meGFP- or mCherry-labelled tau bound to the microtubule was then estimated by dividing the integrated intensity by the estimated intensity per single fluorescent molecule (either mCherry or meGFP, see below) and the length of the region. Conversion to the number of tau molecules per tubulin dimer was performed assuming tau binding to 13 protofilaments and an 8 nm length of tubulin dimer. The Kip3 densities were estimated analogously: tau–mCherry islands were identified in the corresponding channel (561 nm), and density traces of Kip3–GFP (488 nm) were read out at the corresponding locations.

Single fluorophore quantification. Fluorescent signal of a single fluorescent molecule (meGFP or mCherry) was determined by generating intensity time traces of single meGFP- or mCherry-labelled kinesin-1 molecules tightly bound to the microtubule in presence of adenylyl-imidodiphosphate (in the absence of ATP) and estimating the 'height' of the bleaching steps. The number of steps was first estimated by eye, and this number was used as input for the findchangepoints function of Matlab to determine the position of the steps (by detection of significant changes of the mean value). To yield the intensity per single molecule, the median of the heights of these steps was calculated. The number of averaged steps was at least 15 per estimate. Photobleaching rates (at the given imaging conditions, on the day of the experiment) were determined using the experimental setup described above. Instead of single-molecule intensities, the integrated intensity of all labelled kinesin-1 molecules was measured.

The fraction of microtubule length covered by tau islands. The fraction of microtubule length covered by tau islands was estimated by approximating islands and microtubules with segmented lines, measuring their lengths and dividing the sum of the lengths of the islands on a single microtubule (or in a field of view) by the length of the respective microtubule on which the islands are located (or by the summed length of all microtubules in a field of view).

Estimation of the tau-unbinding time. To estimate the unbinding times of tau inside and outside the islands, we analysed how the tau density in a given region decayed over time after a buffer exchange that either removed tau from solution or replaced tau–meGFP in the solution with tau–mCherry. Every analysed region (island or surrounding) yielded a time trace of tau density decay after a buffer exchange. Time traces from exemplary experiments were combined to be presented in Fig. 1f,h, Supplementary Figs. 1g, 2b,c; the line represents the median value of all traces at the given point in time and the edges of the shaded area represent the first and third quartiles. To estimate the mean residence times of tau inside and outside the islands, individual density time traces as described above were fitted separately by an exponential decay using the Matlab function 'fit' (data points taken before exchange of solution were not taken into account). The presented fits and mean residence times were computed by averaging the coefficients of the individual fits.

Estimation of velocity and diffusion coefficient. Tracking of single tau molecules for the estimation of diffusion coefficient was performed using FIESTA[36] software. To reconnect tracks, a threshold velocity of 12,000 nm s^{-1} was chosen, and tracks were allowed to have at most three missing frames between two data points. To minimize false-positive connections of molecules, the tracks obtained by FIESTA were cut such that the maximum distance between two data points was never more than 360 nm. Island boundary assembly and disassembly velocities (in the absence or presence of katanin or Kip3) were estimated by approximating straight lines onto segments of advancing or receding tau-island edges in kymographs. The value presented in the text is a duration-weighted average of the corresponding segments. This was converted to the number of tau molecules per second by multiplying this velocity by the estimated characteristic tau density within islands (in molecules per nanometre), assuming tau binding to 13 protofilaments and 8 nm length per tubulin dimer. Kip3 and kinesin-1 velocities were estimated by approximating straight lines onto kymographs of moving motors (inside and outside islands).

Katanin severing-rate estimation. Severing rates in the areas surrounding the islands were estimated by fitting exponential decay to the number of pixels in the area of the original microtubule position above a threshold value, which was manually set to encompass the microtubule. In island regions, cuts were counted. In Supplementary Fig. 4e, the estimated severing rates include both straight and curved microtubules. In Supplementary Fig. 5d, the severing rates are sorted according to the following definition: straight microtubules were defined as microtubule stretches in which the microtubule orientation would not change beyond 10°; curved regions were defined as 0.5 μm-long stretches of microtubule centred at the point of highest curvature with radius <2.5 μm.

Data representation. In all box plots presented in the figures, the horizontal midline indicates the median; bottom and top box edges indicate the 25th and 75th percentiles, respectively; the whiskers extend to the most extreme data points not considered as outliers (the function 'Alternative box plot' from the IoSR Matlab Toolbox has been used). Thick lines with shaded areas, unless otherwise indicated, show the median and the 25th and 75th percentiles. Where single data points are presented, points from the same experiment are indicated by the same colour (unless otherwise stated). The individual data points have been weighted such that each experiment carries the same weight for determination of the median and percentile lines. Weighting by experiments has been performed in all data represented in the text or in figures involving averages or quartiles, except for the determination of the diffusion constants of tau, where each experiment was weighted according to how many tau molecules were observed in the respective experiment.

Statistics and reproducibility. Experiments were performed over several months by three researchers; all replication attempts (that were not impeded by unrelated events, such as an image-acquisition-software malfunction) were successful. For each quantified experiment and each exemplary image or kymograph, *N* describes the number of either biologically independent samples (individual tau molecules, islands of tau molecules or microtubules) or the number of independent events (island nucleation, island merging or island fission). In all cases, the number of independent experiments, during which the data were gathered over the course

of several days, refers to the number of independent flow channels, which were assembled, filled with assay components and imaged individually.

Reporting Summary. Further information on research design is available in the Nature Research Reporting Summary linked to this article.

Data availability

Source data for Figs. 1–5 and quantifications given in the main text (island density) have been provided as Supplementary Table 1. Example raw videos are available at BioStudies with accession number S-BSST266. All other data supporting the findings of this study are available from the corresponding authors on reasonable request.

Code availability

Code used to determine single-molecule intensities (GNU General Public License v.3, for further information see repository) is available at https://doi.org/10.5281/zenodo.3270568. Code used to create kymographs (MIT license, for further information see repository) is available at https://doi.org/10.5281/zenodo.3270572. All other custom written code is available from the corresponding authors on request.

References

32. Mitra, A., Ruhnow, F., Girardo, S. & Diez, S. Directionally biased sidestepping of Kip3/kinesin-8 is regulated by ATP waiting time and motor-microtubule interaction strength. *Proc. Natl Acad. Sci. USA* **115**, E7950–E7959 (2018).
33. Nitzsche, B. et al. Studying kinesin motors by optical 3D-nanometry in gliding motility assays. *Methods Cell Biol.* **95**, 247–271 (2010).
34. Braun, M. et al. Adaptive braking by Ase1 prevents overlapping microtubules from sliding completely apart. *Nat. Cell Biol.* **13**, 1259–1264 (2011).
35. Schindelin, J. et al. Fiji: an open-source platform for biological-image analysis. *Nat. Methods* **9**, 676–682 (2012).
36. Ruhnow, F., Zwicker, D. & Diez, S. Tracking single particles and elongated filaments with nanometer precision. *Biophys. J.* **100**, 2820–2828 (2011).

A.2 MICROTUBULE LATTICE SPACING GOVERNS COHESIVE ENVELOPE FORMATION OF TAU FAMILY PROTEINS

Siahaan, V.*, Tan, R.*, Humhalova, T. Libusova, L., Lacey, S. E., Tan, T., Dacy, M., Ori-McKenney, K. M., McKenney, R. J., Braun, M., Lansky, Z. Microtubule lattice spacing governs cohesive envelope formation of tau family proteins. *Nat Chem Biol* 18, 1224–1235 (2022).

*These authors contributed equally.

Contributions as stated in the article:

The manuscript was conceptualized by R.T., K.M.O.M., R.J.M., M.B., and Z.L.; methods were developed by V.S., T.H., L.L., S.E.L., R.J.M., M.B., and Z.L.; recombinant proteins were generated by V.S., R.T., T.T., and M.D.; TIRF experiments were performed by V.S., R.T., and R.J.M.; optical tweezers experiments by V.S.; cryo-EM experiments by S.E.L.; live-cell experiments by T.H.; data were formally analyzed by V.S., R.T., T.H., S.E.L., K.M.O.M., and R.J.M.; the manuscript was written by V.S., L.L., K.M.O.M., R.J.M., M.B., Z.L., with reviewing and editing by T.T. and M.D.; the project was supervised by K.M.O.M., R.J.M., M.B., and Z.L.; funding was acquired by V.S., T.H., L.L., K.M.O.M., R.J.M., M.B., and Z.L.

In detail: V.S. optimized the methods and performed all experiments visualized in figure 1 and 2. These experiments include work using both TIRF microscopy and optical trapping. Additionally, V.S. optimized the methods and performed the experiments represented in figure 3e. All analysis for figures 1 (all), 2 (all), and 3e were carried out by V.S. using ImageJ, Excel, FIESTA tracking software, and Matlab. Analysis for the in vivo data presented in figure 4 was carried out by T.H. with help from V.S. Visualization for figures 1 (all), 2 (all), 3e, and 4 (all) was carried out by V.S. using Matlab and Illustrator. Tau-GFP and tau-mCherry constructs were generated by V.S. The manuscript was written by V.S., L.L., K.M.O.M., R.J.M., M.B., Z.L. Additionally, funding was acquired by V.S. from the Charles University Grant Schemes: GAUK no. 373821, and START reg. no. CZ.02.2.69/0.0/0.0/19_073/0016935.

ARTICLES
https://doi.org/10.1038/s41589-022-01096-2

nature chemical biology

Microtubule lattice spacing governs cohesive envelope formation of tau family proteins

Valerie Siahaan[1,7], Ruensern Tan[2,5,7], Tereza Humhalova[3], Lenka Libusova[3], Samuel E. Lacey[4,6], Tracy Tan[2], Mariah Dacy[2], Kassandra M. Ori-McKenney[2]✉, Richard J. McKenney[2]✉, Marcus Braun[1]✉ and Zdenek Lansky[1]✉

Tau is an intrinsically disordered microtubule-associated protein (MAP) implicated in neurodegenerative disease. On microtubules, tau molecules segregate into two kinetically distinct phases, consisting of either independently diffusing molecules or interacting molecules that form cohesive 'envelopes' around microtubules. Envelopes differentially regulate lattice accessibility for other MAPs, but the mechanism of envelope formation remains unclear. Here we find that tau envelopes form cooperatively, locally altering the spacing of tubulin dimers within the microtubule lattice. Envelope formation compacted the underlying lattice, whereas lattice extension induced tau envelope disassembly. Investigating other members of the tau family, we find that MAP2 similarly forms envelopes governed by lattice spacing, whereas MAP4 cannot. Envelopes differentially biased motor protein movement, suggesting that tau family members could spatially divide the microtubule surface into functionally distinct regions. We conclude that the interdependent allostery between lattice spacing and cooperative envelope formation provides the molecular basis for spatial regulation of microtubule-based processes by tau and MAP2.

Microtubules, polymers composed of tubulin, provide mechanical rigidity for the cell and tracks for motor-driven intracellular transport. Microtubules undergo alternating phases of polymerization and depolymerization, dependent on tubulin GTP hydrolysis activity. During polymerization, GTP-tubulin associates with the growing tip of the microtubule. After tubulin incorporation into the microtubule lattice, tubulin-bound GTP is hydrolyzed to GDP. GTP hydrolysis is accompanied by a ~2.5 Å longitudinal compaction of the interdimer interface within the mammalian tubulin lattice[1]. Compacted GDP-lattices can be artificially extended by microtubule stabilizing agents, such as the GTP analog guanosine-5′-[(α,β)-methyleno]triphosphate (GMPCPP) or taxol (Paclitaxel)[1]. While GMPCPP keeps the microtubule lattice in an extended state owing to its extremely low turnover[2], taxol binds transiently and increases the microtubule lattice spacing reversibly[3]. Tubulin spacing can also be altered by the interaction of microtubule-associated proteins (MAPs) with the lattice[4–6], demonstrating the dynamic interdependence between the structure of the microtubule lattice and lattice-bound proteins.

MAPs have different affinities for the compacted or extended tubulin lattice and can employ this difference as a readout for their localization on the microtubule. High affinity for the GTP-tubulin enables localization of specific MAPs to the microtubule tips[7,8]. Other MAPs, such as the kinesin-3 KIF1A or the neuronal protein tau, are reported to have a higher affinity for GDP tubulin, which enables their specific localization to the GDP regions of the microtubules[9–11].

Tau, along with MAP2 and MAP4, constitute a family of evolutionarily and structurally related, intrinsically disordered MAPs, important in neuronal development and function[12,13]. Neuronally enriched tau is associated with a number of neurodegenerative disorders termed 'tauopathies', while, to date, a role for MAP2 and MAP4 in disease has not been described[14,15]. MAP2 is mostly localized to dendrites and regulates neuronal cargo trafficking by inhibiting kinesin motors[16,17]. In contrast to tau and MAP2, MAP4 is more ubiquitously expressed in various tissues[12]. MAP4 regulates microtubule-based cargo trafficking by inhibiting dynein motility and enhancing kinesin-based transport. However, a MAP4 fragment reduced the motility of kinesin-1 and kinesin-3 in vitro[18–20], and overexpression of MAP4 inhibited vesicle motility in vivo[21].

Tau can assemble into various higher-order structures. In solution, tau undergoes liquid–liquid phase separation[22–24], In neurons, tau aggregates into neurofibrillary tangles[25], found in Alzheimer's disease brains. When bound to microtubules, tau molecules can form oligomers[26,27] and cohesive envelopes, previously referred to as 'condensates' or 'islands'[9,28], which act as selectively permeable barriers for other MAPs[9,28], inhibiting kinesin motility, while allowing dynein-based motility[9,16,17,26,28,29]. The mechanism underlying the envelope formation, however, remains elusive.

Here we found that microtubule lattice spacing governs the cooperative formation of tau envelopes. We show that this mechanism is conserved for MAP2, but not MAP4, and demonstrate functional consequences of these differential binding modes. Our results show that the regulation of MAP cooperativity through the spacing of tubulin dimers within the microtubule lattice is a divergent evolutionary feature within this family of MAPs.

Results

Tau cooperativity by local microtubule lattice compaction. To study the tau envelope formation, we immobilized taxol-stabilized

[1]Institute of Biotechnology, Czech Academy of Sciences, BIOCEV, Prague West, Czech Republic. [2]Department of Molecular and Cellular Biology, University of California – Davis, Davis, CA, USA. [3]Department of Cell Biology, Faculty of Science, Charles University, Prague, Czech Republic. [4]Structural Studies Division, MRC Laboratory of Molecular Biology, Cambridge, UK. [5]Present address: Department of Molecular and Cellular Biology, University of California at Berkeley, Berkeley, CA, USA. [6]Present address: Human Technopole, Milan, Italy. [7]These authors contributed equally: Valerie Siahaan, Ruensern Tan. ✉e-mail: kmorimckenney@ucdavis.edu; rjmckenney@ucdavis.edu; marcus.braun@ibt.cas.cz; zdenek.lansky@ibt.cas.cz

microtubules on a coverslip, added purified fluorescently labeled full-length 2N4R tau, and imaged the system using total internal reflection fluorescence (TIRF) microscopy (Fig. 1a). Initially we varied tau concentration and measured the tau density on the microtubule surface, revealing that tau envelope formation is a cooperative process (Fig. 1b) with a Hill coefficient of 1.9 ± 0.7. During envelope growth we often observed straightening of microtubules (Fig. 1c and Supplementary Movie 1), suggesting that cooperative binding of tau influences the microtubule structure. Previously, we observed that tau envelopes form on GDP-microtubule lattices but do not form on microtubules stabilized with GMPCPP[9]. To probe how the structure of the microtubule lattice affects tau envelope formation, we analyzed the envelope growth on (a) GMPCPP-capped GDP-lattice microtubules (natively compacted), (b) taxol-lattice microtubules (extended reversibly), and (c) GMPCPP-lattice microtubules (extended irreversibly). We observed that the rate with which tau envelopes covered the GDP-lattice microtubules ($1.6 \pm 1.3\,\mu m\,s^{-1}$; mean ± s.d.) was more than an order of magnitude faster than the coverage rate on taxol-lattice microtubules ($23.0 \pm 12.8\,nm\,s^{-1}$; mean ± s.d.), while, in agreement with previous observations[9], no envelope formation was observed on GMPCPP-lattice microtubules (Fig. 1d and Supplementary Fig. 1a–d). These results demonstrate that cooperative tau envelopes preferably form on compacted GDP-lattice microtubules.

To test if irreversible lattice extension hinders the envelope formation, even at saturating tau concentrations, we added 600 nM tau to a mixture of GMPCPP-lattice and taxol-lattice microtubules (Fig. 1e). At this concentration, tau uniformly covers the microtubule and the envelopes cannot be distinguished by local changes in tau density. However, tau envelopes can be detected by their effect on kinesin-1, which is occluded from the envelopes[28]. After the addition of 60 nM kinesin-1, we observed no movement of kinesin-1 on the taxol-lattice microtubules, showing that these were fully covered by tau envelopes (Fig. 1e, Supplementary Movie 2 and Supplementary Fig. 1e,f). By contrast, on the GMPCPP-lattice microtubules, kinesin-1 moved along their entire lengths, revealing that tau did not form envelopes, even at saturating tau concentrations. Additionally, we studied dynamics of single tau molecules on GMPCPP-lattice microtubules within this elevated tau concentration (600 nM tau-mCherry and 0.2 nM tau-meGFP) and found that 100% of single tau-meGFP molecules moved diffusively on GMPCPP-lattice microtubules (Supplementary Fig. 1g). This further reveals that tau does not form envelopes on GMPCPP-lattice microtubules, since tau molecules inside envelopes do not diffuse, but remain stationary[9,28]. Permanent extension of the microtubule lattice thus prevents envelope formation, suggesting that the microtubule lattice spacing might regulate the envelope formation.

Therefore, we reasoned that tau envelope formation might induce microtubule lattice compaction. To test this hypothesis, we employed sparsely labeled microtubules (Fig. 1f) with fluorescent speckles marking fixed positions on the microtubule. After the addition of 400 nM tau to speckled taxol-lattice microtubules, envelopes formed rapidly and we observed a decrease in the distances between the individual speckles, indicating that the microtubule lattice was compacting concomitantly with the cooperative binding of tau (Fig. 1g and Supplementary Movie 3). Repeating the experiment at lower tau concentration (20 nM), and following the compaction inside and outside the envelope regions, we found no compaction of the lattice in the regions of the microtubule not covered by tau envelopes, while the lattice regions covered by a tau envelope showed a compaction of $3.2 \pm 1.0\%$ (Fig. 1h and Supplementary Fig. 1h–k). The extent of the compaction is similar to the length difference between GTP- and GDP-bound tubulin dimers estimated previously by cryo-electron microscopy (cryo-EM) to be 2.4%[1], suggesting that tau envelopes shift tubulin from its extended GTP-like into its compacted GDP- conformation. As cooperative binding of tau to the microtubule reverses the taxol-induced lattice extension, we asked if the envelope formation will locally induce dissociation of taxanes from the microtubule. We visualized tau interaction with microtubules labeled with SiR-tubulin, a fluorogenic taxane that is based on docetaxel, which binds to the same site as taxol, but with a higher affinity[30]. Comparison of the SiR-tubulin intensity within or outside the tau envelope regions (Fig. 1i,j and Supplementary Movie 4) revealed a decrease of $21.7 \pm 12.9\%$ (mean ± s.d.) within the enveloped regions. These results are consistent with prior data showing competition between tau and taxol for microtubules[31]. Combined, these experiments show that a localized structural shift to the compacted GDP-tubulin microtubule lattice induces cooperative formation of tau envelopes.

Lattice extension induces disassembly of tau envelopes. Tau-envelope formation induces a reversible compaction of taxol-extended tubulin. We hypothesized that physically lengthening microtubule lattices either locally or globally should induce the disassembly of tau envelopes. Locally, we extended the lattice by bending the microtubules in a hydrodynamic flow. Using GMPCPP-capped GDP-lattice microtubules attached to the coverslip at a single point, we formed tau envelopes over the entire length of the GDP-lattice. By briefly (~10 s) introducing a hydrodynamic flow, the microtubules bent at their single attachment points, extending

Fig. 1 | Tau cooperativity through local microtubule lattice compaction. a, Schematics of the assay geometry. **b**, Quantification of cooperative binding of tau to taxol-lattice microtubules (mean ± s.d., $n = 652$ microtubules, 60 experiments, 95% confidence bounds, $r^2 = 0.9633$, gray), Hill–Langmuir equation fit (green). AU, arbitrary units. **c**, Fluorescence time-lapse micrographs showing microtubule lattice straightening (yellow arrow) upon formation of tau envelopes (green). Twenty nanomolar tau-mCherry was added at $t = 0$ s. Scale bar, 2 µm. **d**, Rate of increase of tau envelope microtubule coverage (Methods) on different lattices after the addition of 20 nM tau-mCherry. Coverage rate was $1.6 \pm 1.3\,\mu m\,s^{-1}$ (mean ± s.d., $n = 34$ microtubules, 5 experiments) on GDP-lattice microtubules (orange), $23.0 \pm 12.8\,nm\,s^{-1}$ (mean ± s.d., $n = 49$ microtubules, 3 experiments) on taxol-lattice microtubules (blue) and no envelope formation ($n = 200$ microtubules, 14 experiments) on GMPCPP-lattice microtubules (red). MT, microtubules. **e**, Fluorescence micrograph (top left) showing a taxol-lattice microtubule (marked by a blue dotted rectangle) and a GMPCPP-lattice microtubule (marked by a red dotted rectangle) after the addition of 600 nM tau-mCherry (green) and 60 nM kinesin-1-GFP. Fluorescence intensity profile along the microtubule length (bottom left) shows that the tau-mCherry density is comparable on both microtubules. Fluorescence kymographs (right) show that kinesin-1-GFP does not processively move on taxol-lattice microtubules (left) and moves on GMPCPP-lattice microtubules (right). Scale, vertical 1 s, horizontal 2 µm. Int., intensity. **f**, Fluorescence micrograph of a speckled Atto647-labeled microtubule (top) after the addition of 400 nM tau-meGFP (bottom). Scale bar, 2 µm. **g**, Multi-channel kymograph corresponding to the microtubule in **f** showing compaction of the microtubule lattice—individual speckles (white) move closer to each other after the addition of 400 nM tau-meGFP (green). Addition of tau-meGFP is marked by green arrows. Scale bars, 2 µm, 1 min. **h**, Compaction of the microtubule lattice by tau within the envelope regions ($3.2 \pm 1.1\%$, mean ± s.d., $n = 59$ envelope regions, 7 experiments) and outside the envelope regions ($-0.1 \pm 1.1\%$, mean ± s.d., $n = 57$ microtubules, 7 experiments). **i**, Fluorescence micrographs of 2 µM SiR-tubulin (magenta) on a microtubule lattice before and after the addition of 20 nM tau-mCherry (green) at $t = 0$ s. Green arrows indicate tau envelopes. Pink arrows indicate the corresponding local decrease in the SiR-tubulin density. Local decrease in tau density within tau envelope regions was $21.7 \pm 12.9\%$ (mean ± s.d., $n = 72$ envelopes, 5 experiments). Scale bar, 2 µm. **j**, Fluorescence intensity profile of SiR-tubulin (magenta) and tau-mCherry (green) on the microtubule lattice shown in **i**.

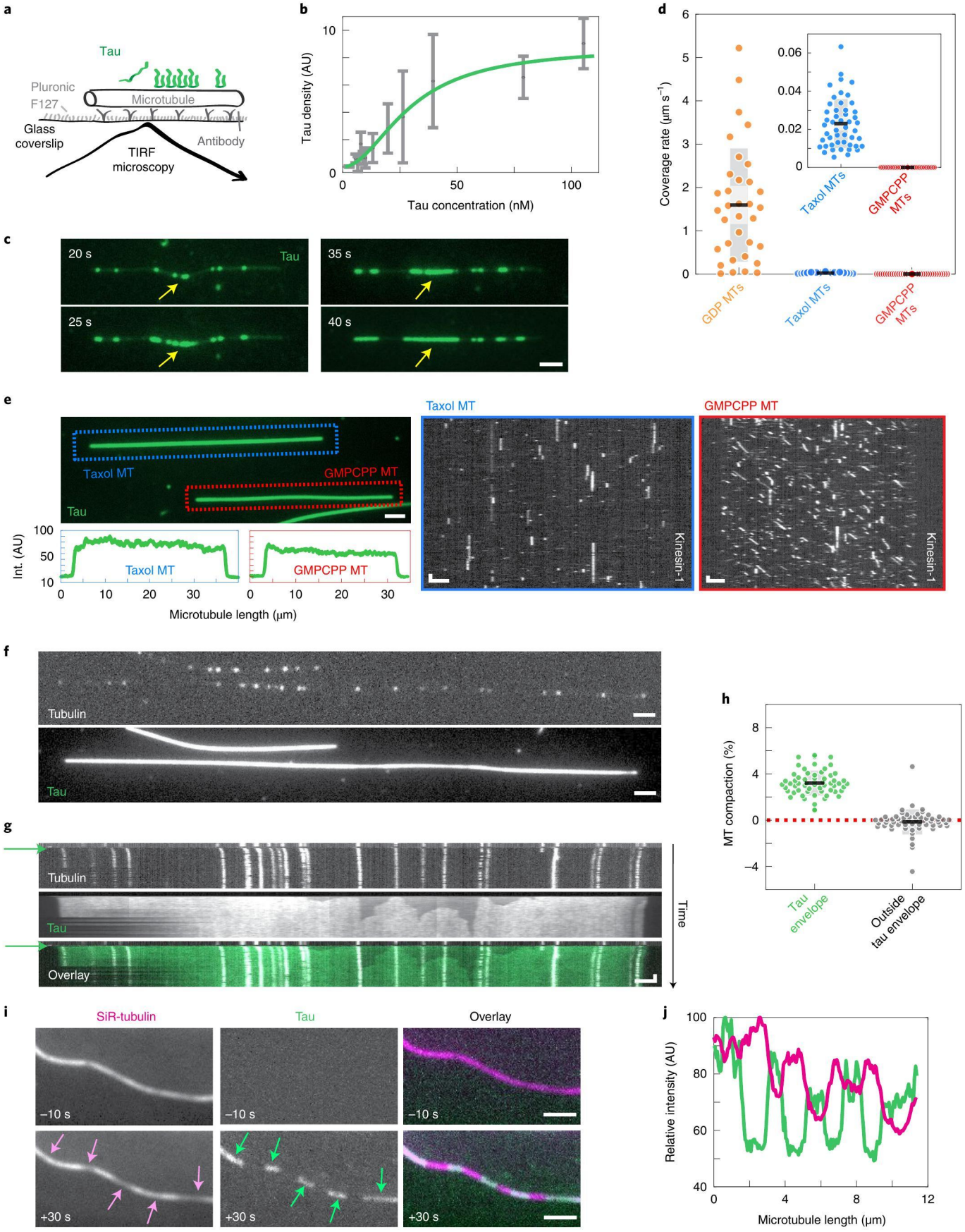
a
Tau
Pluronic F127
Microtubule
Glass coverslip
Antibody
TIRF microscopy
b
Tau density (AU)
Tau concentration (nM)
d
Coverage rate (μm s−1)
GDP MTs
Taxol MTs
GMPCPP MTs
c
20 s
Tau
25 s
35 s
40 s
e
Taxol MT
GMPCPP MT
Tau
Int. (AU)
Microtubule length (μm)
Kinesin-1
f
Tubulin
Tau
g
Tubulin
Tau
Overlay
Time
h
MT compaction (%)
Tau envelope
Outside tau envelope
i
SiR-tubulin
Tau
Overlay
−10 s
+30 s
j
Relative intensity (AU)
Microtubule length (μm)

the lattice locally on the outside of the bend point (Fig. 2a). During the hydrodynamic flow, we removed tau from solution and added either buffer alone or buffer containing 10 µM taxol to further induce lattice extension. After the period of flow, the microtubules relaxed back to their original (straight) shape. We found that, during the flow period, both in presence and absence of taxol, the tau density in the highly curved regions dropped by approximately 50% (Fig. 2b), indicating a fissure in the envelope. After the hydrodynamic flow, in the presence of 10 µM taxol in solution, the envelopes disassembled from the ends. Additionally, the envelope started disassembling from the location where the fissure had been introduced by mechanical bending (Fig. 2a and Supplementary Movie 5) as evidenced by a drop in tau density to 3.6 ± 2.8% (Fig. 2a,b; mean ± s.d.). In the absence of taxol, the fissure closed when the microtubule relaxed, with the tau density recovering to 77.3 ± 10.8% (Fig. 2a,b and Supplementary Movie 6; mean ± s.d.). These results demonstrate that transient local extension of the lattice by mechanical means destabilizes tau envelopes.

To assess if physical extension of the entire microtubule lattice can induce tau envelope disassembly, we attached individual microtubules between two beads held in two optical traps and moved the beads apart until we began detecting a force increase. We then fixed the beads in this position, with the microtubule in a straight but non-stretched state (Fig. 2c). After adding 60 nM tau to the chamber we observed tau envelope formation (Fig. 2d) and, simultaneously, detected an increase in force caused by a decrease in the distance between the two beads, indicating a compaction of the microtubule lattice (Fig. 2e,f). No compaction was detected in a control experiment when the buffer was exchanged but no tau was added (Fig. 2e and Supplementary Fig. 2a). Next, we stretched microtubules with pre-formed tau envelopes by moving the beads apart until we reached a set force of 40 pN. We then removed tau from solution and monitored the disassembly rate of the tau envelopes while keeping the force constant (Fig. 2g,h and Supplementary Movie 7). In a control experiment, we monitored the disassembly rate of tau envelopes on microtubules suspended in a relaxed, non-stretched state (Fig. 2h,i, Supplementary Movie 8). We found that the disassembly rate of tau envelopes increased twofold when the microtubule lattice was stretched by an external force. Combined, these experiments establish that tau envelope formation is tightly linked to microtubule mechanics, and show that physically extending microtubule lattices coated by tau envelopes induces envelope disassembly, suggesting that tau functions in living cells may be mechanosensitive.

Conservation of MAP envelope formation within the tau family. In vertebrates, the tau family also includes the neuronal MAP2 and the more ubiquitously expressed MAP4, which are conserved within their carboxy-terminal microtubule-binding repeats, and differ substantially outside this region[12,13] (Fig. 3a). To investigate whether envelope formation is conserved within the tau family, we produced MAP2c and MAP4 (Fig. 3a), and examined the behavior of these MAPs on taxol-lattice and GMPCPP-lattice microtubules (Fig. 3b). MAP2c behaved similarly to tau, forming envelopes on taxol-lattice but not on GMPCPP-lattice microtubules. Conversely, we did not observe envelope formation on either lattice with MAP4, but rather uniform binding along the microtubule length (Fig. 3b and Supplementary Fig. 3a). Quantification of MAP intensity on both types of lattices revealed that the MAP2c level outside of the envelopes was identical to that on GMPCPP-lattice microtubules, similar to tau[9]. The intensity of MAP4 was identical on either type of lattice (Fig. 3b), further suggesting that MAP4 cannot form envelopes.

We next examined these MAPs on taxol-lattices at the single-molecule level. At picomolar concentrations, both MAP2c and MAP4 molecules showed predominantly diffusive interactions with microtubules (Supplementary Fig. 3a). To probe for concentration-dependent effects on single-molecule behavior, we used higher concentrations of GFP-MAP2c or GFP-MAP4 and added picomolar concentrations of fluorescent TMR-labeled MAP2c or MAP4. The diffusive behavior of TMR-MAP2c outside of the GFP-MAP2c envelopes did not change with increasing concentrations of GFP-MAP2c. However, TMR-MAP2c molecules transitioned to static binding within the GFP-MAP2c envelopes (Supplementary Fig. 3a), their dwell times increasing roughly threefold (Supplementary Fig. 3a,b), as observed for tau[9,28]. By contrast, TMR-MAP4 molecules remained diffusive regardless of the concentration (Supplementary Fig. 3a), consistent with its inability to form envelopes. To further explore the dynamics of these MAPs on taxol-lattices, we performed fluorescence recovery after photobleaching (FRAP) experiments. Similar to previous observations with tau[9], MAP2c molecules turned over approximately fourfold faster when they resided outside versus inside envelope boundaries (Supplementary Fig. 3c). By contrast, MAP4 showed homogenous behavior with a recovery time and mobile fraction comparable to envelope-associated MAP2c, in accordance with the observed roughly twofold longer dwell times for single MAP4 molecules versus MAP2c (Supplementary Fig. 3b).

Fig. 2 | Lattice expansion induces disassembly of tau envelopes. a, Fluorescence micrographs of tau-mCherry envelopes on GMPCPP-capped GDP-lattice microtubules before, during, and after hydrodynamic flow removing tau at $t = 0$ s. During the hydrodynamic flow we either added 10 µM taxol (top panels) or kept the measurement buffer taxol-free (bottom). Yellow arrows indicate the location of the bend induced by the flow and the subsequent local decrease in tau density. Scale bars, 5 µm. **b**, Relative density of tau-mCherry in the bend of GMPCPP-capped GDP-lattice microtubules, during and after the flow. With taxol in solution the density dropped to 45.9 ± 15.9% during flow (mean ± s.d., $n = 11$ microtubules, 5 experiments) and decreased further to 3.6 ± 2.8% after flow (mean ± s.d., $n = 11$ microtubules, 5 experiments). Without taxol in solution the density dropped to 53.5 ± 10.4% during hydrodynamic flow (mean ± s.d.; $n = 11$ microtubules, 4 experiments) and recovered to 77.3 ± 10.8% after flow (mean ± s.d.; $n = 11$ microtubules, 4 experiments). **c**, Schematics of the optical tweezers assay. **d**, Fluorescence micrographs of a biotin-HiLyte647-labeled taxol-lattice microtubule suspended between two beads after addition of 60 nM tau-mCherry. Yellow arrows indicate locations of the tau envelopes. Scale bar, 2 µm. **e**, Compaction of taxol-lattice microtubules measured after the addition of either 60 nM tau-mCherry (green) or 0 nM tau-mCherry (gray). Compaction with tau in was 0.48 ± 0.32% (mean ± s.d., $n = 26$ microtubules, 26 experiments). Without tau in solution the microtubule did not compact; −0.01 ± 0.07% (mean ± s.d., $n = 23$ microtubules, 23 experiments, two-sided t-test, $P < 0.001$). **f**, Representative force–time (blue) and distance–time (purple) graphs of a single taxol-lattice microtubule after addition of 60 nM tau-mCherry. After tau addition (green arrow) a decrease in the distance and an increase in the force is detected. After tau was removed from the channel (gray arrow) an increase in the distance, and a decrease in the force is detected, indicating relaxation of the microtubule lattice as tau envelopes disassembled. **g**, Fluorescence micrographs of tau envelope disassembly where the microtubule is stretched using external force. Sketches of the micrographs (left) indicate the size and positions of the tau envelopes (green lines). Scale bars, 2 µm. **h**, Disassembly rate of tau envelopes on taxol-lattice microtubules either stretched by an external force (blue, 0.11 ± 0.06 µm s^{-1}, mean ± s.d., $n = 24$ microtubules, 24 experiments) or relaxed when no external force is applied (gray, 0.05 ± 0.02 µm s^{-1}, mean ± s.d., $n = 18$ microtubules, 18 experiments, two-sided t-test, $P < 0.001$). **i**, Fluorescence micrographs of a tau envelope disassembly experiment where the microtubule is relaxed in absence of external force. Sketches of the micrographs (left) indicate the sizes and positions of the tau envelopes (green lines). Scale bars, 2 µm.

Tau envelopes are sensitive to the aliphatic alcohol 1,6-hexanediol (1,6-HD), a compound that disrupts phase-separated systems in a variety of biological contexts[9], revealing that they share some material properties with these systems. Similar to tau[9], MAP2c envelopes dissolved when exposed to 1,6-HD, but the diffusive fraction of MAP2c molecules remained unchanged (Fig. 3c and Supplementary Fig. 3b). MAP2c envelopes were not dissolved by the 1,6-HD isomer 2,5-hexanediol (Fig. 3c), revealing tau and MAP2c's sensitivity to 1,6-HD is similar to phase-separated systems[32]. By contrast, 1,6-HD had no effect on the binding of MAP4 to microtubules, further demonstrating the distinct biophysical properties of MAP4 (Fig. 3c and Supplementary Fig. 3b).

We next tested the effect of MAP2c or MAP4 on microtubule lattice spacing. First, we mixed each MAP with SiR-tubulin and measured the average SiR-tubulin intensity along microtubules. Similar to tau (Fig. 1i), the presence of MAP2c decreased SiR-tubulin binding by over threefold, while MAP4 had no effect (Fig. 3d). We next measured microtubule compaction by tracking fluorescent speckles on taxol-lattice microtubules upon addition of MAPs (Supplementary Fig. 1j,k). Similar to tau, we observed

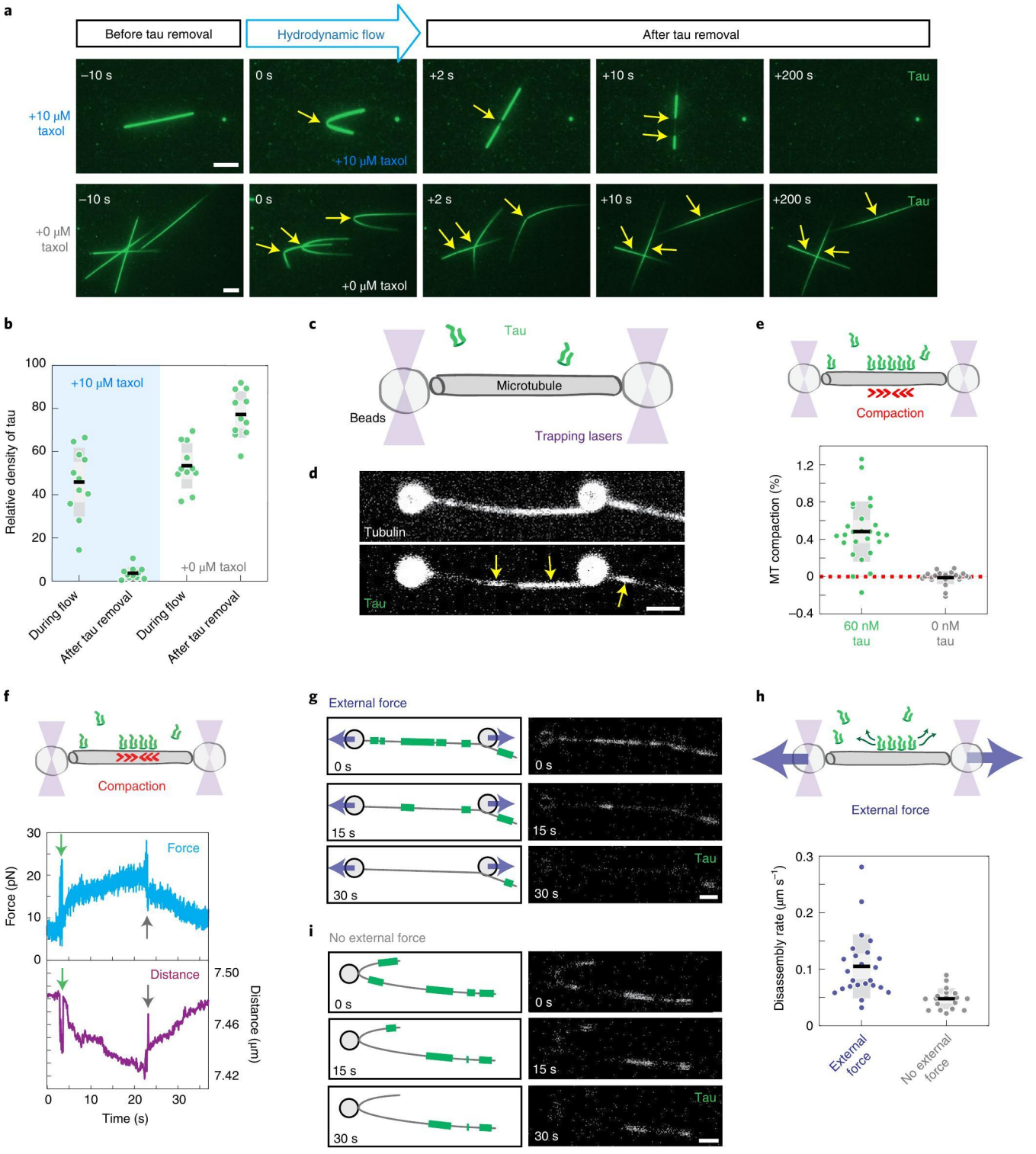

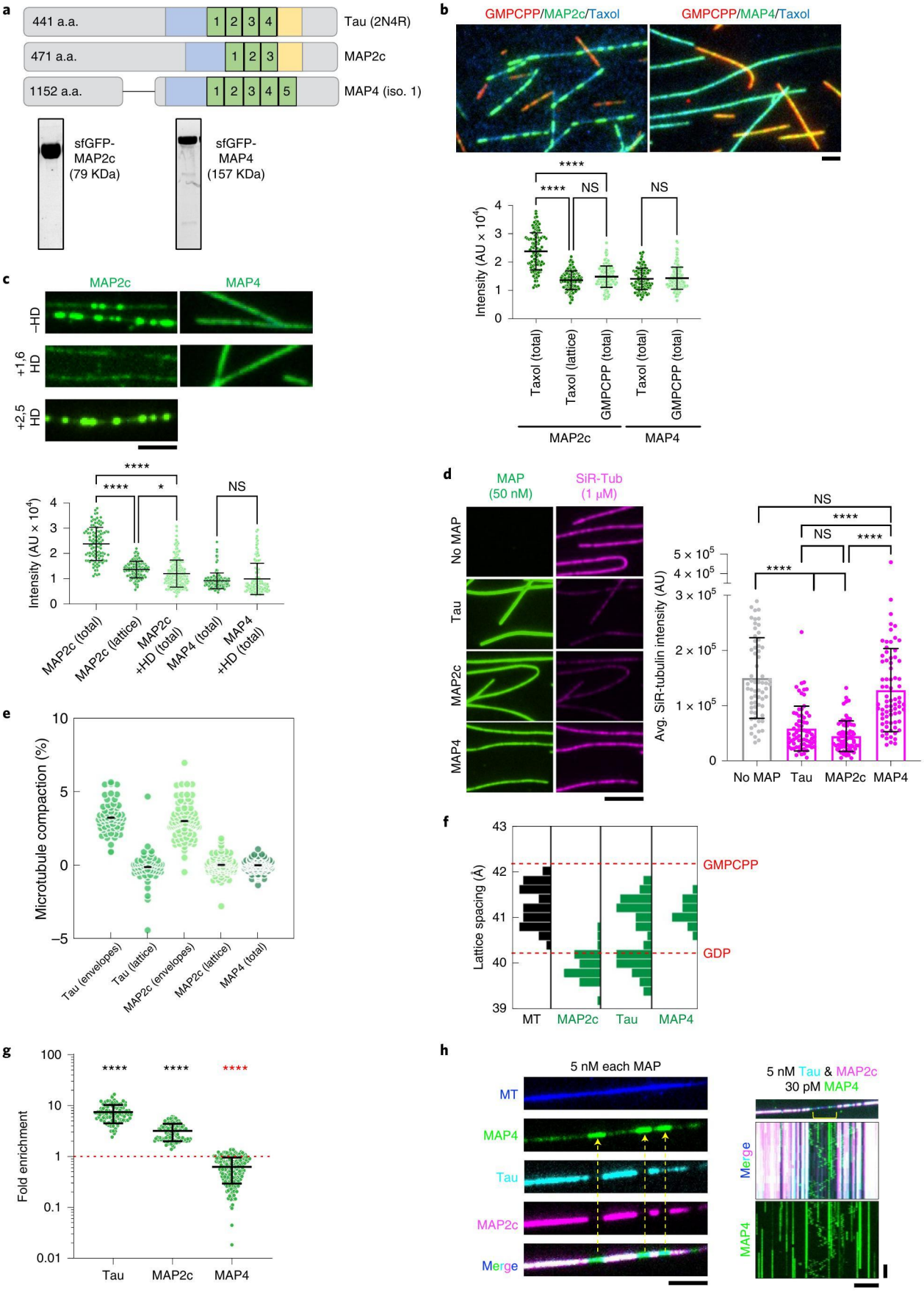
a
441 a.a.
1 2 3 4
Tau (2N4R)
471 a.a.
1 2 3
MAP2c
1152 a.a.
1 2 3 4 5
MAP4 (iso. 1)
sfGFP-MAP2c (79 KDa)
sfGFP-MAP4 (157 KDa)
b
GMPCPP/MAP2c/Taxol
GMPCPP/MAP4/Taxol
Intensity (AU x 10^4)
Taxol (total)
Taxol (lattice)
GMPCPP (total)
MAP2c
MAP4
c
MAP2c
MAP4
–HD
+1.6 HD
+2.5 HD
Intensity (AU x 10^4)
MAP2c (total)
MAP2c (lattice)
MAP2c +HD (total)
MAP4 (total)
MAP4 +HD (total)
d
MAP (50 nM)
SiR-Tub (1 μM)
No MAP
Tau
MAP2c
MAP4
Avg. SiR-tubulin intensity (AU)
e
Microtubule compaction (%)
Tau (envelopes)
Tau (lattice)
MAP2c (envelopes)
MAP2c (lattice)
MAP4 (total)
f
Lattice spacing (Å)
GMPCPP
GDP
MT
MAP2c
Tau
MAP4
g
Fold enrichment
Tau
MAP2c
MAP4
h
5 nM each MAP
MT
MAP4
Tau
MAP2c
Merge
5 nM Tau & MAP2c
30 pM MAP4
Merge
MAP4

Fig. 3 | Cooperative envelope formation is a divergent property within the tau family. a, Schematics of the MAP proteins analyzed, highlighting the conserved microtubule-binding regions (green), proline-rich region (blue), and pseudo-repeat (yellow). Bottom, Coomassie-stained gels showing purity of the MAP2c and MAP4 proteins used. See Source Data for the uncropped gels. a.a., amino acids. **b**, Multi-channel fluorescence micrographs showing the binding of 0.5 nM GFP-MAP2c or GFP-MAP4 (green) to either taxol-lattice (blue) or GMPCPP-lattice microtubules (red). Note the clear formation of envelopes by MAP2c on taxol-lattice, but not on GMPCPP-lattice microtubules. Bottom, quantification of the fluorescence intensity of MAPs on the indicated lattices (mean ± s.d., $n = 108$, 134, 116, 106, and 150 microtubule segments in 3 chambers each.). 'Total' refers to the intensity on the entire lattice including regions outside and inside envelopes for MAP2c. Scale bar, 2 µm. One-way analysis of variance (ANOVA), $^{****}P < 0.001$. n.s., not significant. **c**, Fluorescence images of 0.25 nM GFP-MAP proteins on taxol-lattice microtubules in the absence or presence of 10% 1,6-hexanediol or 2,5-hexanediol (HD). Bottom, quantification of the fluorescence intensity of MAPs in the indicated conditions (mean ± s.d., $n = 108$, 134, 199, 146, and 125 microtubule segments, respectively, 2 experiments each). One-way ANOVA, $^{****}P < 0.001$. **d**, Example fluorescence images showing GFP-MAP (green) and SiR-tubulin (magenta) signals along microtubules. Right, quantification of average SiR-tubulin fluorescence intensity (mean ± s.d., $n = 65$, 74, 72, and 70 microtubule segments, respectively, 2 experiments each). One-way ANOVA, $^{****}P < 0.001$. **e**, Compaction of the microtubule lattice measured on speckled microtubules (same method as data presented in Fig. 1h) after the addition of MAPs. For MAP2c, compaction was 3.0 ± 1.1 % in the envelope regions and 0.0 ± 0.6 % on the lattice outside the envelopes (mean ± s.d., $n = 78$ envelopes, $n = 95$ lattices, in 5 experiments). For MAP4, compaction was 0.0 ± 0.4 % ($n = 105$ microtubules in 11 experiments). **f**, Quantification of the tubulin monomer spacing from cryo-EM images of taxol-lattice microtubules in the absence or presence of the indicated MAPs ($n = 46$, 36, 44, 61, and 30 microtubules, respectively). Red lines denote previously reported tubulin spacing for the indicated lattices[5]. **g**, Quantification of the enrichment of GFP-MAPs, on the basis of fluorescence intensity, within mScarlet-2N4R tau envelopes (mean ± s.d., $n = 97$, 115, 94, 112, 206, and 183 tau envelopes, respectively, 2 experiments each). MAP protein (0.5 nM) was used for each condition. Note that MAP4 values below 1 indicates the protein is excluded from tau envelopes (red asterisks). One-way ANOVA, $^{****}P < 0.001$. **h**, Multi-channel fluorescence micrograph showing all three orthogonally-labeled MAPs mixed together on microtubules. Arrows denote the exclusion of MAP4 from the regions enriched with both tau and MAP2c. Scale bar, 5 µm. Right, TIRF image showing a single microtubule coated in tau/MAP2c envelopes. Kymograph below shows the behavior of single MAP4 molecules (green) visualized at a lower concentration, revealing that they diffuse outside (yellow bracket) but not inside tau/MAP2c envelopes (cyan and magenta). $N = 2$ experiments. Kymograph scale bars, 5 µm, 10 s.

compaction within MAP2c envelopes, but not outside (Fig. 3e). By contrast, we observed no microtubule compaction upon the addition of MAP4. To confirm these results, we performed cryo-EM analysis of taxol-microtubules in the presence of MAPs to directly measure the tubulin spacing within the lattice. Consistent with their ability to form envelopes, we found that both tau and MAP2c binding resulted in ~1 Å compaction between tubulin monomers, consistent with previous cryo-EM measurements between GDP and GTP-like lattices[1] (Fig. 3f). For tau, we observed a bimodal distribution of lattice spacing, suggesting that the lattice was not covered entirely in tau envelopes under our conditions. Addition of MAP2c caused a more complete compaction, to a level consistent with the compacted tau lattice (Fig. 3f). By contrast, addition of MAP4 did not result in measurable compaction within the tubulin lattice (Fig. 3f), consistent with the rest of our observations that MAP4 does not form envelopes on microtubules.

Given their distinct modes of binding, we wondered how the three members of the tau family co-exist on microtubules. We first mixed tau with either differentially-labeled tau, MAP2c or MAP4 and measured how enriched each molecule became within tau envelopes. As expected[9], tau was highly co-enriched within tau envelopes (Fig. 3g). Strikingly, MAP2c co-localized with the tau envelopes, where it was strongly enriched (Fig. 3g) showing that tau and MAP2c can form miscible MAP envelopes. By contrast, MAP4 was largely excluded from tau envelopes (Fig. 3g). To further confirm this result, we co-mixed all three MAPs at equimolar concentrations and observed strong co-segregation of tau and MAP2c into envelopes that excluded MAP4 into the surrounding regions (Fig. 3h). Dilution of MAP4 to single-molecule levels in these conditions revealed that, while single MAP4 molecules diffused on the microtubule lattice outside of tau/MAP2c envelopes, they were unable to diffuse into the tau/MAP2c envelopes (Fig. 3h). Further, individual MAP4 molecules located within the tau/MAP2c envelopes remained static, demonstrating that tau/MAP2c envelopes exclude MAP4 at their boundaries and restrict the dynamics of MAP4 within. Combined, these data reveal that like tau, MAP2c forms envelopes, which compact an extended microtubule lattice. By contrast, MAP4 does not form cohesive envelopes in any condition tested, and is unable to affect the structure of the lattice, suggesting functional diversification within the tau family related to the ability to both recognize and alter the conformation of the microtubule lattice.

Lattice spacing governs MAP cooperativity in vivo. Our results show that compacted microtubule lattices induce cooperative binding of tau, and that extending microtubule lattices induces disassembly of tau envelopes in vitro. Since the majority of tubulin incorporated

Fig. 4 | Lattice spacing governs MAP cooperativity in vivo. a, Time-lapse micrographs of U-2 OS cells expressing eGFP-tau treated with 0.01 µM taxol (top) or DMSO (bottom). Expanded views of the indicated region are provided in the top left corner of the original micrograph. Scale bars, 10 µm. **b**, Coefficient of variation of eGFP-tau cells 10 min after taxol or DMSO treatment, normalized to the coefficient of variation before treatment (at $t = -1$ min). Coefficient of variation was calculated over the whole cell (eGFP-tau after taxol treatment: 66.6 ± 8.0 (mean ± s.d.); $n = 18$ cells, 5 experiments; eGFP-tau after DMSO treatment: 96.8 ± 11.8 (mean ± s.d.); 17 cells, 7 experiments, two-sided t-test, $P < 0.0001$). **c**, Time lapse micrographs of U-2 OS cells expressing eGFP-MAP4 treated with 0.01 µM taxol (top) or DMSO (control, bottom). Expanded views of the indicated regions are provided in the top left corner of the original micrograph. Scale bars, 10 µm. **d**, Coefficient of variation of eGFP-MAP4 cells 10 min after taxol or DMSO treatment, normalized to the coefficient of variation before the same treatment (at $t = -1$ min). The coefficient of variation was calculated over the whole cell (eGFP-MAP4 after taxol treatment: 93.8 ± 20.4 (mean ± s.d.); $n = 23$ cells, 5 experiments; eGFP-MAP4 after DMSO treatment: 92.7 ± 7.5 (mean ± s.d.); $n = 23$ cells, 5 experiments, two-sided t-test, $P = 0.7936$). **e**, Expanded view from a movie as shown in **a** showing the progression of tau signal on a single microtubule (yellow arrowhead) initially fully covered by eGFP-tau after taxol treatment. Sketches of the micrographs (panels next to the original micrographs) indicate the size and locations of fissures in tau signal that appear after taxol treatment. Scale bar, 2 µm. **f**.,Fluorescence kymograph of the microtubule presented in **e** showing the fissures (yellow arrows) appearing in the eGFP-tau signal and the disassembly of the tau envelopes from their boundaries. Scale bars, horizontal 1 µm, vertical 10 s. **g**, Fluorescence kymograph of tau envelope disassembly in vitro showing striking resemblance with the in vivo observations in **f**. Scale bars, horizontal 2 µm, vertical 10 s.

to microtubules in vivo is thought to be in the compacted GDP state, our results suggest that the majority of tau in vivo is bound to microtubules cooperatively. To test this hypothesis, we aimed to induce tau envelope disassembly by extending the microtubule lattices in living cells using taxol. We imaged U-2 OS cells expressing eGFP-tau and observed that 94% of all cells (total $n = 18$ cells, 5 experiments), covering a 20-fold range of expression levels, exhibited eGFP-tau levels high enough that microtubules were fully covered by tau. In the remaining 6% of cells, exhibiting weak eGFP-tau expression, tau only localized to the microtubule bends, as described previously[33,34].

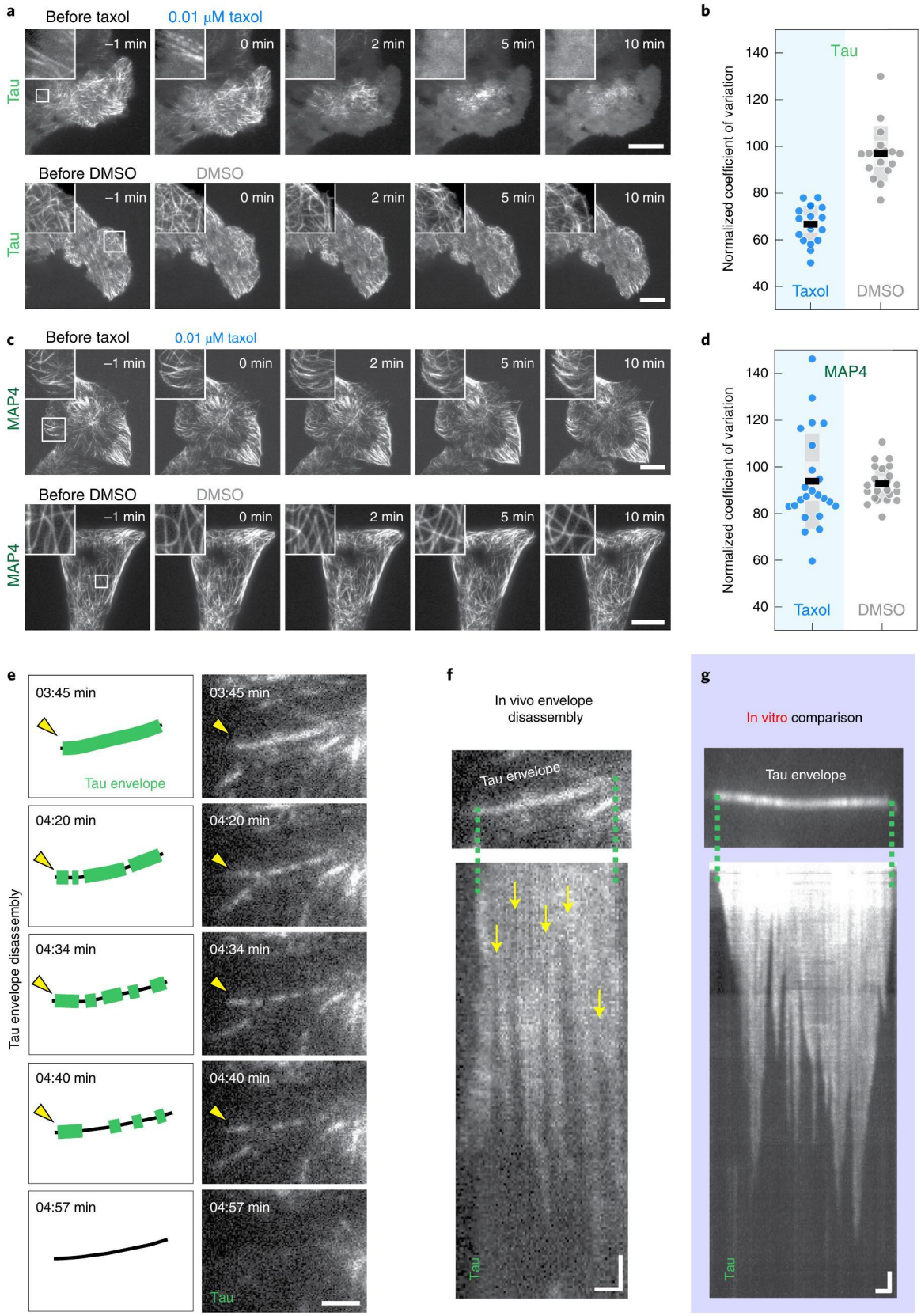

We added 0.01 µM taxol to the medium and imaged the cells for 10 min while monitoring the tau density on microtubules initially fully covered by eGFP-tau. In line with our in vitro observations, and previous in vivo evidence[33,35], we observed that in all cells tau dissociated from the microtubules (Fig. 4a and Supplementary Movie 9) as quantified by the decrease in the coefficient of variation of the tau signal (Fig. 4b). Tau remained on the microtubules when only dimethyl sulfoxide (DMSO) was added to the medium, and the coefficient of variation remained largely unchanged (Fig. 4a,b and Supplementary Movie 10), showing that the dissociation of tau from microtubules is specific to taxol treatment. Staining the cells for α-tubulin, or co-transfecting the cells with eGFP-tau and mScarlet-α-tubulin, verified that microtubules were not disrupted by either treatment (Supplementary Fig. 4a–c). We repeated this experiment with U-2 OS cells expressing eGFP-MAP4. In contrast to tau and in line with previous in vivo evidence[35], we found that MAP4 remained on the microtubules after either treatment with DMSO or taxol (Fig. 4c, and Supplementary Movies 11 and 12), as quantified by the unchanged coefficient of variation (Fig. 4d).

Importantly, when analyzing the tau dissociation during the taxol-driven extension of the native compacted microtubule lattice, we found that the tau signal disappeared from the microtubules in patterns that resembled the disassembly of tau envelopes in vitro[9,28]. Without substantial changes in the initial tau density on the microtubule, fissures in the tau signal appeared, which increased in size over time. The distinct regions of tau signal formed by these fissures then disassembled from their boundaries until they disappeared, similar to tau envelope disassembly in vitro (Fig. 4e–g, Supplementary Fig 4d–f, and Supplementary Movies 13–15). If tau would have been bound non-cooperatively, we would expect tau to unbind from the microtubules uniformly along the microtubule length, as observed for non-cooperatively bound tau in vitro[28]. However, in cells treated with taxol we always observed envelope-like disassembly, rather than uniform tau unbinding. We thus conclude that the vast majority of tau in U-2 OS cells was cooperatively bound to microtubules, and that artificial lattice extension by taxol reveals this cooperative binding through envelope dissolution. These results suggest that native GDP-microtubule lattices in vivo can be fully enclosed by tau envelopes.

MAP cooperativity differentially regulates motor proteins. We next aimed to determine the functional implications for the different microtubule-binding behaviors we observed. We investigated how MAP2c and MAP4 affected the motility of the retrograde microtubule motor complex, dynein–dynactin–Hook3 (DDH), and the anterograde kinesin-3 microtubule motor, KIF1A. In our assays, DDH complexes bound and moved processively along microtubules in the absence and presence of both MAP2c and MAP4 (Fig. 5a). We found that at the highest concentrations of MAPs tested, MAP4, but not MAP2c, decreased the number of processive dynein motors on the microtubule (Fig. 5a,b). At low concentrations of MAP2c, where envelope boundaries are visible, we observed occasional pausing of DDH complexes at the envelope boundary (Fig. 5a), similar to previous observations with tau[9]. Neither MAP strongly affected the average velocity (including pauses) of these motors (Fig. 5c). We analyzed the pixel-by-pixel correlation between the averaged intensities of the MAPs and DDH (Methods). We found no observable negative correlation (Fig. 5d), suggesting that neither MAP strongly affects the spatial distribution of the motors along microtubules. The modest effect of MAP4 on the DDH landing rate may be consistent with prior results[18,19], which suggested MAP4 could inhibit dynein-based movements. The landing rate of dynein–dynactin complexes is strongly determined by the $p150^{glued}$ subunit of the dynactin complex[36], and we speculate that MAP4 may directly affect the interaction of $p150^{glued}$ with the microtubule.

We next examined KIF1A, a neuronal cargo transporter critical for human health[37–40] and sensitive to the nucleotide state of the microtubule lattice[11]. KIF1A motors bound and moved along microtubules in the absence and presence of low concentrations of MAP2c and MAP4 (Fig. 5e). However, at higher concentrations these MAPs strongly decreased the number of processive motors without changing the velocity of motors that were able to bind (Fig. 5e–g). These observations indicate that both MAPs strongly affect the landing rate of the KIF1A motors. In contrast to DDH, we observed a strong spatial effect of MAP2c on KIF1A (Fig. 5e,h). The average pixel intensities of KIF1A were negatively correlated with the average intensities of MAP2c at both concentrations tested, whereas we did not observe a negative correlation between KIF1A and MAP4 (Fig. 5h). These results indicate that cooperative envelope formation facilitates spatial regulation of the KIF1A motor along the microtubule, and demonstrate that MAP2c and MAP4 exert different effects on retrograde and anterograde motors.

Discussion

Cooperative binding of tau and MAP2c to microtubules both requires and, reciprocally, induces a local compaction of the

Fig. 5 | MAP cooperativity results in differential regulation of motor proteins. a, Fluorescence micrographs showing microtubules (blue) and GFP-MAPs (green). Below each condition is a representative kymograph showing TMR-DDH (magenta) behavior. Red arrow denotes a pausing event. Scale bars, horizontal 5 µm, vertical 10 s. Note kymographs do not directly correlate with example images above. **b**, Quantification of the number of processive TMR-DDH complexes observed at the highest concentration of each GFP-MAP examined. Bars show averages with s.d., magenta dots show individual measurement values, $n = 24$, 35, and 26 microtubules quantified from two independent trials each. One-way ANOVA, $^{**}P = 0.0014$. **c**, Quantification of TMR-DDH velocities in the indicated conditions. Bars show averages with s.d., magenta dots show individual measurement values: $n = 201$, 174, 143, 175, and 121 DDH complexes respectively, 2 experiments each. One-way ANOVA, $^{****}P < 0.0001$. **d**, Graphs displaying individual *xy* pairs per pixel for average GFP-MAP2c or GFP-MAP4 intensity versus average TMR-DDH intensity along the microtubule, fit with linear regression. Pearson's correlation coefficients: −0.09669 and 0.01279 for 2.5 and 12.5 nM MAP2c respectively, and 0.1957 and 0.1671 for 2.5 and 12.5 nM MAP4 respectively. $n = 1{,}337$ and 1,557 *xy* pairs from $n = 10$ microtubules, 2 experiments for 2.5 nM and 12.5 nM MAP2c. $n = 1{,}648$ and 1,193 *xy* pairs from $n = 10$ microtubules, 2 experiments for 2.5 and 12.5 nM MAP4. $P = 0.004$, 0.6121, <0.001, and <0.001 for each 2.5, 12,5, 2.5, and 12.5 nM MAP2c and MAP4, respectively. **e**, Representative fluorescence micrographs showing microtubules (blue) and GFP-MAPs (green). Below each condition is a representative kymograph showing mScarlet-KIF1A (magenta) behavior. Scale bars, horizontal 5 µm, vertical 10 s. **f**, Quantification of the number of processive mScarlet-KIF1A motors observed at the highest concentration of each GFP-MAP examined. Bars show averages with s.d., magenta dots show individual measurement values: $n = 18$, 26, and 30 microtubules, 2 experiments each. One-way ANOVA, $^{****}P < 0.0001$. **g**, Quantification of mScarlet-KIF1A velocities in the indicated conditions. Bars show averages with s.d., magenta dots show individual measurement values: $n = 158$, 235, 138, 199, and 151 KIF1A motors, respectively, 2 experiments each. One-way ANOVA. **h**, Graphs displaying individual *xy* pairs per pixel for average GFP-MAP2c or GFP-MAP4 intensity versus average mScarlet-KIF1A intensity along the microtubule, fit with linear regression lines. Pearson's correlation coefficients: −0.7620 and −0.6709 for 2.5 and 12.5 nM MAP2c, respectively, and 0.1237 and 0.1201 for 2.5 and 12.5 nM MAP4, respectively. $n = 1{,}243$ and 1,354 *xy* pairs, 10 microtubules, 2 experiments for 2.5 nM and 12.5 nM MAP2c. $n = 1{,}574$ and 1,121 xy pairs, 10 microtubules, 2 experiments for 2.5 and 12.5 nM MAP4. $P = <0.0001$, <0.001, <0.0001, and <0.0001 for each 2.5, 12,5, 2.5, and 12.5 nM MAP2c and MAP4, respectively.

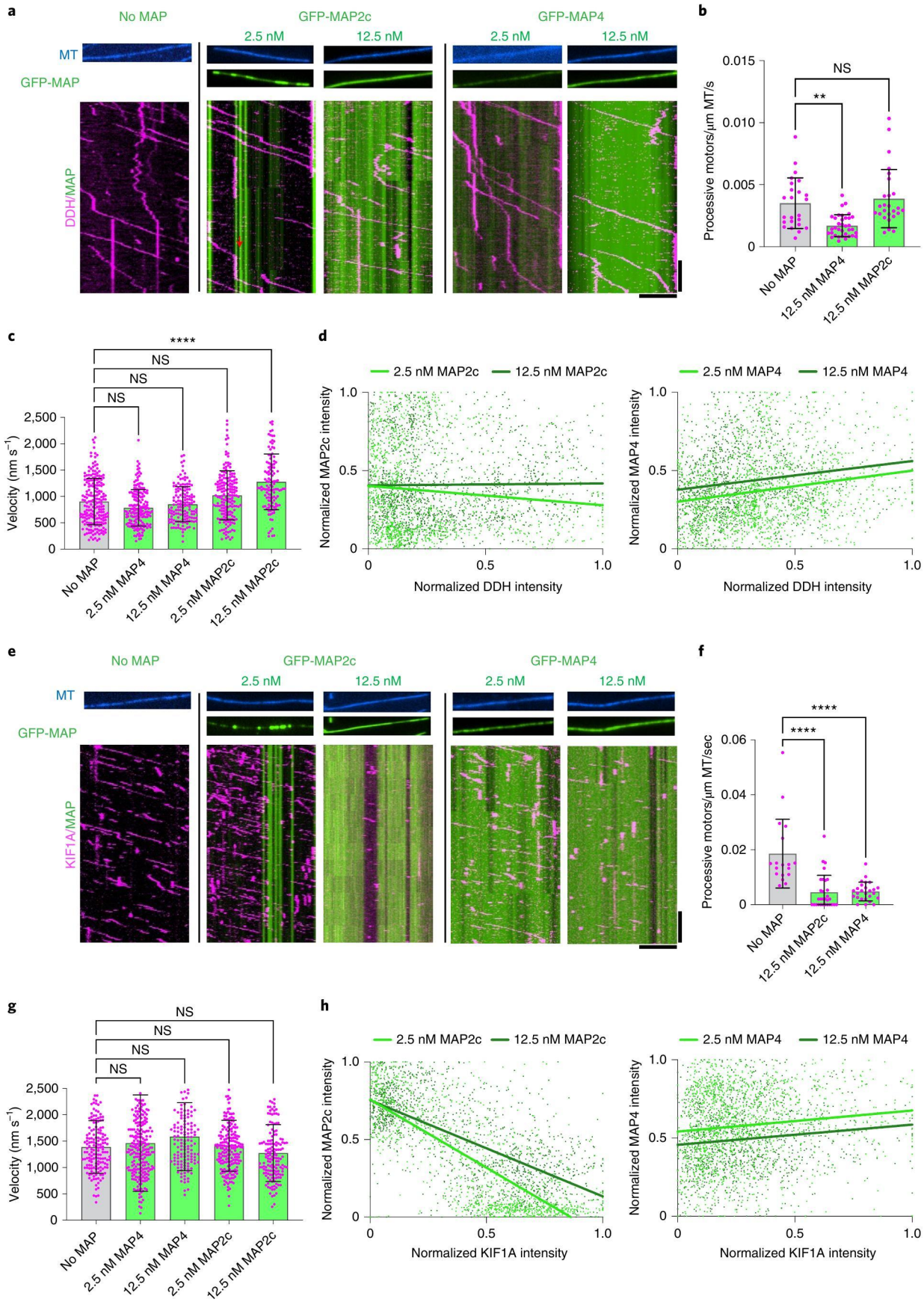
a
No MAP
GFP-MAP2c
2.5 nM
12.5 nM
GFP-MAP4
2.5 nM
12.5 nM
MT
GFP-MAP
DDH/MAP
b
Processive motors/μm MT/s
0.015
0.010
0.005
0
NS
**
No MAP
12.5 nM MAP4
12.5 nM MAP2c
c
Velocity (nm s−1)
2,500
2,000
1,500
1,000
500
0
****
NS
NS
NS
No MAP
2.5 nM MAP4
12.5 nM MAP4
2.5 nM MAP2c
12.5 nM MAP2c
d
2.5 nM MAP2c
12.5 nM MAP2c
Normalized MAP2c intensity
Normalized DDH intensity
2.5 nM MAP4
12.5 nM MAP4
Normalized MAP4 intensity
Normalized DDH intensity
e
No MAP
GFP-MAP2c
2.5 nM
12.5 nM
GFP-MAP4
2.5 nM
12.5 nM
MT
GFP-MAP
KIF1A/MAP
f
Processive motors/μm MT/sec
0.06
0.04
0.02
0
****
****
No MAP
12.5 nM MAP2c
12.5 nM MAP4
g
Velocity (nm s−1)
2,500
2,000
1,500
1,000
500
0
NS
NS
NS
NS
No MAP
2.5 nM MAP4
12.5 nM MAP4
2.5 nM MAP2c
12.5 nM MAP2c
h
2.5 nM MAP2c
12.5 nM MAP2c
Normalized MAP2c intensity
Normalized KIF1A intensity
2.5 nM MAP4
12.5 nM MAP4
Normalized MAP4 intensity
Normalized KIF1A intensity

underlying microtubule lattice. We propose to use the term 'envelopes' for these microtubule-dependent structures to distinguish them from soluble tau droplets, often termed 'condensates', which form independent of the microtubule lattice[22–24]. We hypothesize that MAP-driven compaction of the lattice might allosterically alter the conformation of the regions of lattice adjoining the boundaries of the envelope. This could be mediated by the conserved microtubule-binding repeats, which span several tubulin dimers[41]. This 'through the lattice' allostery might locally increase the affinity for new MAP molecules binding proximal to the envelope boundaries, as previously proposed for kinesin motors[4,6,42] and microtubule dynamics[43]. Additionally, direct MAP–MAP interactions might facilitate the preferential binding of MAP molecules at the envelope boundaries. These interactions might be mediated by the regions flanking the microtubule-binding repeats of tau or MAP2, as these domains are required for envelope formation[9,28]. Additionally, our 1,6-hexanediol experiments suggest that phase separation of tau and MAP2 on the microtubule surface might contribute to cooperative envelope formation. MAP4 adopts a conformation completely distinct from that of tau[41,44] on microtubules, which may at least partially explain why, unlike tau, MAP4 is unable to form envelopes.

Our data suggests that tau and MAP2, but not MAP4, are sensitive to the mechanical state of the microtubule lattice, and thus are suited to function as mechanosensitive MAPs. This observation may have physiological relevance in muscle cells where isoforms of MAP4 are abundantly expressed, and there are several reports of tau expression in various types of muscle tissue[15,45,46]. Additionally, mechanosensitivity could be an important feature in the developing nervous system during cell polarization or cell migration.

Mammalian tubulin within the GDP-lattice primarily adopts compacted state, whereas the newly incorporated GTP-tubulin adopts an expanded state[1]. Intriguingly, in non-mammalian species, microtubule lattice compaction does not appear to be directly coupled to GTP hydrolysis[47,48]. Additionally, recent evidence suggests that the microtubule lattice is not conformationally homogenous, but rather releases and incorporates new GTP-tubulin subunits in response to mechanical damage and repair[49]. Thus, the microtubule lattice in living cells may not exist in a homogenously compacted, GDP state, as previously thought. We suggest it is plausible that MAPs that recognize and alter the compaction state of the lattice, such as tau and MAP2, may play active roles in biasing the conformational dynamics of tubulin within the lattice. It is presumed that the predominant volume of the microtubule lattice in cells is in the GDP compacted state, suggesting that most of tau in cells is bound to the microtubule in a cooperative manner, which is in agreement with our experimental observations in vivo, where tau unbound from microtubules after the addition of taxol. We occasionally observed enriched tau signal in microtubule bends, even after taxol addition, in accordance with previous observations[9,35]. Our results suggest that this is due to tau binding to the compressed lattice on the inner side of the bends. By contrast, at high levels of tau, when the lattice is fully decorated by tau, bending of the lattice leads to local decrease in tau densities[28], which could be explained by the disruption of the tau envelope on stretched lattice on the outer side of the bend.

We demonstrate that MAP envelopes differentially regulate the motility of two predominant microtubule motor systems: dynein-based retrograde, and kinesin-based anterograde transport. Because MAP4 does not form envelopes, it is unable to provide spatially distinct regulation of motors and rather regulates them globally. However, our observation that MAP4 is excluded from tau or MAP2 envelopes raises the possibility that MAP exclusion could act as an extrinsic mechanism to spatially dictate MAP binding within cells. Such a mechanism has also been suggested for tau and MAP7, which have opposite effects on kinesin-1 motility[16]. Why are different classes of kinesin motors unable to access the microtubule lattice under MAP envelopes? Apart from steric clashes between tau and kinesin[9,41], kinesin binding expands the microtubule lattice[4,6] suggesting that exclusive binding may arise from competition for an expanded versus compacted lattice. In previous experiments, MAP4 did not block the binding of a kinesin-1 motor domain to microtubules[44], while we show that it negatively affects KIF1A motility. This distinction could be due to the dominating influence of the k-loop of KIF1A on its landing rate[50]. Our data reveal that tau and MAP2 envelopes spatially gate kinesin access to the microtubule, while allowing dynein to pass. These MAPs are highly enriched within the neuronal system and this capability may be harnessed to spatially regulate microtubule-based trafficking. We hypothesize that the efficiency of cargo trafficking trough MAP envelopes is further modulated by motor-associated proteins[51] and the numbers and types of different motors bound to the cargo. Co-localization of tau and MAP2 into shared envelopes that exclude MAP4 suggests that different MAPs can form spatially distinct domains on the microtubule lattice, differentially regulating access to microtubule surface. Our work raises the hypothesis that the heterogeneity of the MAP envelope may thus provide a means for sectioning the microtubule surface into functionally distinct segments.

Online content

Any methods, additional references, Nature Research reporting summaries, source data, extended data, supplementary information, acknowledgements, peer review information; details of author contributions and competing interests; and statements of data and code availability are available at https://doi.org/10.1038/s41589-022-01096-2.

Received: 5 January 2022; Accepted: 24 June 2022;
Published online: 22 August 2022

References

1. Alushin, G. M. et al. High-resolution microtubule structures reveal the structural transitions in αβ-tubulin upon GTP hydrolysis. *Cell* **157**, 1117–1129 (2014).
2. Hyman, A. A., Salser, S., Drechsel, D. N., Unwin, N. & Mitchison, T. J. Role of GTP hydrolysis in microtubule dynamics: information from a slowly hydrolyzable analogue, GMPCPP. *Mol. Biol. Cell* **3**, 1155–1167 (1992).
3. Díaz, J. F., Barasoain, I. & Andreu, J. M. Fast kinetics of taxol binding to microtubules: effects of solution variables and microtubule-associated proteins. *J. Biol. Chem.* **278**, 8407–8419 (2003).
4. Peet, D. R., Burroughs, N. J. & Cross, R. A. Kinesin expands and stabilizes the GDP-microtubule lattice. *Nat. Nanotechnol.* **13**, 386–391 (2018).
5. Zhang, R., LaFrance, B. & Nogales, E. Separating the effects of nucleotide and EB binding on microtubule structure. *Proc. Natl Acad. Sci.* **115**, E6191–E6200 (2018).
6. Shima, T. et al. Kinesin-binding–triggered conformation switching of microtubules contributes to polarized transport. *J. Cell Biol.* **217**, 4164–4183 (2018).
7. Maurer, S. P., Bieling, P., Cope, J., Hoenger, A. & Surrey, T. GTPγS microtubules mimic the growing microtubule end structure recognized by end-binding proteins (EBs). *Proc. Natl Acad. Sci.* **108**, 3988–3993 (2011).
8. Zanic, M., Stear, J. H., Hyman, A. A. & Howard, J. EB1 recognizes the nucleotide state of tubulin in the microtubule lattice. *PLoS One* **4**, e7585 (2009).
9. Tan, R. et al. Microtubules gate tau condensation to spatially regulate microtubule functions. *Nat. Cell Biol.* **21**, 1078–1085 (2019).
10. Castle, B. T., McKibben, K. M., Rhoades, E. & Odde, D. J. Tau avoids the GTP cap at growing microtubule plus-ends. *iScience* **23**, 101782 (2020).
11. Guedes-Dias, P. et al. Kinesin-3 responds to local microtubule dynamics to target synaptic cargo delivery to the presynapse. *Curr. Biol.* **29**, 268–282 (2019).
12. Dehmelt, L. & Halpain, S. The MAP2/Tau family of microtubule-associated proteins. *Genome Biol.* **6**, 1–10 (2005).
13. Sündermann, F., Fernandez, M. & Morgan, R. An evolutionary roadmap to the microtubule-associated protein MAP Tau. *BMC Genom.* **17**, 264 (2016).
14. Götz, J., Halliday, G. & Nisbet, R. M. Molecular pathogenesis of the tauopathies. *Annu. Rev. Pathol. Mech. Dis.* **14**, 239–261 (2019).
15. Li, L., Zhang, Q., Lei, X., Huang, Y. & Hu, J. MAP4 as a new candidate in cardiovascular disease. *Front. Physiol.* **11**, 1044 (2020).

16. Monroy, B. Y. et al. A combinatorial MAP code dictates polarized microtubule transport. *Dev. Cell* **53**, 60–72 (2020).
17. Seitz, A. et al. Single-molecule investigation of the interference between kinesin, tau and MAP2c. *EMBO J.* **21**, 4896–4905 (2002).
18. Semenova, I. et al. Regulation of microtubule-based transport by MAP4. *Mol. Biol. Cell* **25**, 3119–3132 (2014).
19. Samora, C. P. et al. MAP4 and CLASP1 operate as a safety mechanism to maintain a stable spindle position in mitosis. *Nat. Cell Biol.* **13**, 1040–1050 (2011).
20. Karasmanis, E. P. et al. Polarity of neuronal membrane traffic requires sorting of kinesin motor cargo during entry into dendrites by a microtubule-associated septin. *Dev. Cell* **46**, 204–218 (2018).
21. Bulinski, J. C., McGraw, T. E., Gruber, D., Lan Nguyen, H. & Sheetz, M. P. Overexpression of MAP4 inhibits organelle motility and trafficking in vivo. *J. Cell Sci.* **110**, 3055–3064 (1997).
22. Hernández-Vega, A. et al. Local nucleation of microtubule bundles through tubulin concentration into a condensed Tau phase. *Cell Rep.* **20**, 2304–2312 (2017).
23. Zhang, X. et al. The proline-rich domain promotes Tau liquid–liquid phase separation in cells. *J. Cell Biol.* **219**, e202006054 (2020).
24. Zhang, X. et al. RNA stores tau reversibly in complex coacervates. *PLoS Biol.* **15**, e2002183 (2017).
25. Iqbal, K., Liu, F. & Gong, C.-X. Tau and neurodegenerative disease: the story so far. *Nat. Rev. Neurol.* **12**, 15–27 (2016).
26. Dixit, R., Ross, J. L., Goldman, Y. E. & Holzbaur, E. L. F. Differential regulation of dynein and kinesin motor proteins by tau. *Science* **319**, 1086–1089 (2008).
27. McVicker, D. P., Hoeprich, G. J., Thompson, A. R. & Berger, C. L. Tau interconverts between diffusive and stable populations on the microtubule surface in an isoform and lattice specific manner. *Cytoskeleton* **71**, 184–194 (2014).
28. Siahaan, V. et al. Kinetically distinct phases of tau on microtubules regulate kinesin motors and severing enzymes. *Nat. Cell Biol.* **21**, 1086–1092 (2019).
29. Chaudhary, A. R., Berger, F., Berger, C. L. & Hendricks, A. G. Tau directs intracellular trafficking by regulating the forces exerted by kinesin and dynein teams. *Traffic* **19**, 111–121 (2018).
30. Diaz, J. F. & Andreu, J. M. Assembly of purified GDP-tubulin into microtubules induced by taxol and taxotere: reversibility, ligand stoichiometry, and competition. *Biochemistry* **32**, 2747–2755 (1993).
31. Kar, S., Fan, J., Smith, M. J., Goedert, M. & Amos, L. A. Repeat motifs of tau bind to the insides of microtubules in the absence of taxol. *EMBO J.* **22**, 70–77 (2003).
32. Lin, Y. et al. Toxic PR poly-dipeptides encoded by the C9orf72 repeat expansion target LC domain polymers. *Cell* **167**, 789–802.e12 (2016).
33. Samsonov, A., Yu, J.-Z., Rasenick, M. & Popov, S. V. Tau interaction with microtubules in vivo. *J. Cell Sci.* **117**, 6129–6141 (2004).
34. Balabanian, L., Berger, C. L. & Hendricks, A. G. Acetylated microtubules are preferentially bundled leading to enhanced kinesin-1 motility. *Biophys. J.* **113**, 1551–1560 (2017).
35. Ettinger, A., van Haren, J., Ribeiro, S. A. & Wittmann, T. Doublecortin is excluded from growing microtubule ends and recognizes the GDP-microtubule lattice. *Curr. Biol.* **26**, 1549–1555 (2016).
36. McKenney, R. J., Huynh, W., Vale, R. D. & Sirajuddin, M. Tyrosination of α-tubulin controls the initiation of processive dynein–dynactin motility. *EMBO J.* **35**, 1175–1185 (2016).
37. Lam, A. J. et al. A highly conserved 310 helix within the kinesin motor domain is critical for kinesin function and human health. *Sci. Adv.* **7**, eabf1002.
38. Budaitis, B. G. et al. Pathogenic mutations in the kinesin-3 motor KIF1A diminish force generation and movement through allosteric mechanisms. *J. Cell Biol.* **220**, e202004227 (2021).
39. Chiba, K. et al. Disease-associated mutations hyperactivate KIF1A motility and anterograde axonal transport of synaptic vesicle precursors. *Proc. Natl Acad. Sci.* **116**, 18429–18434 (2019).
40. Boyle, L. et al. Genotype and defects in microtubule-based motility correlate with clinical severity in KIF1A-associated neurological disorder. *Hum. Genet. Genomics Adv.* **2**, 100026 (2021).
41. Kellogg, E. H. et al. Near-atomic model of microtubule–tau interactions. *Science* **360**, 1242–1246 (2018).
42. Wijeratne, S. S., Fiorenza, S. A., Subramanian, R. & Betterton, M. D. Motor guidance by long-range communication through the microtubule highway. Preprint at *bioRxiv* https://doi.org/10.1101/2020.12.23.424221 (2020).
43. Kim, T. & Rice, L. M. Long-range, through-lattice coupling improves predictions of microtubule catastrophe. *Mol. Biol. Cell* **30**, 1451–1462 (2019).
44. Shigematsu, H. et al. Structural insight into microtubule stabilization and kinesin inhibition by Tau family MAPs. *J. Cell Biol.* **217**, 4155–4163 (2018).
45. Gu, Y., Oyama, F. & Ihara, Y. Tau is widely expressed in rat tissues. *J. Neurochem.* **67**, 1235–1244 (1996).
46. Shults, N. V. et al. Tau protein in lung smooth muscle cells. *J. Respir.* **1**, 30–39 (2020).
47. Howes, S. C. et al. Structural differences between yeast and mammalian microtubules revealed by cryo-EM. *J. Cell Biol.* **216**, 2669–2677 (2017).
48. Chaaban, S. et al. The structure and dynamics of *C. elegans* tubulin reveals the mechanistic basis of microtubule growth. *Dev. Cell* **47**, 191–204 (2018).
49. Triclin, S. et al. Self-repair protects microtubules from destruction by molecular motors. *Nat. Mater.* **20**, 883–891 (2021).
50. Soppina, V. & Verhey, K. J. The family-specific K-loop influences the microtubule on-rate but not the superprocessivity of kinesin-3 motors. *Mol. Biol. Cell* **25**, 2161–2170 (2014).
51. Henrichs, V. et al. Mitochondria-adaptor TRAK1 promotes kinesin-1 driven transport in crowded environments. *Nat. Commun. 2020 111* **11**, 1–13 (2020).

Methods

Microtubule assembly. Porcine brains were obtained from a local abattoir and used within ~4 h of death. Porcine brain tubulin was isolated using the high-molarity piperazine-*N*,*N*′-bis(2-ethanesulfonic acid) PIPES procedure then labeled with biotin NHS ester, Dylight-405 NHS ester, Alexa-647 NHS ester, or Atto-647 ester as described previously[52,53]. Biotin-labeled tubulin as well as HiLyte647-labeled tubulin were purchased from Cytoskeleton (T333P and TL670M, respectively).

Taxol-lattice microtubules (GTP polymerized, then taxol stabilized; stored and imaged in presence of taxol) were polymerized from 4 mg ml^{-1} tubulin for 30 min at 37 °C in BRB80 (80 mM PIPES, 1 mM ethylene glycol-bis(2-aminoethylether)-*N*,*N*,*N*′,*N*′-tetraacetic acid (EGTA), 1 mM $MgCl_2$, pH 6.9) supplemented with 4 mM $MgCl_2$, 5% DMSO, and 1 mM GTP (Jena Bioscience, NU-1012). The polymerized microtubules were diluted in BRB80T (BRB80 supplemented with 10 µM taxol (paclitaxel)) and centrifuged for 30 min at 18,000*g* in a Microfuge 18 Centrifuge (Beckman Coulter). After centrifugation the pellet was resuspended and kept in BRB80T.

GMPCPP-lattice microtubules (GMPCPP polymerized) were polymerized from 4 mg ml^{-1} tubulin for 2 h at 37 °C in BRB80 supplemented with 1 mM $MgCl_2$ and 1 mM GMPCPP (Jena Bioscience, NU-405). The polymerized microtubules were centrifuged for 30 min at 18,000*g* in a Microfuge 18 Centrifuge (Beckman Coulter). After centrifugation the pellet was resuspended and kept in BRB80T.

GMPCPP-capped GDP-lattice microtubules (GTP polymerized, GMPCPP-capped) were polymerized from 4 mg ml^{-1} tubulin for 30 min at 37 °C in BRB80 supplemented with 4 mM $MgCl_2$, 5% DMSO, and 1 mM GTP (Jena Bioscience, NU-1012). The polymerized microtubules were centrifuged at 37 °C for 30 min at 18,000*g* in a Microfuge 18 Centrifuge (Beckman Coulter). After centrifugation, the pellet was resuspended and incubated for 20 min at 37 °C in BRB80 supplemented with 100 mM $MgCl_2$, 10 mM GMPCPP and 0.25 mg ml^{-1} tubulin for cap formation.

Speckled microtubules were polymerized as taxol-lattice microtubules prepared from 4 mg ml^{-1} tubulin comprised of 2% biotin-labeled tubulin and 0.133% Atto647-labeled tubulin.

Protein constructs and purification. For in vitro experiments comparing tau family proteins, tau and MAP2c constructs were cloned into pET28A vectors using Gibson assembly. Full-length human MAP4 (isoform 1) was codon optimized for insect cell expression by Epoch Biosciences before cloning into the pFastbac vector. All constructs contain an N-terminal cassette consisting of a 6× His-tag, tandem Strep-tags, and fluorophore or SNAPf tag connected by a GS-linker as previously described[9]. *Mus musculus* MAP2c was acquired from the Ori-McKenney lab[16].

For in vitro experiments, tau[9,22],MAP2c[16], DDH complexes[54], a truncated, constitutively dimerized Kif1A construct[16], and kinesin-1-GFP[51] were expressed and purified as previously described.

MAP4 was expressed in insect cells using the Bac-to-Bac system (Thermo Fisher). Cells were infected at ~2 million cells per milliliter for 60 h before harvesting. Cells were resuspended in lysis buffer (50 mM Tris pH 8, 150mM κ-acetate, 2 mM $MgSO_4$, 1 mM EGTA, 10% glycerol) with protease inhibitor, 1 mM dithiothreitol (DTT), 1 mM phenylmethylsulfonyl fluoride, 1% Triton X-100, and DNaseI, and dounced on ice. Cell lysate, after douncing, was cleared by centrifugation at 14,000*g* for 20 min, and loaded onto Streptactin Superflow resin (Qiagen) and extensively washed with lysis buffer. Bound proteins were eluted with 3 mM desthiobion (sigma) in lysis buffer. Eluted proteins were loaded on cation exchange column 5 ml HiTrapS (GE Healthcare) in lysis buffer pH 7.5 and eluted with 0–0.6 M NaCl gradient over 40 column volumns. Fractions were collected, concentrated, and flash frozen in LN_2.

SNAPf-tagged MAP proteins were labeled by incubation with 2–5 µM SNAP dye at 4 °C for ~2–4 h. Unbound dye was removed by passage through a HiTrap desalting column equilibrated in GF150 buffer (25 mM HEPES pH 7.4, 150 mM KCl, 1 mM $MgCL_2$). Protein was concentrated using Amicon Ultra concentrators (Millipore) and flash frozen in liquid nitrogen and stored at −80 °C.

Total internal reflection fluorescence microscopy. TIRF microscopy experiments were performed on an inverted microscope (Nikon-Ti E, Nikon-Ti2 E) equipped with 60× or 100× NA 1.49 oil immersion objectives (Apo TIRF or SR Apo TIRF, respectively, Nikon) and either Hamamatsu Orca Flash 4.0 sCMOS or PRIME BSI (Teledyne Photometrics) cameras. Or on either of two custom-built through-the-objective TIRF microscope that are based on a Nikon-Ti-E or Ti-2 microscope body, motorized ASI or Nikon stage, quad-band filter cube (Chroma), laser launch (100 mW, 405 nm; 150 mW, 488 nm; 100 mW, 560 nm; 100 mW, 642 nm), EMCCD camera (iXon Ultra 897) and a high-speed filter wheel (Finger Lakes Instruments)[9]. Microtubules and MAPs were visualized sequentially by switching between microscope filter cubes for Cy5, TRITC and FITC channels or by using a quad-band set filter (405/488/561/640). All imaging was performed using a ×100 1.45 NA objective (Nikon) and if necessary, the ×1.5 tube lens setting was used. The microscopes were controlled using Micro-Manager 1.4 or Nikon NIS Elements software. All experiments were conducted at room temperature, if required the sample chamber was kept at 25 °C using an objective warmer (Oko Labs).

TIRF chambers were assembled from acid-washed coverslips as described previously (http://labs.bio.unc.edu/Salmon/protocolscoverslippreps.html) and double-sided sticky tape. Chambers were first incubated with 0.5 mg ml^{-1} PLL-PEG-biotin (Surface Solutions) for 10 min, followed by 0.5 mg ml^{-1} streptavidin for 5 min. Or TIRF chambers were assembled from coverslips silanized with 0.05% dichlorodimethylsilane (DDS, #440272, Sigma) and thin strips of parafilm melted in between two coverslips, as described previously[51]. The chambers were first incubated with 20 µg ml^{-1} anti-biotin antibodies (#B3640, Sigma) for 5 min, followed by 1% F127 (#P2443, Sigma, 1% in phosphate-buffered saline (PBS)) for at least 30 min.

Microtubules were diluted into BC Buffer (80 mM PIPES pH 6.8, 1 mM $MgCl_2$, 1 mM EGTA, 1 mg ml^{-1} bovine serum albumin (BSA), 1 mg ml^{-1} casein and 10 µM taxol) or BRB80T (80 mM PIPES, 1 mM EGTA, 1 mM MgCl2, pH 6.9, 10 µM taxol) then incubated in the chamber and allowed to adhere to the streptavidin-coated surface for 10 min or the antibody-coated surface for 1 min. Unbound microtubules were washed away with TIRF assay buffer AB1 (60 mM HEPES pH 7.4, 50 mM potassium acetate, 2 mM $MgCl_2$, 1 mM EGTA, 10% glycerol, 0.5% Pluronic F127, 0.1 mg ml^{-1} biotin-BSA, 0.2 mg ml^{-1} κ-casein and 10 µM taxol) or BRB80T. Unless otherwise stated, experiments were conducted in imaging buffer IB1 (AB1 supplemented with 2 mM Trolox, 2 mM protocatechuic acid, ~50 nM protocatechuate-3,4-dioxygenase and 2 mM ATP) or assay buffer AB2 (50 mM HEPES pH 7.4, 1 mM EGTA, 2 mM $MgCl_2$, 75 mM KCl, 10 mM dithiothreitol, 0.02 mg ml^{-1} casein, 10 µM taxol, 1 mM Mg–ATP, 20 mM D-glucose, 0.22 mg ml^{-1} glucose oxidase and 20 µg ml^{-1} catalase). All experiments were quantified by pooling data from at least two chambers performed on multiple days.

Fluorescence recovery after photo-bleaching experiments. FRAP experiments were carried out largely as described previously[9]. For the FRAP experiments, chambers were sealed at both sides with vacuum grease. A pre-bleach image was acquired by averaging 12 consecutive images. Then, 8 regions were bleached (1 empty background, 1 unbleached portion of the microtubule, 3 envelopes and 3 lattice or 6 regions on the microtubule in the case of MAP4) at 2% power without scanning; 5 images were taken before stimulation and 91 images were taken after stimulation, all at 1 s intervals. The regions subjected to FRAP were then background subtracted using the empty background region, then normalized to the unbleached portion of the microtubule, and then to the average of the first 12 consecutive images of each region. *N* is defined as the number of bleached regions.

Kinesin-1 on GMPCPP/taxol-lattice microtubules. GMPCPP- and taxol-lattice microtubules were immobilized on the antibody-coated coverslips surface. Six-hundred nanomolar tau-mCherry diluted in AB2 was added to the microtubules before addition of kinesin-1-GFP and incubated for at least 2 min to ensure envelope formation. After incubation, 60 nM kinesin-1-GFP was added to the microtubules in presence of 600 nM tau, diluted in imaging buffer. Imaging of kinesin-1-GFP was performed with 20 ms or 50 ms framerate.

Lattice expansion TIRF assay. DDS-coated coverslips were incubated with low anti-β-tubulin antibody concentration (#T7816, Sigma, 1 µg ml^{-1} in PBS) to ensure low binding of microtubules to the coverslip surface. GMPCPP-capped GDP-lattice microtubules were flushed into the measurement chamber and unbound microtubules were removed with BRB80. Twenty nanomolar tau-mCherry diluted in AB2 was added to the microtubules and incubated for 1–2 min. After incubation, tau was removed from the measurement chamber by introducing 20 µl of tau in AB2 either in presence or absence of taxol (0 or 10 µM taxol).

SiR-tubulin assay. For the data in Fig. 1i, taxol-lattice microtubules were prepared as described above and kept in BRB80T-S (BRB80T supplemented with 2 µM SiR-tubulin (#SC002, tebu-bio)). SiR-tubulin-lattice microtubules were immobilized on the coverslip surface and unbound microtubules were removed with BRB80T-S. Before the experiment, the solution was exchanged by AB3 (AB2 supplemented with 2 µM SiR-tubulin and lacking taxol). Finally, tau in AB3 was added to the measurement chamber at the final assay concentration stated in the main text.

For the data in Fig. 3d, taxol-lattice 405- and biotin-labeled microtubules were prepared as described above and kept in BRB80 supplement with 10 µM taxol. For each chamber, microtubules were diluted at least 100-fold into AB1 lacking taxol but including 1 µM SiR-tubulin (Cytoskeleton) and the mixture was allowed to bind to coverslips for 10 min. After this, the indicated amount of MAP protein in AB1 and 1 µM SiR-tubulin was flown into the chamber and MAPs were allowed to bind for 10 min before images were acquired.

1,6-hexanediol and envelope enrichment assays. For 1,6-hexanediol experiments, 0.5 nM GFP-MAP2c or GFP-MAP4 was flowed into the chamber and imaged after a 5-min incubation. Then a solution of 0.5 nM GFP-MAP2c or GFP-MAP4 in 10%-hexanediol in AB1 was introduced into the chamber and imaged after a 5-min incubation. For envelope enrichment assays, 0.5 nM GFP-tau and 0.5 nM mScarlet-tau was incubated in the chamber for 5 min, then a mixture of 0.5 nM mScarlet-tau and 0.5 nM sfGFP-tau, or sfGFP-MAP2c, or sfGFP-MAP4 was flowed into the chamber and allowed to incubate for 5 min. The mScarlet-tau envelopes were

used as fiducials for envelope boundaries. Background-subtracted mean intensities were obtained for a line scan along the microtubule. Each straight and uninterrupted (no microtubule overlaps) stretch of microtubule was counted as a single data point. Data points from two different protein preparations of mScarlet-tau envelopes were pooled. Fold enrichment was calculated by dividing each data point for envelope intensity by the average value of associated lattice intensity.

Optical tweezers. *Optical trapping assay.* Correlative force measurements and microscopy were performed on an optical tweezers setup equipped with confocal fluorescence imaging and microfluidic system (c-Trap, LUMICKS B.V.). The microfluidic system was passivated by BSA (#A0281, Sigma, 0.1% in PBS) and F127 (#P2443, Sigma, 1% in PBS) no later than 100 h before the experiment. The trap stiffness was calibrated using force calibration (0.5.1) in Bluelake (v.1.6.11, LUMICKS B.V.) under zero-flow condition. The experiments were performed at room temperature. Data was obtained using the Bluelake software (v.1.6.11) and analyzed using FIJI, Matlab (R2020b), and Jupyterlab (0.35.4). Forces were measured along the microtubule. Distances were measured between the beads from edge to edge (center-to-center measurement, subtracted by 1× the diameter of the bead).

Microtubule lattice compaction. Two streptavidin silica beads (1.12 µm, #SVSIP-10–5, Spherotech) were captured in two separate traps. The beads were moved to the microtubule channel with fluorescently labeled taxol-lattice microtubules in AB4 (AB2 supplemented with 30 µM taxol), where a microtubule was specifically attached to both beads. This construct was then moved to a channel containing AB4 where the beads were slowly moved apart until an increase in the force was detected. The microtubule was then kept in a straight but unstretched position and the flow was minimized (0.01–0.02 bar). The construct was moved into the channel containing 60 nM tau-mCherry in AB4 where the compaction of the microtubule was detected by the increase in force concomitant with a decrease in the distance between the two beads. In a control experiment, the construct was moved into a channel containing AB4 in the absence of tau. The distance between two beads was measured by averaging the distance before adding tau and averaging the distance when maximum compaction was achieved.

Envelope disassembly rate. A microtubule was suspended between two beads and moved to a channel containing 60 nM tau-mCherry in AB4. The microtubule was kept in the channel for at least 1 min to allow tau envelope formation, and moved the beads slowly apart until 40 pN force was measured (0 pN in the control experiment). The construct was then moved into the channel containing AB4 in absence of tau where the tau envelopes disassembled under a constant flow (0.1 bar). In the experiment where external force was applied, the force was kept constant by a feedback loop moving the beads further apart while the microtubule relaxed during tau envelopes disassembly. The envelopes were imaged using confocal microscopy and the envelope length was measured using ImageJ and divided by the time it took for the full envelope to disassemble.

Image analysis. Microscopy data were analyzed using ImageJ 2.3.0/1.53q (FIJI)[55]. The background was subtracted using the 'subtract background' function with a rolling ball radius of 50 and brightness and contrast settings were modified linearly. In images with substantial drift, the 'Descriptor-based series registration (2D/3D + T)' plugin was used in FIJI with interactive brightness and size detections in the microtubule channel to register the images.

Tau density estimation. Tau density on the microtubules was measured in FIJI by drawing a rectangle around the microtubule and measuring the RawIntDen. For background-subtraction the rectangle was then moved to an area directly adjacent to the microtubule where no microtubule is present and the RawIntDen was measured again and subtracted from the RawIntDen on the microtubule.

Hill coefficient analysis. The tau density (estimated as described above) on taxol-lattice microtubules was plotted against the tau concentration. The Hill coefficient was obtained by fitting this plot using Matlab curve fitting tool using the Hill equation and weights defined as 1/s.d.

Coverage rate analysis. Microtubules with different lattices were polymerized as described above. Twenty nanomolar tau diluted in imaging buffer AB2 (without taxol for GMPCPP- and GDP-lattice experiments) was added to the measurement chamber and the length of the tau envelopes was measured after 5 min of incubation time on the taxol- and GMPCPP-lattice microtubules. For GDP-lattice microtubules, the coverage rate was measured by taking the full length of the GDP-lattice and dividing it by the time when the entire lattice was covered by a tau envelope.

Kinesin run length and landing rate. Kinesin run lengths were measured manually by determining the beginning and the end of the run using kymographs compiled in FIJI ('KymographBuilder' plugin). Landing rates were determined by counting the number of traces within 30 s on various lengths of microtubules. Traces were considered when they visually resembled kinesin-1 landings (based on intensity and size).

Microtubule lattice compaction. Compaction of the microtubule lattice was measured using speckled microtubules (see above). MAPs were added at concentrations where microtubules would be partially covered with MAP envelopes. In the case of MAP4, 20 nM was added. Fluorescence images were taken with 5 s framerate and individual fluorescent speckles were tracked using FIESTA tracking software (v.1.6.0) to obtain the distance between two neighboring speckles. Compaction was measured by averaging the distance between two neighboring speckles before MAPs were added (average of 3–5 frames) and compared with the distance between the same speckles after 5 min of MAP incubation (average of 3–5 frames). Subsequently, fluorescence images of the MAPs were used to correlate the position of the speckles to the position of the envelopes on the microtubule lattice. The compaction was then averaged per microtubule for all events within tau envelopes, as well as outside tau envelopes. For MAP4, no assigning was required and all distances between speckles were pooled into the same category ('total') and the average was taken from all regions per microtubule.

Analysis of DDH and KIF1A motility. Kymographs of motor motility were analyzed manually to extract velocity and landing rate data. For velocity, entire visible runs were analyzed, including any pauses. For landing rates, the numbers of processive motors in each kymograph were counted manually. Processive runs were counted if the run was at least 3 pixels (~300 nm) long. For pixel-by-pixel intensity correlation between MAPs and motors, average intensity images were generated in each channel using FIJI and analyzed as described previously[16].

Cryo-EM characterization of microtubule lattice compaction. For cryo-EM experiments, 20 µM unlabeled porcine brain tubulin (Cytoskeleton #T240) was polymerized at 37 °C for 2 h in BRB80 (80 mM PIPES pH 6.8, 1 mM $MgCl_2$, 1 mM EGTA) supplemented with 3 mM GTP. An equal volume of BRB80 supplemented with 10 µM taxol was added, and the polymerized microtubules were left at room temperature overnight. Directly before grid preparation, the microtubules were pelleted at 20,000 r.c.f. for 10 min and resuspended to 3 µM in fresh BRB80.

Microtubules and MAPs were pre-incubated before being added to electron microscopy grids. A mixture of 3 µl 3 µM microtubules and 8 µl MAP was incubated at room temperature for 20 min. For the microtubule-only dataset, the MAP was replaced with BRB80. Final MAP concentrations were 27 µM tau, 28 µM MAP2c, and 34 µM MAP4. During incubation, R1.2/1.3 Au300 Quantifoil EM grids were glow-discharged for 40 s. Then, 4 µ microtubule–MAP mixture was applied to the grid in a Vitrobot Mark II (TFS) set to 100% humidity and 22 °C. After 30 s, the grid was blotted for 4.5 s and plunged into liquid ethane. The grids were loaded into a Polara cryo-electron microscope (TFS) operating at 300 kV. Images were collected semi-automatically in SerialEM with a pixel size of 1.35 Å px^{-1}, defocus ranging from −2 to −3 µm, and a dose rate of 25e^{-1} px^{-1} s^{-1} for a 1.5-s exposure. Roughly forty images were taken for each dataset. Movie stacks were aligned in MotionCorr2[56]. Straight and uninterrupted microtubule segments longer than 2.5 µm were then manually picked in RELION 3.0[57], with the coordinates used to crop out each microtubule. In FIJI[55], each microtubule segment was then rotated to line up with the *y*-axis of the image and the Fast Fourier Transform (FFT) was calculated. The spatial frequency of the peak in intensity of the 4 nm (J_s) reflection[58], corresponding to the longitudinal lattice spacing, was measured manually in FIJI.

Live-cell experiments. *Molecular cloning.* The sequence of eGFP-tau was subcloned from the vector pSP6 EGFP-tau to the pcDNA4.0/TO mammalian expression vector using BamHI and AscI restriction enzymes. The sequence of the resulting pcDNA4.0/TO_EGFP-tau plasmid was checked using Sanger sequencing. The sequence coding *MAP4* gene was amplified from cDNA generated from the U-2 OS cell line. The amplified fragment was then cloned into the pEGFP-C1 mammalian expression vector using the restriction enzymes HindIII and XbaI. We confirmed that the sequence of the amplified gene corresponds to the RefSeq NM_002375.5 with Sanger sequencing. The resulting plasmid was named pEGFP-C1_MAP4.

Cell culture and preparation for live-cell experiments. U-2 OS cells (ATCC, HTB-96) were maintained in DMEM + GlutaMAX (Sigma-Aldrich, 61965-026) supplemented with 10% FBS at 37 °C in 5% CO_2. Two days before imaging, the cells were plated onto 4-chamber Glass Bottom Dish (Cellvis, D35C4-20-1.5-N) to achieve 30% confluency. On the following day, the cells were transfected with the mammalian expression vector pcDNA4.0/TO_EGFP-tau or pEGFP-C1_MAP4, or co-transfected with the pcDNA4.0/TO_EGFP-tau and pmScarlet-i alphaTubulin-C1 expression vectors using the HP-Xtreme transfection reagent (Sigma-Aldrich, 636624400). The pmScarlet-i_alphaTubulin_C1 was a gift from D. Gadella (Addgene plasmid #85047; http://n2t.net/addgene:85047; RRID:Addgene_85047). The cells were imaged 24 h after transfection, with DMEM medium exchanged for FluoroBright DMEM medium (Sigma-Aldrich, A1896701).

Live-cell imaging. Using TIRF microscopy, cells were imaged for 1 min before addition of taxol or DMSO, with frame interval 700 ms, or 1,400 ms for dual imaging experiments. Then imaging was paused, and taxol or DMSO was added to the medium. The final concentration of taxol was 0.01 µM. Cells were recorded for an additional 10 min immediately after the addition of taxol or DMSO.

Immunofluorescence. After taxol treatment, the recorded cells were fixed directly in a glass bottom dish using 3% paraformaldehyde in MSB buffer. The cells were then permeabilized with 0.1% Triton Tx-100 and subsequently stained with DM1A antibody against α-tubulin (1:500 dilution, #T9026, Sigma). Cells were then kept in the MSB buffer and imaged with the TIRF microscope.

Image analysis. All images and movies were processed in FIJI. The two movies resulting from one recording (one movie before and one movie after the addition of taxol or DMSO) were merged. The shift resulting from manipulating the sample was corrected with the plugin Template_Matching and function Align_slices in stacks. The kymograph was generated with the KymographBuilder plugin.

Coefficient of variation. Using FIJI, a box was drawn inside the cell, covering (most of) the area of the cell. The coefficient of variation was determined from the standard deviation of the tau or MAP4 fluorescent signal within the box divided by the mean, before and 10 min after taxol or DMSO treatment. The coefficient of variation 10 min after treatment was then normalized to the coefficient of variation before treatment.

Envelope fission frequency and disassembly rate. The fission frequency and disassembly rate of envelopes on microtubules in eGFP-tau cells were measured using FIJI. Fissions were manually counted and divided by the length of the microtubule at the time the first fission appeared until all tau envelopes had disassembled from the microtubule lattice. The length of the microtubule or envelope were obtained by the eGFP-tau signal.

Statistics and reproducibility. For representative figures, whenever not specifically stated in the caption, all data was collected from at least two independent trials. All repeated independent experiments showed similar results and no data was excluded from the manuscript. Unless otherwise stated, all data were analyzed manually using ImageJ (FIJI) or Matlab (R2020b). Graphs were created using GraphPad Prism v.8.0.1 or Matlab R2020b and statistical analyses were performed using the same software. Major points on graphs represent data means and the error bars represent variation or associated estimates of uncertainty.

Reporting summary. Further information on research design is available in the Nature Research Reporting Summary linked to this article.

Data availability

Source data files for all figures and Supplementary figures, are available with this manuscript. Source data are provided with this paper.

References

52. Gell, C. et al. Purification of tubulin from porcine brain. *Methods Mol. Biol.* **777**, 15–28 (2011).
53. Tan, R., Foster, P. J., Needleman, D. J. & McKenney, R. J. Cooperative accumulation of dynein–dynactin at microtubule minus-ends drives microtubule network reorganization. *Dev. Cell* **44**, 233–247 (2018).
54. McKenney, R. J., Huynh, W., Tanenbaum, M. E., Bhabha, G. & Vale, R. D. Activation of cytoplasmic dynein motility by dynactin-cargo adapter complexes. *Science* **345**, 337–341 (2014).
55. Schindelin, J. et al. Fiji: an open-source platform for biological-image analysis. *Nat. Methods* **9**, 676–682 (2012).
56. Zheng, S. Q. et al. MotionCor2: anisotropic correction of beam-induced motion for improved cryo-electron microscopy. *Nat. Methods* **14**, 331–332 (2017).
57. Zivanov, J. et al. New tools for automated high-resolution cryo-EM structure determination in RELION-3. *eLife* **7**, e42166 (2018).
58. Chrétien, D., Kenney, J. M., Fuller, S. D. & Wade, R. H. Determination of microtubule polarity by cryo-electron microscopy. *Structure* **4**, 1031–1040 (1996).

Acknowledgements

The authors thank members of the MOM lab for feedback and discussion during the project and the Protein Facility of MPI-CBG and V. Váňová for technical support. We also thank A. Carter for critical reading of the manuscript, O. Kučera for establishing the optical tweezers assay and J. Sabó for support in obtaining imaging data. This work was supported by Czech Science Foundation grant 19–27477X to Z.L. and L.L. and grant 20-04068S to M.B. We acknowledge the financial support from the Charles University Grant Agency (GAUK no. 373821 to V.S.) and the project 'Grant Schemes at CU' (reg. no. CZ.02.2.69/0.0/0.0/19_073/0016935) to T.H. and V.S., grants 1R35GM124889 to R.J.M. and 1R35GM133688 to K.M.O.M. K.M.O.M. is also supported by the Pew Charitable Trusts grant A19-0406. We acknowledge the institutional support from the CAS (RVO: 86652036), CMS supported by MEYS CR (LM2015043), and the Imaging Methods Core Facility at BIOCEV, an institution supported by the MEYS CR (Large RI Project LM2018129 Czech-BioImaging) and ERDF (project no. CZ.02.1.01/0.0/0.0/16_013/0001775) for their support in obtaining imaging data presented in this paper.

Author contributions

The manuscript was conceptualized by R.T., K.M.O.M., R.J.M., M.B., and Z.L.; methods were developed by V.S., T.H., L.L., S.E.L., R.J.M., M.B., and Z.L.; recombinant proteins were generated by V.S., R.T., T.T., and M.D.; TIRF experiments were performed by V.S., R.T., and R.J.M.; optical tweezers experiments by V.S.; cryo-EM experiments by S.E.L.; live-cell experiments by T.H.; data were formally analyzed by V.S., R.T., T.H., S.E.L., K.M.O.M., and R.J.M.; the manuscript was written by V.S., L.L., K.M.O.M., R.J.M., M.B., Z.L., with reviewing and editing by T.T. and M.D.; the project was supervised by K.M.O.M., R.J.M., M.B., and Z.L.; funding was acquired by V.S., T.H., L.L., K.M.O.M., R.J.M., M.B., and Z.L.

Competing interests

The authors declare no competing interests.

Additional information

Supplementary information The online version contains supplementary material available at https://doi.org/10.1038/s41589-022-01096-2.

Correspondence and requests for materials should be addressed to Kassandra M. Ori-McKenney, Richard J. McKenney, Marcus Braun or Zdenek Lansky.

Peer review information *Nature Chemical Biology* thanks Arne Gennerich and the other, anonymous, reviewer(s) for their contribution to the peer review of this work.

A.3 TAU PHOSPHORYLATION IMPEDES FUNCTIONALITY OF PROTECTIVE TAU ENVELOPES

Siahaan V.*, Weissova, R.*, Lanska, E., Karhanova, A., Dostal, V., Henriot, V., Janke, C., Libusova, L., Braun, M., Balastik,M., Lansky, Z. (in submission at Nature Chemical Biology)

*These authors contributed equally.

Contributions as stated in the article:

The manuscript was conceptualized by M.Br., M.Ba., Z.L.; methods were developed by V.S., R.W., E. L., A.K., V.D.; TIRF in vitro experiments were performed by V.S., E. L., A.K.; tau lysate preparation and experiments were performed by R.W., E.L.; live-cell experiments were performed by R.W., V.D.; FRAP experiments were performed by V.S., R.W.; data were analyzed by V.S., R.W., E.L., A.K., V.D.; resources were provided by V.H., C.J.; the manuscript was written by V.S., M.Br., Z.L., with reviewing and editing by R.W., M.Ba.; visualization was done by V.S.; the project was supervised by L.L., M.Br., M.Ba., Z.L.; funding was acquired by V.S., R.W., V.D., L.L., M.Br., M.Ba., and Z.L.

In detail: For all in vitro TIRF experiments, development of the methods and optimization of the analysis of the data for figures 1, 2 and 4a-c was done by V.S. with help from E.L., A.K., M.Br. and Z.L. All in vitro TIRF experiments and its repetitions for figure S1h, and some of the repetitions for figure 4a-c and S4a,b,c were performed by V.S. Sample preparation and data analysis of the Mass Spectrometry results (figures 1a,b, S1a,b,d-g, 2a,b and S2a,b) were optimized and performed by V.S. using Excel and Matlab. All FRAP experiments (figure 3a-c, S3g-i) were optimized by V.S. and R.W., all repetitions were performed by V.S. using spinning disk. The manuscript was written by V.S., M.Br., and Z.L. Visualization of all figures was done by V.S. using Matlab and Illustrator. Additionally, funding was acquired by V.S. from the Charles University Grant Schemes: GAUK no. 373821, and START reg. no. CZ.02.2.69/0.0/0.0/19_073/0016935.

Tau phosphorylation impedes functionality of protective tau envelopes

Valerie Siahaan*[1,2], Romana Weissova*[2,3], Eva Lanska[1,2], Adela Karhanova[1], Vojtech Dostal[2], Veronique Henriot[4,5], Carsten Janke[4,5], Lenka Libusova[2], Marcus Braun[#1], Martin Balastik[#3], Zdenek Lansky[#1]

1. Institute of Biotechnology, Czech Academy of Sciences, BIOCEV, Prague-West, Czech Republic
2. Department of Cell Biology, Faculty of Science, Charles University, Prague, Czech Republic
3. Institute of Physiology, Czech Academy of Sciences, Prague, Czech Republic
4. Institut Curie, Université PSL, CNRS UMR3348, Orsay, France
5. Université Paris-Saclay, CNRS UMR3348, Orsay, France

*,#Contributed equally
Correspondence: marcus.braun@ibt.cas.cz, martin.balastik@fgu.cas.cz, zdenek.lansky@ibt.cas.cz

Abstract

Tau, an axonal microtubule-associated protein, is a critical regulator of microtubule function and stability. Tau interaction with microtubules is regulated by tau phosphorylation. Tau hyperphosphorylation is implicated in microtubule destabilization related to neurodegenerative disorders. How tau phosphorylation leads to microtubule destabilization is however unknown. Recently, it was shown that tau molecules on microtubules cooperatively assemble into cohesive layers termed envelopes. Tau envelopes protect microtubules against degradation by microtubule-severing enzymes, suggesting a functional link between envelopes and microtubule stability. Here we show that tau phosphorylation has deleterious effects on the microtubule-protective function of tau envelopes. Using reconstitution and live-cell experiments, we found that tau phosphorylation destabilizes tau envelopes and decreases their integrity, leading to reduced microtubule protection against microtubule-severing enzymes. Our data suggest that a perturbation of microtubule homeostasis linked to tau hyperphosphorylation in neurodegeneration, could be explained by the disassembly and impaired functionality of the tau envelopes.

Introduction

Microtubules are rigid filaments, which are essential for neuronal function and homeostasis e.g. by providing tracks for intracellular cargo transport. Microtubules are dynamic polymers, frequently switching between phases of assembly and disassembly[1]. The lifetime of a microtubule is regulated by a multitude of microtubule-associated proteins, which either affect microtubule assembly and disassembly[2,3], or can sever microtubules into fragments[4]. Deregulation of various microtubule-associated proteins, e.g. tau, has been shown to trigger changes in microtubule dynamics, induce loss of microtubule mass from axons and dendrites, and is associated with multiple neurodegenerative disorders[2,5].

Tau is an intrinsically disordered microtubule-associated protein, which in healthy neurons localizes predominantly to axonal microtubules. Tau regulates the functioning of other microtubule-associated proteins and protects microtubules against microtubule-severing enzymes, such as katanin[6]. During neurodegeneration, tau is found aggregated in neurofibrillary tangles, which is one of the hallmarks of neurodegenerative disorders collectively termed tauopathies, such as Alzheimer's disease[7,8]. It was proposed that tau aggregation causes a depletion of functional tau[9,10], thereby leaving the axonal microtubules unprotected against microtubule-severing enzymes, such as katanin, which could lead to pathological microtubule destabilization. Moreover, aggregated tau has an increased phosphorylation state as compared to physiological tau, and has been shown to have reduced interaction with microtubules[11,12]. These findings suggest a relation between hyperphosphorylation of tau and microtubule instability related to neurodegeneration, nevertheless, the underlying molecular mechanism remains unclear.

It has recently been shown that tau molecules associate with microtubules in two distinct modes – either (i) diffusing individually along the microtubule lattice, rapidly binding and unbinding, or (ii) binding cooperatively, with much longer interaction times, constituting cohesive envelopes, previously referred to as 'condensates' or 'islands'[13–15]. These envelopes enclose the microtubules and act as selectively permeable barriers for other microtubule-associated proteins[13,14]. Tau envelopes can differentially modulate the action of microtubule-related molecular motors, e.g. decreasing the kinesin-1 walking distance[14,16], while permitting dynein-mediated transport[13]. While microtubules covered by individually diffusing tau

molecules are prone to disintegration by microtubule severing enzymes, such as katanin[14], tau envelopes efficiently protect the microtubule surface from the action of microtubule severing enzymes[13,14]. These observations suggest that the protective function of tau is mediated by the cohesion of tau envelopes. We thus hypothesized that pathological effects of tau phosphorylation can be explained by the impact of tau phosphorylation on the formation and function of protective tau envelopes.

Here, we demonstrate that the formation and maintenance of tau envelopes is indeed critically regulated by phosphorylation. We found that phosphorylation of tau decreases the propensity of tau to form envelopes and that envelopes formed by phosphorylated tau have altered functionality with decreased protection against microtubule severing enzymes. Our findings suggest that the cohesive binding mode of tau may provide a causal connection between tau phosphorylation and impaired tau functionality: the reduction of tau envelopes and their impaired functionality, caused by tau phosphorylation, results in decreased shielding of microtubules from severing enzymes, and consequently in a decrease of microtubule stability.

Results

Tau phosphorylation induces envelope disassembly

To investigate whether phosphorylation of tau affects the formation of tau envelopes, we expressed GFP-labelled human 2N4R tau (full length tau protein, 441 amino acids), in insect cells and used Alkaline phosphatase to dephosphorylate the tau in vitro (Methods). This approach yielded two tau samples: phosphorylated tau (native, insect cell expressed tau, denoted as 'phospho-tau'), and dephosphorylated tau (phosphatase treated, insect cell expressed tau, denoted as 'dephospho-tau') (Fig. 1a). To confirm the efficiency of the phosphatase-treatment, we determined the degree of phosphorylation of these samples at all potential phosphorylation sites using mass spectrometry (Methods, Fig. 1b, for individual sites see Supplementary Fig. 1a,b). We then added the phospho-tau or dephospho-tau samples at 1.5 nM to surface-immobilized taxol-stabilized microtubules and visualized the interaction using TIRF microscopy. While dephospho-tau readily formed micrometer-sized envelopes at this concentration, by contrast, phospho-tau was present on microtubules only

diffusively and did not form envelopes (Fig. 1c, Supplementary Movie 1,2). Repeating this experiment at two higher concentrations of tau, we found that tau envelopes were formed by both tau samples (Supplementary Fig. 1c), nevertheless, at all concentrations tested, dephospho-tau covered a higher percentage of the microtubules compared to phospho-tau (Fig. 1d), demonstrating higher propensity of dephosphorylated tau to form envelopes. To confirm our findings, we repeated these experiments with tau expressed in bacterial cells which possesses a low phosphorylation state (denoted by Bact-tau) and used a kinase to increase its phosphorylation state (Supplementary Fig. 1d, Methods). Multitude of kinases have been shown to phosphorylate tau, including proline-directed kinases (e.g. Cdk5, GSK-3β or MAP kinases). Cdk5-mediated phosphorylation of tau has been shown in healthy conditions to control multiple processes in neural development (e.g. axonal growth and guidance), while hyperactivation of Cdk5 (e.g. in Alzheimer's disease) has been shown to result in heightened tau phosphorylation, promoting tau mislocalization, aggregation and formation of neurofibrillary tangles[9,17,18]. Therefore, we phosphorylated the Bact-tau sample using Cdk5 kinase with its activator p35 (denoted by Bact-Cdk5-tau, Supplementary Fig. 1d, Methods) yielding a sample with higher phosphorylation degree as confirmed by mass spectrometry (Supplementary Fig. 1e, for individual sites see Supplementary Fig. 1f,g). We then added these samples separately to surface-immobilized taxol-stabilized microtubules and studied the envelope coverage after 3 minutes of incubation. In accordance with our previous results, we found that the Bact-tau formed envelopes at much lower concentrations compared to Bact-Cdk5-tau (Supplementary Fig. 1h). We next asked if tau phosphorylation can destabilize preexisting tau envelopes formed by dephosphorylated tau. To test this, we formed envelopes using 15 nM Bact-tau and after 10 minutes we added active Cdk5 kinase to the channel while keeping tau in solution. After the addition of active kinase we observed that the tau envelopes started to disassemble from their boundaries (Fig. 1e, Supplementary movie 3, Methods) with occasional fission events within the boundaries of the envelope during disassembly (0.01 ± 0.08 fissions $mm^{-1}s^{-1}$). In a control experiment, we added deactivated Cdk5 (Methods) to the envelopes while keeping tau in solution, in which case no disassembly was observed and, on the contrary, a significant increase of the envelope coverage was detected (Fig. 1e,f, Supplementary movie 4). Combined, these experiments show that phosphorylation of tau decreases the propensity of tau to form envelopes and destabilizes preexisting envelopes.

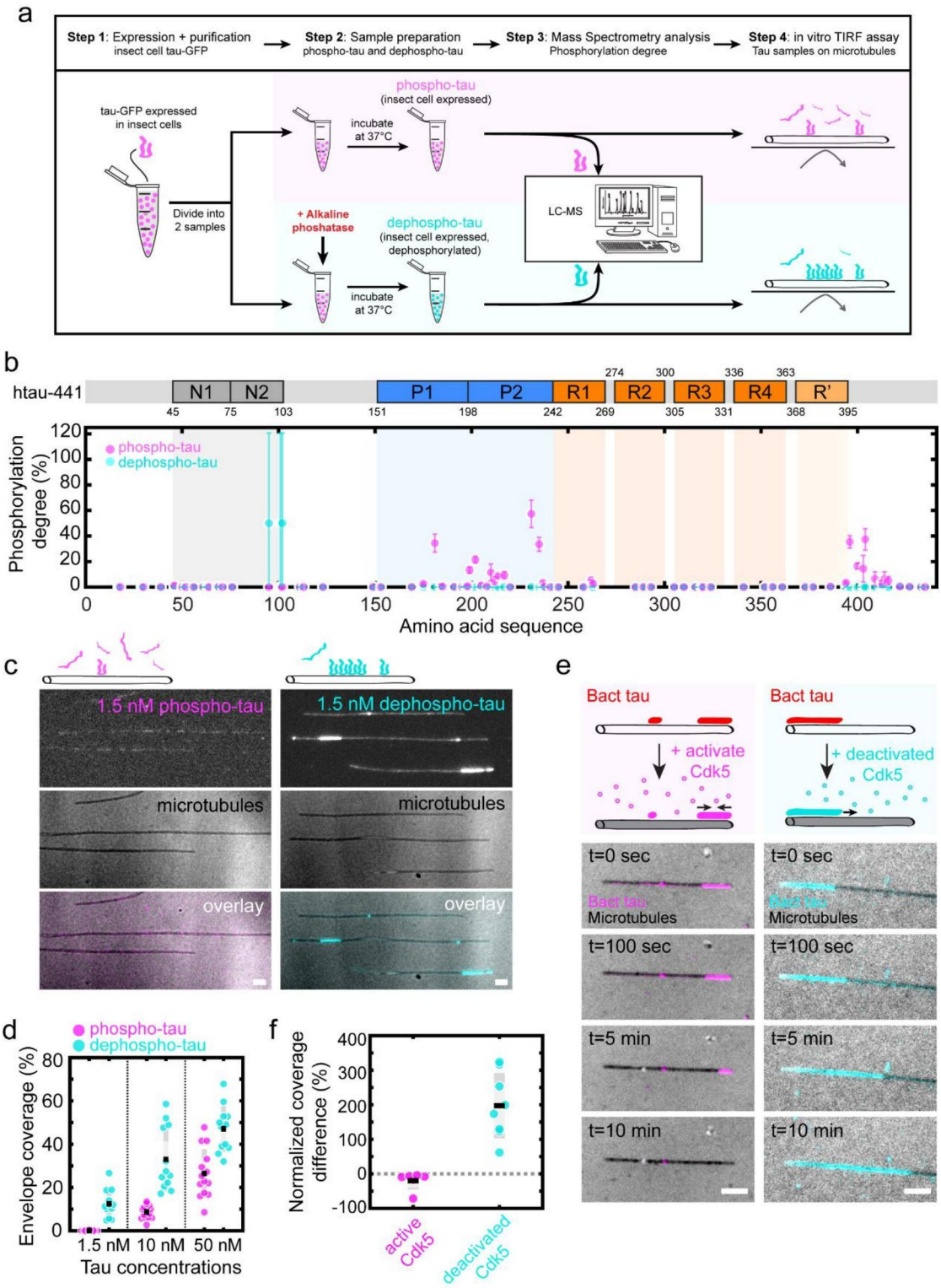

Fig. 1. Tau phosphorylation induces envelope disassembly. a. Schematics of the sample preparation. **b**. Mass-spectrometry-determined degree of phosphorylation of phospho-tau (insect cell expressed tau, magenta) and dephospho-tau (phosphatase-treated insect cell expressed tau, cyan). Phosphorylation degree is presented as the mean ± s.d. (Methods) and displayed at the location of the phosphorylation site along the amino acid sequence of tau (schematic of the sequence is shown above the plot). The domains on the tau sequence are

color-coded: N-terminal domains (N1, N2, grey), proline-rich domains (P1, P2, blue), microtubule-binding repeats (R1-R4, orange), and the domain pseudo-repeat (R', light orange). **c**. Multichannel fluorescence micrographs of 1.5 nM phospho-tau (magenta, left), and 1.5 nM dephospho-tau (cyan, right) on taxol-stabilized microtubules (black, middle panels) after 3 min incubation. Scale bars: 2 µm. **d**. Percentage of taxol-stabilized microtubules covered with tau envelopes after 3 min of tau incubation on surface-immobilized microtubules. Envelope coverage for phospho-tau (magenta) at 1.5 nM was 0.1 ± 0.1%, at 10 nM was 8.6 ± 3.1%, and at 50 nM was 26.5 ± 11.2% (mean ± s.d., n=14, 14, 14 fields of view in 11 independent experiments). Envelope coverage for dephospho-tau (cyan) at 1.5 nM was 12.5 ± 6.4%, at 10 nM was 32.9 ± 14.7%, and at 50 nM was 47.1 ± 10.5%, n=12, 12, 12 independent experiments). **e**. Multichannel fluorescence micrographs of 15 nM Bact-tau (red in schematics) after treatment with active Cdk5 (left, Bact-tau in magenta) or with deactivated Cdk5 (right, Bact-tau in cyan). Microtubules (black) imaged using IRM. Scale bars: 2µm. **f.** Normalized difference between the coverage before and after treatment with active Cdk5 or deactivated Cdk5. Normalized coverage difference for active Cdk5: -19.4 ± 25.9% (mean ± s.d., n=6 independent experiments); deactivated Cdk5: 197.6 ± 94.3% (n=8 independent experiments). Two-sided t-test: $p=1.52*10^{-4}$.

Phosphorylation reduces envelope integrity

We next asked why tau phosphorylation leads to a decrease in envelope formation. We hypothesized that phosphorylated tau might not be able to participate in the formation of tau envelopes. Our phosphorylated tau samples are heterogeneous, meaning that they consist of tau molecules with different patterns and degrees of phosphorylation, which could be differently competent in forming envelopes. To test which tau molecules, out of a given sample, can participate in envelope formation, we added phospho-tau at high concentration (1 µM) to microtubules in solution, ensuring that microtubules were fully covered by tau envelopes. By spinning down the microtubules, we then separated the sample into (i) tau, which participated in envelope formation (tau in envelopes – characterized by limited translocation along the microtubule lattice and with very low turnover[13,14] - found in the pellet along with the microtubules) and (ii) tau, which did not participate in envelope formation (tau in solution – unbound tau or tau characterized by rapid diffusion along the microtubule lattice and high turnover[13,14] - found in the supernatant) (Fig. 2a, Methods). When we then analyzed the phosphorylation degree of these two samples by mass spectrometry, we did not find any striking differences in the phosphorylation patterns between the two samples (Fig. 2b, for individual sites see Supplementary Fig. 2a,b), demonstrating that phosphorylated tau is competent in envelope formation. We did,

nevertheless, find that the phosphorylation degree of tau in the supernatant (not participating in envelope formation) was slightly elevated compared to tau in the envelopes. While we observed almost no phosphorylation in the N-terminal region as well as the microtubule-binding repeats for both tau samples, we found on average about a 5% increase in phosphorylation degree within the proline-rich region and C-terminal regions in tau found in solution. This data demonstrates that although phosphorylation of tau decreases its propensity to form envelopes, phosphorylated tau can (particularly at higher concentration) be incorporated into the tau envelopes.

Knowing that phosphorylated tau participates in envelope formation, we hypothesized that the lowered propensity to form envelopes is caused by a combination of (i) a reduced interaction of phosphorylated tau with the microtubule lattice, as observed previously[11,12,19–21], and (ii) reduced cohesiveness of the envelope, presumably due to reduced tau-tau interaction between phosphorylated tau molecules. To demonstrate (i) the reduction of the affinity of phosphorylated tau molecules on microtubules, we investigated the density of tau on the surface of microtubules. We performed the tau-microtubule interaction experiment at two different conditions; on GMPCPP-microtubules (which prevent the envelope formation) and on native GDP-microtubules (where tau binds preferentially in the envelope form[15]) (Methods, Supplementary Fig. 2c,d,e). Consistent with previous findings[11,12,19–21], at most conditions, except for the saturating conditions on GDP-lattices, we found that phospho-tau is present on the microtubule lattice at lower densities compared to dephospho-tau (Supplementary Fig. 2c,d,e), confirming that phosphorylation reduces tau-microtubule interaction. To test if, furthermore, phosphorylation of tau, (ii) influences the cohesiveness of the envelopes, we mixed 8 nM mCherry-labeled phospho-tau with 8 nM GFP-labeled dephosho-tau, added this mixture to surface immobilized microtubules and observed the formation of envelopes. In line with the results of our pelleting assay, we observed that these envelopes exhibited both GFP and mCherry fluorescence (Fig. 2c), demonstrating that phosphorylated tau molecules are competent to participate in envelope formation. We then analyzed the ratio of phospho-tau to dephospho-tau outside of the envelope region and compared it to the ratio within the envelopes. This analysis revealed a significant relative decrease of phospho-tau within the tau envelopes compared to the regions outside the envelopes (Fig. 2d), showing that, additional to lower affinity to the microtubule lattice,

phosphorylated tau less readily participates in envelope formation. Next, we prepared tau envelopes of either phospho- or dephospho-tau and studied the density of tau molecules within the enveloped regions. We found that for any given envelope coverage, the density of tau within the envelope region is lower in envelopes prepared from phospho-tau compared to envelopes prepared from dephospho-tau (Fig. 2e). This data suggests that envelopes formed by phosphorylated tau consist of a less dense and potentially more gap-prone structure. To test this hypothesis, we prepared tau envelopes on surface-immobilized microtubules using 10 nM Bact-tau, that has a low phosphorylation degree, and removed tau from solution to observe the disassembly of the envelopes. The removal of tau from solution was either performed in presence of (i) active Cdk5 kinase, (ii) deactivated Cdk5 kinase, or (iii) in the absence of a kinase (control) (Methods). In presence of active Cdk5, we observed that the disassembly of the envelopes was significantly faster compared to the conditions with deactivated Cdk5 or the control (Fig. 2f,g(note the different experimental timeframes), Supplementary Movie 5,6). These findings indicate that the Cdk5 kinase actively phosphorylated the tau in the envelopes, causing envelope destabilization. Interestingly, we observed a striking increase in the number of fission events within the envelopes in the presence of active Cdk5, compared to the deactivated Cdk5 or control envelopes (Fig. 2g,h). Combined, these data suggest that tau phosphorylation compromises the integrity and cohesiveness of the tau envelopes.

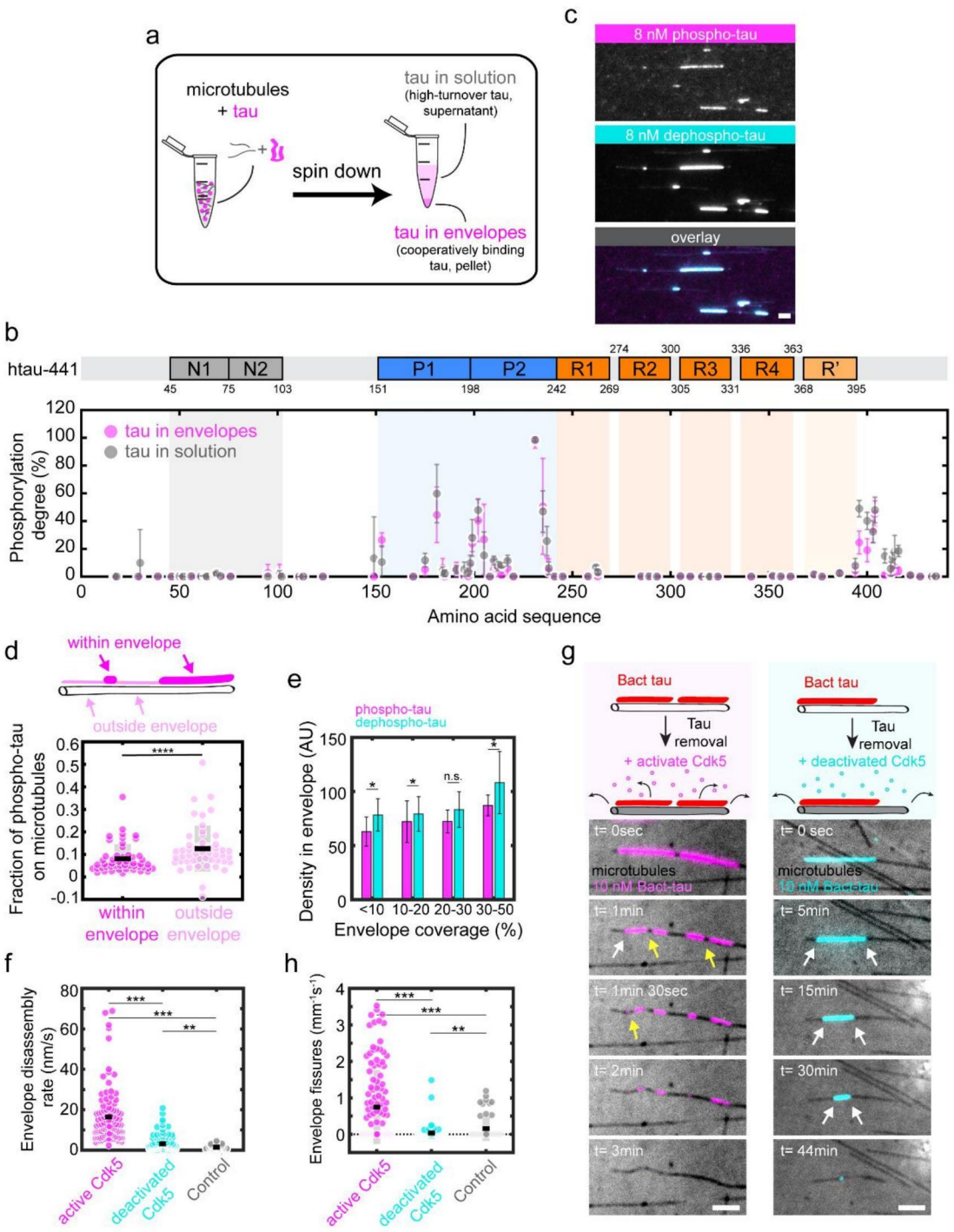

Fig. 2. Phosphorylation reduces envelope integrity. a. Schematics of the sample preparation (Methods). **b**. Mass-spectrometry-determined degree of phosphorylation of cooperatively bound tau found in the pellet (slow-turnover tau in envelopes, magenta) and unbound tau found in the supernatant (high-turnover tau in solution, grey). The phosphorylation degree was presented as the mean ± s.d. for each sample (Methods) and displayed at the location of the phosphorylation site along the amino acid sequence of tau (schematic of the sequence is shown above the plot). The domains on the tau sequence are color-coded: N-terminal domains (N1, N2, grey), proline-rich domains (P1, P2, blue), microtubule-binding repeats (R1-

R4, orange), and the domain pseudo-repeat (R', light orange). **c**. Multichannel fluorescence micrographs of 8 nM phospho-tau (magenta, top panel) and 8 nM dephospho-tau (cyan, middle panel) incubated simultaneously (overlay, bottom panel) and imaged after 3 min incubation. Scale bar: 2 µm. **d.** Fraction of the density of phospho-tau compared to the total density of all tau within tau envelope region (magenta), or outside of tau envelope region (light pink). Location of the envelope and non-envelope region are schematically drawn in the cartoon above the plot. Fraction of phospho-tau within the envelope was 0.08 ± 0.06 (mean ± s.d., n=50 envelopes in 10 independent experiments), and outside the envelope 0.12 ± 0.10 (n=50 regions in 10 independent experiments). Two-sided t-test, $p=6.63*10^{-4}$. **e.** Density of tau within the envelope region for phospho-tau (magenta) and dephosho-tau (cyan) envelopes. Tau density in phospho-tau envelopes: 63.0 ± 13.5 (0 – 10% coverage), 72.1 ± 19.4 (10-20%), 72.4 ± 10.7 (20-30%), and 87.2 ± 95.6 (30-50%) (mean ± s.d., n=18, 16, 18, 12 envelopes in 5, 3, 4, 1 independent experiments); in dephospho-tau envelopes: 78.3 ± 15.0 5 (0 – 10% coverage), 79.3 ± 16.0 (10-20%), 83.3 ± 16.5 (20-30%), 108.2 ± 28.8 (30-50%) (n=7, 17, 30, 37 envelopes in 2, 2, 4, 5 independent experiments. Two-sided t-test between tau samples (left to right): p=0.0207, p=0.2569, p=0.0165, p=0.0169. **f.** Envelope disassembly rate after addition of active Cdk5 (magenta), deactivated Cdk5 (cyan), or in absence of Cdk5 (control, grey). Envelope disassembly rate for active Cdk5: 16.4 ± 13.7 nm/s (mean ± s.d., n=99 envelopes in 7 independent experiments); for deactivated Cdk5 3.2 ± 3.8 nm/s (n=123 envelopes in 8 independent experiments); for control 1.5 ± 1.1 nm/s (n=38 envelopes in 4 independent experiments). Two-sided t-test (left to right): $p=2.30*10^{-20}$, $p=5.92*10^{-10}$, p=0.0075. **g.** Fluorescence micrographs of removal of 10 nM Bact-tau in presence of active Cdk5 (left panels, Bact-tau in magenta) or deactivated Cdk5 (right panels, Bact-tau in cyan). Microtubules (black) are visualized using IRM. Envelope disassembly from the boundaries is indicated by the white arrows while fission events within the boundaries of the envelopes are indicated by yellow arrows (only observable in the active Cdk5 example). Note the different timepoints and intervals for the two samples. Scale bars: 2 µm. **h.** Number of fission events within the boundaries of Bact-tau envelopes during disassembly in presence of Cdk5 (magenta), deactivated Cdk5 (cyan), or in absence of kinase (control, grey). Number of envelope fissures in presence of active Cdk5: 0.75 ± 1.02 $mm^{-1}s^{-1}$ (mean ± s.d., n=117 envelopes in 7 independent experiments); deactivated Cdk5: 0.03 ± 0.17 $mm^{-1}s^{-1}$ (n=119 envelopes in 8 independent experiments); in absence of kinase (control): 0.16 ± 0.34 $mm^{-1}s^{-1}$ (n=52 envelopes in 4 independent experiments). Two-sided t-test (left to right): $p=8.85*10^{-13}$, $p=7.39*10^{-5}$, p=0.001364.

Tau phosphorylation affects envelope formation in cells

We next investigated how envelope formation is regulated by tau phosphorylation in a cellular environment. Initially, we performed TIRF assays with cell lysates (Supplementary Fig. 3a, Methods). To generate tau lysates, we either overexpressed GFP-tau in HEK cells (denoted as HEK lysate), or we overexpressed GFP-tau together with proline-directed kinase Cdk5 and its activator p25 (Cdk5/p25) in HEK cells (denoted as Cdk5 lysate). We then lysed the cells,

added the lysates to surface-immobilized microtubules, and followed the tau-microtubule interaction using TIRF microscopy (Supplementary Fig. 3a,b). While we observed tau envelopes forming in the HEK lysate, there were no envelopes forming in the Cdk5 lysate (Supplementary Fig. 3b,c). These observations are in line with our in vitro experiments showing that phosphorylation of tau decreases the propensity of tau to form envelopes. Next, we overexpressed GFP-tau and mScarlet-tubulin in U-2 OS cells and followed the tau signal correlated to the microtubule signal throughout the cell cycle, which is tightly regulated by activation of specific proline-directed cyclin-dependent kinases known to phosphorylate tau[22]. When following the tau signal throughout the cell cycle, we observed high tau signal on microtubules in interphase cells, where the overall activity of kinases is low, and a significant reduction of the tau signal on microtubules in mitotic cells (Supplementary Fig. 3d,e,f), where multiple mitotic kinases are active[23]. This observation is in agreement with our in vitro findings and published data of decreased affinity of phosphorylated tau for microtubules[11,12].

To discern details of the tau-microtubule interaction in living cells and its regulation by phosphorylation, we overexpressed GFP-tau together with Cdk5/p25 in IMCD-3 cells, denoted as tau-Cdk5. In a control experiment, we overexpressed GFP-tau in IMCD-3 cells in the absence of Cdk5/p25, denoted as tau. Additionally, we overexpressed N-terminally truncated GFP-tau that is not able to form tau envelopes[13,14], denoted as tau-ΔN (Methods). At elevated (micromolar) tau concentrations, tau envelopes are not readily discernable by a local increase in tau density[15]. We thus did not expect to observe regions of high and low tau density in cells, since tau is present at micromolar concentrations in cells[24,25]. Indeed, in both tau and tau-ΔN overexpressing cells, as well as in the tau-Cdk5 cells, tau covered microtubules uniformly along their entire lengths (Supplementary Fig. 3g). In tau-ΔN and tau-Cdk5 cells, tau signal on the microtubule was however weaker (Supplementary Fig. 3h), although the expression levels were comparable (Supplementary Fig. 3i), suggesting that in tau-ΔN and tau-Cdk5 cells, tau has a lower affinity for the microtubule surface or is bound at lower density because of reduced cohesiveness between the tau molecules.

To assess the turnover of tau on microtubules in our differently transfected cells, we used fluorescence recovery after photobleaching (FRAP). We photobleached a circular region of the cell that contained microtubules covered by tau, and studied the recovery of the tau signal

on the microtubules over time (Fig. 3a, Supplementary Fig. 3j, Supplementary Movie 7-9). We found that the recovery of the fluorescent tau signal was slowest and the immobile fraction highest in our control cells expressing full length tau (Fig. 3b,c, Supplementary Fig. 3j), while in cells expressing tau-ΔN, which does not form envelopes, the recovery was fastest and there was no detectable immobile fraction. Since cooperatively bound tau shows lower turnover[14], this data suggests that full length tau is bound to the microtubules in the form of a tau envelope. Interestingly, the recovery time and immobile fraction of the tau signal in tau-Cdk5 cells fell inbetween that of the control cells and the tau-ΔN cells, further supporting our in vitro data and indicating that phosphorylated tau is able to form envelopes, however, their turnover is faster and the envelopes are therefore less stable.

Tau binding is sensitive to pH of the environment in vitro as well as in cells[26,27]. It was shown that changing the pH of the media of cells manifests in the change of the intracellular pH, which can rapidly affect binding of tau to microtubules in cells[26]. As the presence of envelope-incorporated tau can be detected during the assembly or disassembly of the envelopes[14,15], we used pH change to directly test the presence of tau envelopes in cells by exchanging the media during imaging for a solution with slightly higher pH (from pH 7.4 to pH 8.4, Methods). In these conditions, any tau molecules that are non-cooperatively bound to the microtubule, due to their much higher turnover compared with tau in the envelopes, would be readily released from microtubules, while cooperatively bound tau forming envelopes would be more resilient to disassembly. Indeed, in our positive control cells expressing full length GFP-tau (denoted as tau), we observed gaps forming in the tau signal (manifested as increased coefficient of variation of the tau signal along the microtubule, Supplementary Fig. 3g,k) while the microtubules remained unaffected (coefficient of variation of the tubulin signal is not affected, Supplementary Fig. 3g,k). These gaps in the tau signal left clearly separated tau patches on the microtubules, strongly suggesting the presence of cooperatively binding tau molecules forming envelopes, constituting the observed patches (Fig 3d, t=0 min), and confirming our previous observations, where taxol treatment led to dissociation of tau from microtubules in cells in a patch-like pattern[15]. The advantage of the elevated pH treatment compared to the taxol treatment is that the tau unbinding is faster and reversible, which allowed us to analyze the re-binding of tau to microtubules. Presumably due to a recovery of the intracellular pH after the treatment, the gaps started to close and the tau patches regrew

(Fig 3d, t = 5 and 9 min), which is analogous to the growth of envelopes in vitro, when excess tau is available[14,15]. During the whole process, the density of the GFP-tau signal (GFP intensity per unit length) in the patches remained constant (Fig. 3f), further suggesting that these patches represent tau envelopes (which grow and shrink only at the boundaries). Within 9 minutes after the elevated-pH treatment, the microtubules regained full tau coverage (Fig. 3d, Supplementary Fig. 3g (whole cell images),k,l, Supplementary Movie 10). When we performed the elevated-pH treatment on tau-ΔN (incompetent of envelope formation), we did not detect any tau patches on the microtubules after the elevated-pH treatment (Fig 3e, t=0 min). Instead, we observed that the tau signal was removed uniformly and fully along the entire lengths of the microtubules (Fig. 3e, Supplementary Fig. 3g (whole cell images),k,l, Supplementary Movie 11), which suggests that tau molecules were bound to the microtubules individually, non-cooperatively. Subsequently, when following the recovery after elevated-pH treatment, we observed that the tau-ΔN signal returned, again uniformly, along the microtubule lattice. Unlike full-length tau molecules, which exhibited regrowth of the patches while remaining a constant density within the patches, the density of tau-ΔN signal on the microtubule uniformly increased during recovery (Fig. 3e,f, Supplementary Fig. 3g (whole cell images),k,l, Supplementary Movie 11). This further suggests that ΔN-tau, in these cells, does not form envelopes, and instead binds to microtubules non-cooperatively (i.e. with high turnover and high diffusivity). Strikingly, when following the recovery after elevated-pH treatment in the tau-Cdk5 cells, we observed that the reappearance and recovery of the signal occurred in a patch-like manner, closely resembling the reappearance of the tau signal in our positive control cells (Fig 3g, Supplementary Fig. 3g (whole cell images),k,l, Supplementary movie 12). Moreover, the density of the tau signal on microtubules within the patches remained constant throughout the treatment in the tau-Cdk5 cells (Fig. 3f), indicating that tau was bound cooperatively to the microtubules. Interestingly, the reappearance of the tau signal on microtubules was slower in tau-Cdk5 cells than in the control cells indicating that tau phosphorylation leads to slower envelope recovery (Fig. 3h). Combined, these data suggest that in control and tau-Cdk5 cells, the patches and the high-density tau areas covering microtubules consisted of cooperatively bound tau molecules forming cohesive tau envelopes, while N-terminally truncated tau in tau-ΔN cells bound non-cooperatively only. The fact that after the elevated-pH treatment, tau signal disappeared almost completely and reappeared slower in the tau-Cdk5 cells compared to

cells overexpressing control tau is in agreement with our in vitro data showing that tau phosphorylation does not prevent tau envelope formation but makes tau less prone to form envelopes and makes the resulting envelopes less stable. Combined, our data suggests that tau phosphorylation decreases the cohesiveness of tau envelopes, thereby negatively affecting the stability of the tau envelopes in living cells.

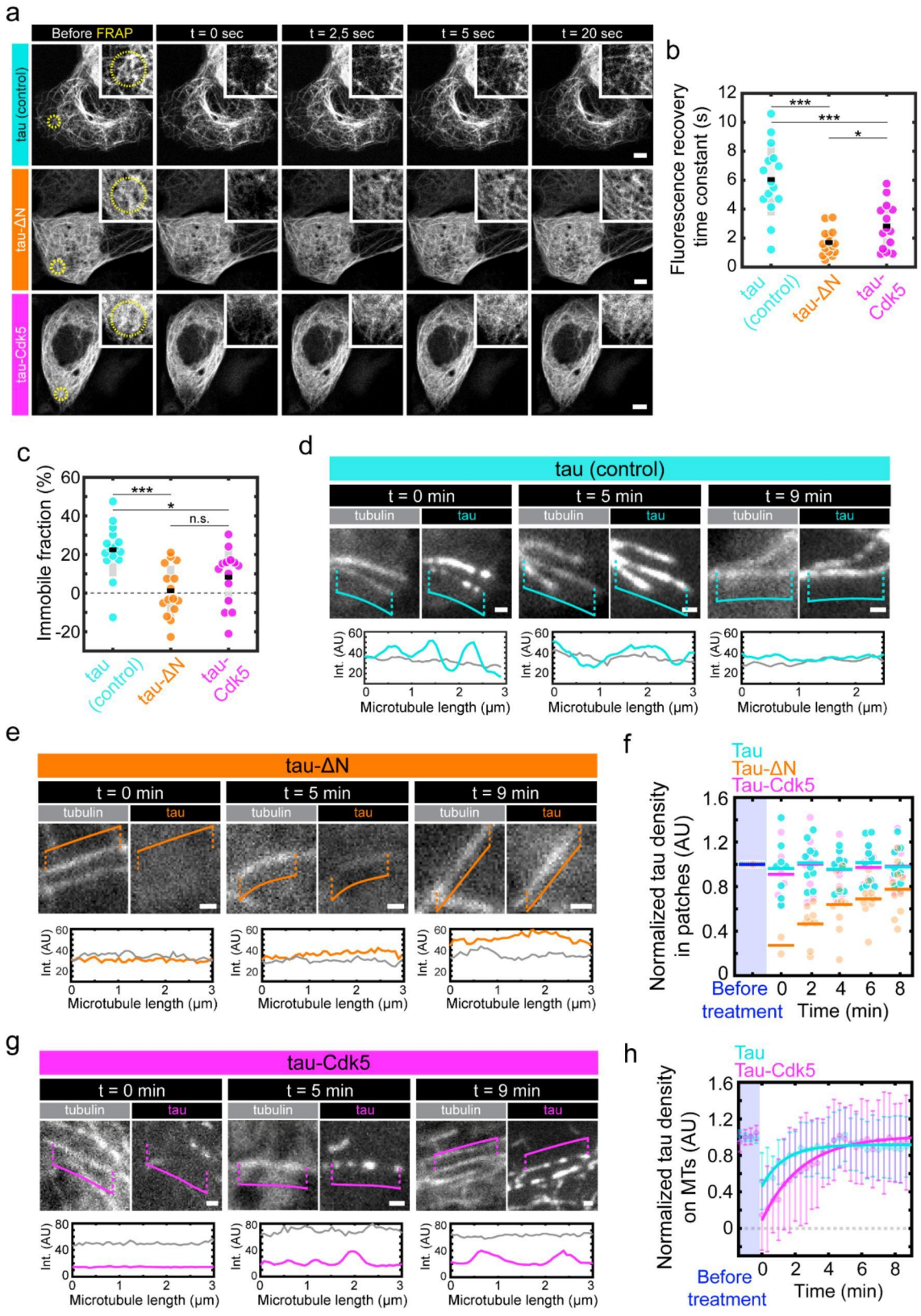

Fig. 3. Tau phosphorylation affects envelope formation in cells. a. Fluorescence micrographs of FRAP experiment on IMCD-3 cells expressing GFP-tau (control, cyan), GFP-tau-ΔN (tau-ΔN, orange), or GFP-tau with Cdk5/p25 (tau-Cdk5, magenta) at different timepoints before and after FRAP. The FRAP-region is drawn as a yellow-dotted circle in the left panels (before FRAP), a zoom-in containing the FRAP-region is shown in the top right corner of each micrograph.

Scale bars: 5µm. **b.** Time constant of the fluorescence recovery of the tau signal in the different groups. Time constant in control cells was 6.05 ± 2.50 sec (mean ± s.d., n=15 cells in 15 independent experiments); in tau-ΔN cells was 1.69 ± 0.89 sec (mean ± s.d., n=15 cells in 15 independent experiments); in tau-Cdk5 cells was 2.83 ± 1.61 sec (mean ± s.d., n=14 cells in 14 independent experiments). Two-sided t-test p-values (from left to right): $p=6.76*10^{-7}$, p=0.00034, p=0.0242. **c.** Immobile fraction measured from fluorescence recovery curve. Immobile fraction in control cells was 22.49 ± 13.77 % (mean ± s.d., n=15 cells in 15 independent experiments); in tau-ΔN cells 1.14 ± 13.15 % (mean ± s.d., n=15 cells in 15 independent experiments); in tau-Cdk5 cells 8.23 ± 14.52 % (mean ± s.d., n=14 cells in 14 independent experiments). Two-sided t-test p-values (left to right): p=0.000167, p=0.0114, p=0.179. . Fluorescence micrographs of IMCD-3 cells expressing mScarlet-tubulin and GFP-tau in control cells (tau, cyan) at t=0 min (left), t=5 min (middle), and t=9 min (right) after elevated-pH treatment. Corresponding linescans are shown below the micrographs. Different microtubules were selected at different timepoints due to dynamic behavior of the microtubules. Scale bars: 1µm. **e.** Fluorescence micrographs of mScarlet-tubulin and GFP-tau signal in tau-ΔN cells (orange) at t=0 min (left), t=5 min (middle), and t=9 min (right) after elevated-pH treatment. Corresponding linescans are shown below the micrographs. Different microtubules were selected at different timepoints due to dynamic behavior of the microtubules. Scale bars: 1µm. **f.** Normalized tau density in patches in GFP-tau control cells (tau, cyan) and GFP-tau-Cdk5/p25 cells (tau-Cdk5, magenta). Normalized tau density along the microtubule lattice (no patches are visible) in GFP-tau-ΔN cells (tau-ΔN, orange). Tau densities were measured at 5 timepoints after elevated-pH treatment and normalized to the tau density along the microtubules before the treatment (dark blue). **g.** Fluorescence micrographs of mScarlet-tubulin and GFP-tau signal in tau-Cdk5 (magenta) at t=0 min (left), t=5 min (middle), and t=9 min (right) after elevated-pH treatment. Corresponding linescans are shown below the micrographs. Different microtubules were selected at different timepoints due to dynamic behavior of the microtubules. Scale bars: 1µm. **h.** Time-trace of tau density on the MTs in the whole cell after elevated-pH treatment normalized to the tau density on the MT before the treatment in GFP-tau cells (tau, cyan) and GFP-tau-Cdk5/p25 cells (tau-Cdk5, magenta). Exponential time constant was 1.3 min for tau cells and 2.5 min for tau-Cdk5 cells (Methods).

Tau phosphorylation affects envelope functionality in vitro and in living cells

Finding that tau envelopes could be formed by tau in both its phosphorylated and non-phosphorylated states, albeit at different efficiencies, and that phosphorylation leads to compromised envelope integrity, we asked if tau phosphorylation additionally affects the functionality of the envelope. Tau envelopes regulate the accessibility of the microtubule surface for other microtubule-associated proteins, such as molecular motors or microtubule severing enzymes, thereby regulating their function[13,14]. To test if envelopes formed by phospho-tau and dephospho-tau differentially regulate typical molecular motors, like kinesin-1, and typical severing enzymes, like katanin, we employed in vitro reconstitution: in separate

measurement chambers, we formed envelopes of similar sizes either with dephospho-tau (5 nM) or phospho-tau (30 nM). Keeping the tau concentrations in solution, we then added kinesin-1 to the measurement chamber and studied the effect of the tau envelopes on kinesin-1. In accordance with previous findings[14], we found that molecules of kinesin-1 could walk on microtubules outside of the envelope regions and were mostly excluded from the envelopes (Supplementary Fig. 4a, Supplementary Movie 13,14). Quantifying the landing rate of kinesin-1 inside the envelope regions, we found no significant difference between the functioning of dephospho-tau and phospho-tau envelopes (Supplementary Fig. 4b). We then repeated the experiment with microtubule severing enzyme katanin. In line with previously published data[14,28], we observed that the regions of microtubules, which were covered only by diffusible tau and not by tau envelopes, were quickly disintegrated by katanin (Fig. 4a), confirming that the cooperatively-bound tau and not the diffusibly-bound tau, can protect microtubules against katanin severing. The envelope-coated regions of the microtubule were protected and prevailed for longer periods. While the density of tau envelopes remained constant (Supplementary Fig. 4c), the envelopes were slowly disassembled by katanin from their boundaries, with occasional severing events within the enveloped region (Fig. 4a, Supplementary Movie 15). The disassembly rate of enveloped regions from their boundaries did not show any significant difference between phospho-tau and dephospho-tau envelopes (Fig. 4b). However, we observed significantly increased rates of katanin severing events within the envelope regions formed by phosphorylated tau compared to non-phosphorylated tau (Fig. 4c), which may be explained by the reduced density of tau within envelopes formed by phospho-tau and reduced tau envelope integrity, as shown above. Combined, these experiments show that envelopes constituted by either phosphorylated or non-phosphorylated tau similarly inhibit kinesin-1 movement, while differentially protect against katanin-mediated severing. Tau phosphorylation thus, in addition to reducing the propensity of tau molecules to bind cooperatively, furthermore reduces the protective functionality of the formed tau envelopes.

We next asked if tau phosphorylation affects the functionality of envelopes in living cells. To test this, we prepared IMCD-3 cells overexpressing katanin-GFP (denoted as ‘katanin only’), or IMCD-3 cells overexpressing katanin-GFP in combination with mCherry-tau (denoted as ‘+ tau’), or mCherry-tau and Cdk5/p25 (denoted as ‘+ tau-Cdk5’). As a control we prepared

IMCD-3 cells overexpressing katanin-GFP in combination with Cdk5/p25 without overexpression of mCherry-tau (denoted as '+ Cdk5'). Cells were fixed 12 hours after transfection and stained for tubulin to visualize the presence of microtubules (Methods). In cells expressing katanin in absence of tau (Fig. 4d, transfected cells, yellow marker), a clear reduction in tubulin signal was observed in comparison with cells not expressing katanin (Fig. 4d,e, non-transfected cells, white marker). Consistent with previously published data[6,14], in cells expressing katanin in combination with tau, no reduction in tubulin signal was measured, indicating that tau protected microtubules against the severing activity of katanin, which is in agreement with our in vitro data. Strikingly, phosphorylation of tau by overexpression of Cdk5/p25, impeded this protective ability, resulting in a reduction in tubulin signal to similar level as in cells expressing katanin only or in cells expressing katanin in combination with Cdk5/p25 (Fig. 4d,e). Comparing the relative density of tubulin with the relative density of katanin 12 hours after transfection, we found that tubulin density inversely correlated with katanin density in all cell groups (Fig. 4f). This correlation was weaker in presence of tau, and stronger in presence of tau-Cdk5, further supporting the notion that phosphorylation of tau decreases its protective functionality (Fig. 4f). Combined, these experiments show that phosphorylation of tau impedes its protective functionality both in vitro and in living cells.

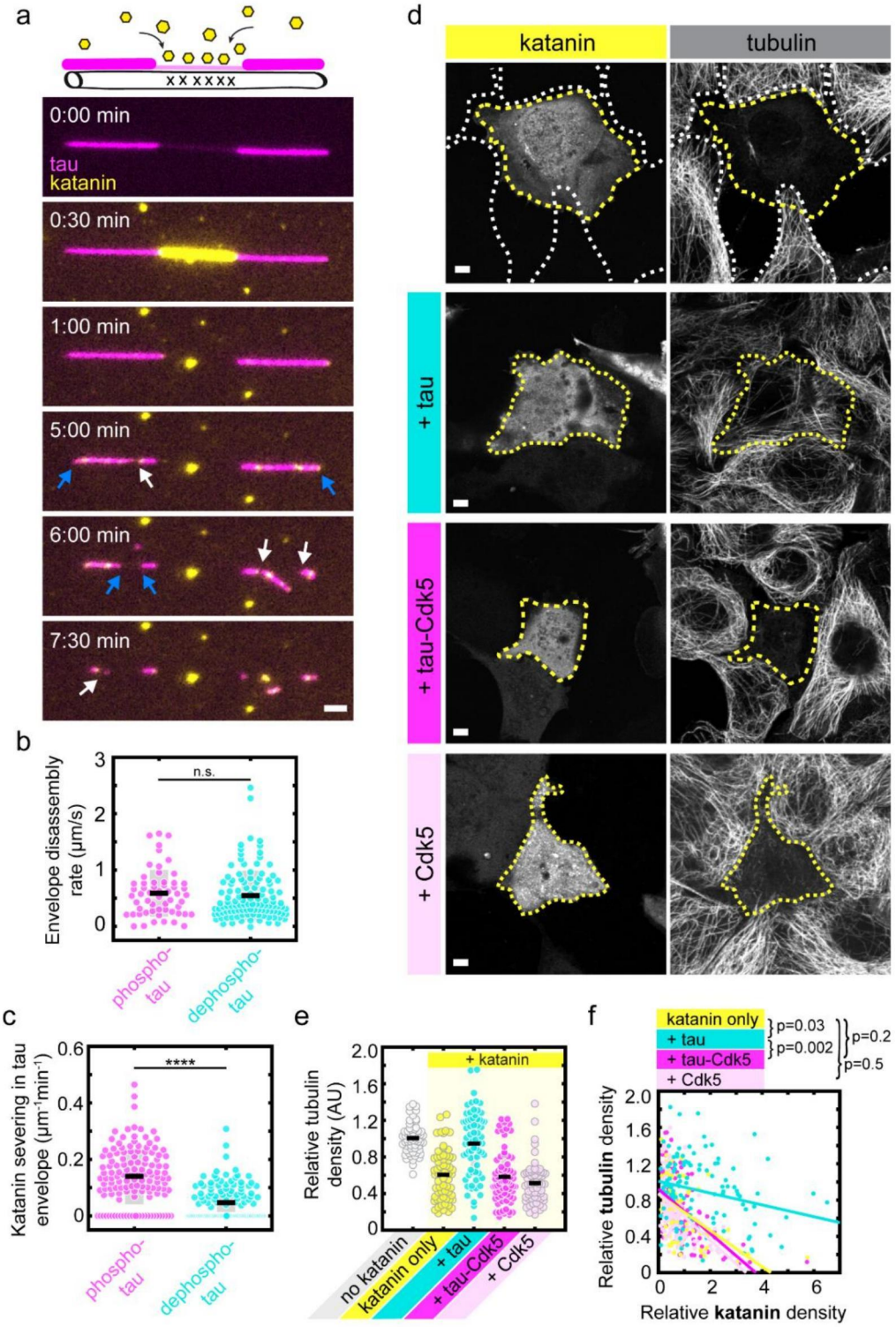

Fig 4. Tau phosphorylation affects envelope functionality in vitro and in living cells. a. Schematics and multichannel fluorescence micrographs showing rapid katanin-GFP-mediated severing of a microtubule region not covered by a tau envelope (panel 2, tau in magenta, katanin in yellow) and subsequently the much slower disassembly of the microtubule regions protected by a tau envelope (panels 3-6). Katanin severing leading to disassembly of envelope-covered portions of the microtubule from their boundaries is indicated by blue arrows, while occasional katanin severing within a tau envelope (severing event) is indicated by white arrows. Scale bar: 2 µm. **b**. Envelope disassembly rate from the boundaries due to

katanin severing of phospho-tau envelopes (magenta) was 0.59 ± 0.41 µm/s; dephospho-tau envelopes (cyan) was 0.50 ± 0.50 µm/s (mean ± s.d., n=57, 112 envelopes in 4,3 experiments). Two-sided t-test, p=0.2638. **c**. Katanin severing events within tau envelope boundaries in phospho-tau envelopes (magenta) was 0.14 ± 0.10 $\mu m^{-1}min^{-1}$; dephospho-tau envelopes (cyan) was 0.05 ± 0.06 $\mu m^{-1}min^{-1}$ (mean ± s.d., n=127,132 envelopes in 4,4 experiments). Two-sided t-test, $p=1.85*10^{-17}$. **d.** Fluorescence micrographs of IMCD-3 cells expressing katanin-GFP (left panels) and stained to visualize tubulin (right panels). Cells were fixed and stained 12 hours after transfection. Additionally, cells are expressing tau (+ tau, cyan), tau and Cdk5/p25 (+ tau-Cdk5, magenta), or Cdk5/p25 in the absence of tau (+ Cdk5, light pink). Cells expressing katanin are marked with a yellow dotted line and cells not expressing katanin (non-transfected cells) are marked with white dotted lines. Scale bars: 5µm. **e.** Relative tubulin density 12 hours after transfection. Relative tubulin density in 'no katanin' cells was 1.01 ± 0.16 (white), in 'katanin-only' cells was 0.61 ± 0.27 (yellow), in '+ tau' cells was 0.95 ± 0.35 (cyan), in '+ tau-Cdk5' cells was 0.58 ± 0.28 (magenta), in '+ Cdk5' cells was 0.51 ± 0.23 (light pink) (mean ± s.d., n=60, 64, 68, 71, 60 cells in 3 independent experiments). **f.** Correlation of the relative tubulin density (y-axis) compared to the relative katanin density (x-axis). Correlation coefficients of 'katanin only' is -0.49 (yellow), of '+ tau' is -0.25 (cyan), of '+ tau-Cdk5' is -0.57 (magenta), and of '+ Cdk5' is -0.54 (light pink). Correlation coefficient comparisons are indicated above the graph.

Discussion

Tau has been shown to modulate many neurodevelopmental processes through its interaction with microtubules, while its deregulation is associated with pathogenesis of numerous neurodegenerative disorders. It is known that phosphorylation regulates tau, but the detailed mechanism of how it affects tau function is still ill-understood. Here we show that phosphorylation of tau controls the formation of the protective tau envelopes. Tau envelopes are cohesive patches of cooperatively binding tau molecules characterized by limited lateral translocation and low turnover of the constituting tau molecules, which enclose the microtubule lattice and are selectively permeable for some proteins, while protecting the microtubules from others, for example the severing enzyme katanin[14]. This mode of tau binding to microtubules is contrasted by non-cooperative interactions of tau molecules binding individually, observed in vitro at low tau concentration[13,14] and upon disturbance of the cellular homeostasis, for example by pH-shock (Fig.4d-g). This non-cooperative mode of tau binding is characterized by rapid diffusion and high turnover of the individual tau molecules, which, in absence of cohesion, does not shield against the binding of other proteins, and thus leaves the microtubule lattice vulnerable to severing enzymes like

katanin[14]. Here, we showed that phosphorylation of tau impedes the envelope formation and integrity and reduces their protective functionality.

Previous results showed that tau phosphorylation reduces tau association with microtubules [19–21,29]. In accordance with these findings, we observed, outside of the tau envelopes, reduced binding of phosphorylated tau to microtubules, compared to non-phoshorylated tau. We suggest that increased binding of non-phosphorylated tau to the microtubule lattice and consequent higher tau densities on the microtubule lead to an increase in frequency of tau-tau encounters on the microtubule lattice, leading to a higher probability of nucleation of a tau envelope and increased envelope growth. Additionally, our finding that the relevant phosphorylation sites are located in the proline-rich regions and the C-terminus of tau (Fig. 2b), but not in the microtubule binding repeats (a) demonstrates that phosphorylation of tau domains other than the binding repeats play a significant role in the interaction of tau with the microtubule lattice, and (b) suggests that tau-tau interaction might play a significant role in the envelope formation. This notion is consistent with the observation that tau molecules, under certain conditions, can phase-separate[30] and that phosphorylation regulates condensate formation[31]. For both reasons (a) and (b), the concentration required to achieve comparable microtubule envelope coverage, is much higher for phosphorylated tau as compared to non-phosphorylated tau. At any given tau concentration, phosphorylated tau generated envelopes which cover, and thus protect, a smaller fraction of the microtubule surface, leaving it completely uncovered at low nanomolar concentrations. The reduced protection resulting from tau phosphorylation could be due to higher turnover of phosphorylated tau, which might result in transient defects in the envelope. Thus, in cells, tau phosphorylation, at any given tau concentration, will dramatically reduce microtubule envelope coverage and thereby protection. And, importantly, due to the reduced protection, microtubule instability can be observed even before tau envelope disassembly occurs.

As non-phosphorylated tau more readily participates in envelope formation, our data suggests that the different affinities are not the only reason for the observed effect of the phosphorylation on tau envelope behavior. Our data suggest that, additionally, the increased envelope coverage observed for non-phosphorylated tau may be due to stronger tau-tau interactions on the microtubule surface, creating a more cohesive and impenetrable

structure. Tau phosphorylation weakens these interactions and creates a structure that is easier to penetrate by microtubule severing enzymes such as katanin. This notion is corroborated by the finding that phosphorylated tau forms envelopes that have lower tau density compared to dephosphorylated tau envelopes (suggesting weaker tau-tau interactions) and that katanin severs microtubules even within the boundaries of envelopes consisting of phosphorylated tau. This hypothesis is especially plausible when considering the position of phosphorylation in our phospho-tau samples: While little phosphorylation was detected within the binding repeats (R1-R4 and R'), which directly interact with the microtubule, most phosphorylation was detected in the projection domains of tau (in particular P1, P2, and the C-terminus), which are the regions thought of as establishing tau-tau interaction[13,14].

Increased tau phosphorylation has been detected in multiple neurodegenerative disorders and has been associated with formation of phosphorylated tau aggregates[32,33]. The specific effect of tau phosphorylation in the pathogenesis of different diseases is still being analyzed. Using in vitro and in vivo models we demonstrate that increased phosphorylation interferes with formation of protective tau envelopes. Moreover, we show that the presence of phosphorylated tau leads to disassembly of already formed tau envelopes. This can critically amplify the deleterious effect of phospho-tau on neurons as release of tau from envelopes may locally increase its concentration and promote formation of phosphorylated tau aggregates with additional toxic effect on neuronal transport and function.

Tau is phosphorylated by numerous kinases in healthy neurons, but deregulation of Cdk5 seems critical in the neuropathological process leading to neurodegeneration. We now demonstrate that upregulation of Cdk5 has a deleterious effect on microtubule protective functions of tau envelope formation and maintenance, and that microtubules covered by tau envelopes formed by phosphorylated tau are more prone to disintegration, e.g. by microtubule severing enzymes, such as katanin. Thus, by linking Cdk5 upregulation with tau phosphorylation and tau envelope disintegration, our work provides a mechanism of microtubule regulation in cells and in pathogenesis of neurodegenerative disorders, such as Alzheimer's disease. Neurodegeneration and microtubule destabilization is often linked to

tau hyper-phosphorylation. Our results suggest that microtubule destabilization could be the result of the impaired protective functionality of tau envelopes upon phosphorylation of tau.

References

1. Mitchison, T. & Kirschner, M. Dynamic instability of microtubule growth. *Nature* **312**, 237–42 (1984).
2. Drechsel, D. N., Hyman, A. A., Cobb, M. H. & Kirschner, M. W. Modulation of the dynamic instability of tubulin assembly by the microtubule-associated protein tau. *Mol. Biol. Cell* **3**, 1141–1154 (1992).
3. Kowalski, R. J. & Williams, R. C. Microtubule-associated protein 2 alters the dynamic properties of microtubule assembly and disassembly. *J. Biol. Chem.* **268**, 9847–55 (1993).
4. McNally, F. J. & Vale, R. D. Identification of katanin, an ATPase that severs and disassembles stable microtubules. *Cell* **75**, 419–29 (1993).
5. Qiang, L. *et al.* Tau does not stabilize axonal microtubules but rather enables them to have long labile domains. *Curr. Biol.* **28**, 2181–2189 (2018).
6. Qiang, L., Yu, W., Andreadis, A., Luo, M. & Baas, P. W. Tau protects microtubules in the axon from severing by katanin. *J. Neurosci.* **26**, 3120–3129 (2006).
7. Berger, Z. *et al.* Accumulation of pathological tau species and memory loss in a conditional model of tauopathy. *J. Neurosci.* **27**, 3650–62 (2007).
8. Lasagna-Reeves, C. A. *et al.* Identification of oligomers at early stages of tau aggregation in Alzheimer's disease. *FASEB J.* **26**, 1946–59 (2012).
9. Guo, T., Noble, W. & Hanger, D. P. Roles of tau protein in health and disease. *Acta Neuropathol.* **133**, 665–704 (2017).
10. Lee, G. & Leugers, C. J. Tau and tauopathies. *Prog. Mol. Biol. Transl. Sci.* **107**, 263–93 (2012).
11. Schneider, A., Biernat, J., von Bergen, M., Mandelkow, E.-M. & Mandelkow, E. M. Phosphorylation that detaches tau protein from microtubules (Ser262, Ser214) also protects it against aggregation into Alzheimer paired helical filaments. *Biochemistry* **38**, 3549–58 (1999).
12. Cho, J.-H. & Johnson, G. V. W. Glycogen synthase kinase 3beta phosphorylates tau at both primed and unprimed sites. Differential impact on microtubule binding. *J. Biol.*

Chem. **278**, 187–93 (2003).

13. Tan, R. *et al.* Microtubules gate tau condensation to spatially regulate microtubule functions. *Nat. Cell Biol.* **21**, 1078–1085 (2019).
14. Siahaan, V. *et al.* Kinetically distinct phases of tau on microtubules regulate kinesin motors and severing enzymes. *Nat. Cell Biol.* **21**, 1086–1092 (2019).
15. Siahaan, V. *et al.* Microtubule lattice spacing governs cohesive envelope formation of tau family proteins. *Nat. Chem. Biol.* **18**, 1224–1235 (2022).
16. Henrichs, V. *et al.* Mitochondria-adaptor TRAK1 promotes kinesin-1 driven transport in crowded environments. *Nat. Commun. 2020 111* **11**, 1–13 (2020).
17. Cruz, J. C., Tseng, H.-C., Goldman, J. A., Shih, H. & Tsai, L.-H. Aberrant Cdk5 activation by p25 triggers pathological events leading to neurodegeneration and neurofibrillary tangles. *Neuron* **40**, 471–83 (2003).
18. Kimura, T., Ishiguro, K. & Hisanaga, S. Physiological and pathological phosphorylation of tau by Cdk5. *Front. Mol. Neurosci.* **7**, 65 (2014).
19. Cho, J.-H. & Johnson, G. V. W. Primed phosphorylation of tau at Thr231 by glycogen synthase kinase 3beta (GSK3beta) plays a critical role in regulating tau's ability to bind and stabilize microtubules. *J. Neurochem.* **88**, 349–58 (2004).
20. Biernat, J., Gustke, N., Drewes, G., Mandelkow, E. M. & Mandelkow, E. Phosphorylation of Ser262 strongly reduces binding of tau to microtubules: distinction between PHF-like immunoreactivity and microtubule binding. *Neuron* **11**, 153–63 (1993).
21. Lindwall, G. & Cole, R. D. Phosphorylation affects the ability of tau protein to promote microtubule assembly. *J. Biol. Chem.* **259**, 5301–5305 (1984).
22. Preuss, U., Döring, F., Illenberger, S. & Mandelkow, E. M. Cell cycle-dependent phosphorylation and microtubule binding of tau protein stably transfected into Chinese hamster ovary cells. *Mol. Biol. Cell* **6**, 1397–1410 (1995).
23. Nigg, E. A. Mitotic kinases as regulators of cell division and its checkpoints. *Nat. Rev. Mol. Cell Biol.* **2**, 21–32 (2001).
24. Gamblin, T. C., Berry, R. W. & Binder, L. I. Modeling tau polymerization in vitro: a review and synthesis. *Biochemistry* **42**, 15009–15017 (2003).
25. Reynolds, M. R., Berry, R. W. & Binder, L. I. Site-specific nitration differentially influences tau assembly in vitro. *Biochemistry* **44**, 13997–14009 (2005).

26. Charafeddine, R. A. *et al.* Tau repeat regions contain conserved histidine residues that modulate microtubule-binding in response to changes in pH. *J. Biol. Chem.* **294**, 8779–8790 (2019).
27. Hinrichs, M. H. *et al.* Tau Protein Diffuses along the Microtubule Lattice. *J. Biol. Chem.* **287**, 38559–38568 (2012).
28. Sudo, H. & Baas, P. W. Strategies for diminishing katanin-based loss of microtubules in tauopathic neurodegenerative diseases. *Hum. Mol. Genet.* **20**, 763–78 (2011).
29. Drewes, G. *et al.* Microtubule-associated protein/microtubule affinity-regulating kinase (p110mark). A novel protein kinase that regulates tau-microtubule interactions and dynamic instability by phosphorylation at the Alzheimer-specific site serine 262. *J. Biol. Chem.* **270**, 7679–88 (1995).
30. Hernández-Vega, A. *et al.* Local nucleation of microtubule bundles through tubulin concentration into a condensed tau phase. *Cell Rep.* **20**, 2304–2312 (2017).
31. Söding, J., Zwicker, D., Sohrabi-Jahromi, S., Boehning, M. & Kirschbaum, J. Mechanisms for Active Regulation of Biomolecular Condensates. *Trends Cell Biol.* **30**, 4–14 (2020).
32. Grundke-Iqbal, I. *et al.* Microtubule-associated protein tau. A component of Alzheimer paired helical filaments. *J. Biol. Chem.* **261**, 6084–9 (1986).
33. Stoothoff, W. H. & Johnson, G. V. W. Tau phosphorylation: physiological and pathological consequences. *Biochim. Biophys. Acta* **1739**, 280–97 (2005).
34. Jiang, K. *et al.* Microtubule minus-end regulation at spindle poles by an ASPM-katanin complex. *Nat. Cell Biol.* **19**, 480–492 (2017).
35. Henrichs, V. *et al.* Mitochondria-adaptor TRAK1 promotes kinesin-1 driven transport in crowded environments. *Nat. Commun.* **11**, 3123 (2020).
36. Castoldi, M. & Popov, A. V. Purification of brain tubulin through two cycles of polymerization-depolymerization in a high-molarity buffer. *Protein Expr. Purif.* **32**, 83–8 (2003).
37. Schindelin, J. *et al.* Fiji: an open-source platform for biological-image analysis. *Nat. Methods* **9**, 676–682 (2012).
38. Liu, H. & Naismith, J. H. An efficient one-step site-directed deletion, insertion, single and multiple-site plasmid mutagenesis protocol. *BMC Biotechnol.* **8**, 91 (2008).
39. Chu, D. T. W. & Klymkowsky, M. W. The appearance of acetylated alpha-tubulin

during early development and cellular differentiation in Xenopus. *Dev. Biol.* **136**, 104–17 (1989).

Methods

Protein constructs and purification

Insect cell expressed tau

For in vitro experiments, GFP- or mCherry-labelled tau (h441-tau; NM_005910.6:151-1476) was expressed in insect cell and purified using the baculovirus expression system (DefBac DNA). Sf9 cells were infected with 8 ml of P2 baculovirus stock (1:100 ratio of P2 virus to cell culture), incubated at 27°C with moderate shaking, and harvested 72 hours post infection. Cells were harvested by centrifugation at 300 x g for 10 min and resuspended in PBS before snap-freezing the cells, or prior to purification in lysis buffer (25 mM HEPES pH 7.4, 150 mM KCl, 20 mM imidazole, with 1 mM DTT, benzonase (1.25 µL of 25 U/µl, 70664, Novagen) and 1x Protease inhibitor cocktail (34044100, Roche Diagnostics GmBH). Cells were lysed by spinning at 70000 x g for 1 hour at 4°C and collecting the supernatant. The lysate was incubated with NiNTA agarose resin (XF340049, Thermo Scientific) HiTrap for 2 hours at 4°C by slowly rotating. After incubation, beads were washed with 3x20 ml wash buffer (25 mM HEPES, 150 mM KCl (or 700 mM KCl in wash step 2), 1mM DTT, 20 mM imidazole). 6xhis tag was removed by incubating the beads with PreScission protease (homemade 3C HRV protease, 1:100, 1µg enzyme/100 µg of protein, overnight at 4°C while rotating). The next day the cleaved protein was collected and concentrated by spinning the sample at 3500 RPM at 4°C using -50kDa centrifugal filter tube (Amicon Ultra-15, Merck). The protein was purified by size-exclusion chromatography using a Superdex 200 10/300 GL column (GE28-9909-44, Sigma) with an NGC Chromatography system (Bio-Rad), equipped with ChromLab software (Bio-Rad) in 25 mM HEPES pH 7.4, 150 mM KCl, 1 mM DTT, 0.1 mM ATP, 1 mM EDTA. Collected peak fractions were concentrated to 10-40 µM using -50kDa centrifugal filter tube (Amicon Ultra-15, Merck). Protein concentration was measured with a NanoDrop ND-1000 spectrophotometer (Thermo Scientific) at 280 nm absorbance. Proteins were flash-frozen in liquid nitrogen and stored at -80°C. All steps in the purification were performed at 4°C.

Bacterial cell expressed tau

Fluorescently tagged tau used for in vitro experiments (h441-tau was subcloned into the expression vector based on pET11Kan-N-HIS6-3C-mNeonGreen or pET11Kan-N-HIS6-3C-mRuby3) was expressed in E. coli BL21(DE3)-RIPL strain. The cells were grown at 30°C until OD_{600} of 0.5-0.6, the protein expression was then induced by 0.1 mM IPTG, and the cells were grown overnight at 16°C. Bacterial cells (3-4 g) were lysed in 45 ml of lysis buffer (50 mM Tris pH 8.0, 300 mM NaCl, 2 mM bME, 20 mM Imidazole, 0.5 µL Benzonase, and 1x Protease inhibitor cocktail), sonicated (5 min; On/Off: 2/4 s) and centrifuged (40000 x g; 30 min; 4 °C). The soluble fraction was then subjected to Strep-Tactin XT purification (washing buffer: 50 mM Tris pH 8.0, 300 mM NaCl, 2 mM bME), and eluted using BXT buffer (100 mM Tris pH 8.0, 150 mM NaCl, 1 mM EDTA, 50 mM Biotin). The purified protein was concentrated using VivaSpin-10kDa-HY and subjected to Size exclusion chromatography (see Insect cell expressed tau; buffer: 50 mM Tris pH 8.0, 300 mM NaCl, 1 mM DTT). Protein concentration was measured with a NanoDrop (see Insect cell expressed tau) at 280 nm absorbance. Proteins were flash-frozen in liquid nitrogen and stored at -80°C. All purification steps were performed at 4°C.

Katanin + Kinesin expression and purification

Katanin-GFP[34] (p60 & p80-GFP)and kinesin-1-GFP[35] were expressed and purified as previously described.

TIRF microscopy

Total internal reflection fluorescent (TIRF) microscopy experiments were performed on an inverted microscope (Nikon-Ti E, Nikon TI2 E) with H-TIRF module or iLas2 equipped with 60x or 100x NA 1.49 oil immersion objectives (Apo TIRF or SR Apo TIRF, respectively, Nikon) and CMOS Hamamatsu Orca Flash 4.0 LT, sCMOS Hamamatsu ORCA 4.0 V2, or PRIME BSI (Hamamatsu Photonics, Teledyne Photometrics) cameras. Microtubules were visualized using interference reflection microscopy (IRM) and fluorescent proteins by switching between microscope filter cubes for EGFP, mCherry, and Cy5 channels or by using a quad band set (405/488/561/640). The microscopes were controlled with Nikon NIS Elements software (v5.02, v5.20 or v5.42). All experiments were performed at room temperature by several experimentalists over the course of multiple months. No data was excluded from the study.

Experimental chamber preparation

For TIRF experiments, chambers were assembled by melting thin strips of parafilm in between two glass coverslips silanized with 0.05% dichlorodimethylsilane (DDS, #440272, Sigma). The chambers were incubated with 20 µg/mL anti-biotin antibodies (in PBS, #B3640, Sigma) for 5 min or 20 µg/mL anti-β-tubulin antibodies (in PBS, #T7816, Sigma) for 5 min, followed by 1% Pluronic (F127 in PBS, #P2443, Sigma) for at least 30 min. (Biotin-labeled) Microtubules (Methods) were diluted into BRB80T (BRB80: 80mM PIPES pH 6.9, 1mM EGTA, 1mM MgCl2, supplemented with 10 µM paclitaxel (#17191, Sigma)), then incubated in the chamber and allowed to adhere to the antibodies for 30 sec. Unbound microtubules were washed away with BRB80T and chambers were pre-incubated with TIRF assay buffer AB (50 mM HEPES pH 7.4, 1 mM EGTA, 2 mM $MgCl_2$, 75 mM KCl, 10 mM dithiothreitol, 0.02 mg/ml casein, 10 µM taxol, 1 mM Mg-ATP, 20 mM D-glucose, 0.22 mg/ml glucose oxidase and 20 µg/ml catalase) prior to experiments. Unless stated otherwise, all experiments were conducted in TIRF assay buffer (AB). All experiments were quantified by pooling data from multiple chambers performed on at least two different days. Chambers were never re-used for additional experiments.

Microtubule Assembly

Porcine brains were obtained from a local abattoir and used within ~4 h of death. Porcine brain tubulin was isolated using the high-molarity PIPES procedure[36]. Biotin-labeled tubulin was purchased from Cytoskeleton Inc. (#T333P) and diluted 1:50 with unlabeled porcine brain tubulin to obtain biotin-labeled tubulin mix for surface-immobilization assays using biotin antibodies.

Taxol-stabilized microtubules (GTP polymerized, then taxol-stabilized; stored and imaged in presence of taxol) were polymerized from 4 mg/ml tubulin for 30 min at 37°C in BRB80

supplemented with 4 mM $MgCl_2$, 5% DMSO, and 1mM GTP (#NU-1012, Jena Bioscience). The polymerized microtubules were diluted in BRB80T and centrifuged for 30 min at 18000 x g in a Microfuge 18 Centrifuge (Beckman Coulter). After centrifugation the pellet was resuspended and kept in BRB80T at room temperature.

GMPCPP-microtubules (GMPCPP polymerized, then taxol-stabilized; stored and imaged in presence of taxol) were polymerized from 4 mg/ml tubulin for 2 h at 37°C in BRB80 supplemented with 1mM $MgCl_2$ and 1mM GMPCPP (#NU-405, Jena Bioscience). The polymerized microtubules were centrifuged for 30 min at 18000 x g in a Microfuge 18 Centrifuge (Beckman Coulter). After centrifugation the pellet was resuspended and kept in BRB80T at room temperature.

GDP-microtubules (GTP polymerized, then glycerol-stabilized; stored and imaged in presence of 40% glycerol) were polymerized as described for taxol-stabilized microtubules. After polymerization, the microtubules were gently diluted in BRB80-Gly40 buffer (80 nM PIPES, 2 mM $MgCl_2$ and 1 mM EGTA, pH 6.8, 40% glycerol) and centrifuged as described above. After centrifugation the supernatant was discarded, and the pellet was resuspended gently in 50 μl of BRB80-Gly40. Microtubules were then kept at room temperate at least 1 hour (maximum overnight) before usage.

Tau sample preparation

To study the effect of phosphorylation of tau on envelope formation 4 samples were produced with various degrees of phosphorylation, as described below:

Phospho-tau. Tau expressed in insect cells, treated with buffer in absence of Alkaline Phosphatase. 2μM (0,2 mg/ml) insect cell expressed tau was incubated in 1x Fast Phosphatase Buffer (stock 10x) for 15 min at 37°C.

Dephospho-tau. Tau expressed in insect cells, treated with Alkaline Phosphatase (FastAP Phosphatase, #EF0651, Themofisher). 2μM (0,2 mg/ml) insect cell expressed tau was incubated with 2,5 g/mol Alkaline Phosphatase (stock 10 g/mol) and 1x Fast Phosphatase Buffer (stock 10x) for 15 min at 37°C.

Bact-tau. Tau expressed in bacterial cells, treated with buffer in absence of Cdk5/p35 kinase. 2μM (0,2 mg/ml) Bact-tau was incubated in Reaction Buffer A (K03-09, stock 5x) supplemented with 50μM DTT, 50μM ATP for 15 min at 37°C.

Bact-Cdk5-tau. Tau expressed in bacterial cells, treated with Cdk5/p35 kinase (#V3271, Promega). 2μM (0,2 mg/ml) Bact-tau was incubated in Reaction Buffer A (K03-09, stock 5x) supplemented with 50μM DTT, 50μM ATP and 0.02 μg/μl Cdk5/p35 kinase (stock 0.1 μg/μl) for 15 min at 37°C.

TIRF assays

In all TIRF experiments, chambers were prepared as described above and microtubules were observed using interference reflection microscopy (IRM). Movies were captured with

appropriate frame interval and analysis was done after a certain incubation time as stated in the caption or methods.

Tau on microtubules. Tau samples were diluted in AB to the final concentration stated in the main text. After microtubule incubation, the diluted tau sample was added to the measurement chamber with at least four-fold amount of the chamber volume.

Cdk5 treatment in channel. Tau-mNeonGreen was diluted in AB buffer (supplemented with 0.5 mg/ml casein) to final concentration 15 nM and incubated on surface-immobilized microtubules for 10 min. After incubation, either i) active cdk5/p35 (activity: 0.1 μg/μl, diluted 10x) or ii) deactivated cdk5/p35 (deactivated by incubating at 95 °C for 10 min, diluted 10x), were added to the chamber, while tau concentration remained unchanged. Tau envelopes were observed for 15 min.

Kinesin-1 assay. Phospho-tau-mCherry or dephospho-tau-mCherry were diluted to concentrations at which envelopes of similar microtubule coverage assembled (30 nM and 5 nM, respectively). After microtubule incubation, tau was added to the measurement chamber and incubated for 3 minutes after which 25 nM kinesin-1-GFP was added in the presence of tau. Microtubules and the location of the tau envelopes were determined by taking a snapshot after which kinesin-1 was imaged for 30 sec using single molecule approach (no delay, 20 ms exposure time).

Katanin assay. Dephospho-tau-mCherry or phospho-tau-mCherry was diluted in AB and incubated on surface-immobilized microtubules for 5 min. Concentrations of dephospho- and phospho-tau were chosen such as to achieve similar microtubule coverage (0.8 nM for dephospho-tau and 3.5 nM for phospho-tau). After incubation, 100 nM katanin-GFP was added to the measurement chamber in presence of the established tau concentration. Chambers were imaged for 30 min with 5 sec interval.

Tau on GDP-microtubules. Tau-mCherry (insect cell expressed) was dephosphorylated using phosphatase as stated above. Dephosphorylated or phosphorylated (untreated) tau diluted in BRB80-Gly40-AB was added to surface immobilized GDP-microtubules (glycerol-stabilized) at concentrations: 0.2 nM, 1 nM, 2 nM, 4 nM, 10 nM, 50 nM or 100 nM, and incubated for 5 minutes. For the lower concentrations (0.2-4nM), tau was sequentially added to the same experimental chamber. For concentrations 10 nM and above, a new channel was used for every concentration. All experiments with Glycerol-stabilized microtubules were performed in BRB80-Gly40 buffer to ensure that microtubules remained stable. For in vitro TIRF assays, BRB80-Gly40 buffer was supplemented with 10 mM dithiothreitol, 20 mM d-Glucose, 1 mM ATP, 0.02 mg/ml Casein, 0.22 mg/ml Glucose Oxidase and 0.02 mg/ml Catalase (henceforth called BRB80-Gly40-AB).

Cdk5 treatment with tau envelope disassambly. Tau-mNeonGreen (bacterial expressed) was diluted in AB to a final concentration between 10-20 nM and incubated on surface-immobilized microtubules for 5 min. After incubation, tau was removed from the channel by the addition of 20 μl AB that contained either i) active Cdk5/p35 (activity: 0.1 μg/μl, diluted 10x), ii) deactivated Cdk5/p35 (deactivated by incubating at 95 °C for 10 min, diluted 10x) or iii) in absence of any kinase (i.e only AB, control). The disassembly of tau envelopes was

observed for: 5 min (for active Cdk5); 10-45 min (for deactivated Cdk5); and 10 min (for control).

TIRF Image analysis

Microscopy data were analyzed using ImageJ 2.3.0/1.53t (FIJI)[37] and custom written Matlab (R2020b) codes. In images with substantial drift, the 'StackregJ' plugin was used to correct the drift (kindly provided by Jay Unruh at Stowers Institute for medical research in Kansas City, MO).

Kymographs. Kymographs were generated by drawing a line along the microtubule lattice and using the ImageJ kymographBuilder plugin.

Envelope coverage. Microtubule lengths were measured by using the IRM signal, tau envelope lengths were measured by using the fluorescent signal after 3 min of incubation. The envelope coverage represents the sum of all tau envelopes lengths divided by the sum of all microtubule lengths within one field of view.

Coverage difference after Cdk5 treatment. Tau envelope coverage difference was calculated by subtracting coverage by tau envelopes before the addition of active/deactivated cdk5/p35 and after 15 min after adding active/deactivated cdk/p35. Coverage was measured as described above.

Tau envelope growth rate. Length of the dephospho-tau envelopes was measured prior to (t=0 min) the 45 min incubation with either phospho- or dephospho-tau and then at the end of the experiment (t=45 min). The difference between the two lengths was calculated and subsequently divided by time to get the growing/shrinking rate (µm/min) of each tau envelope.

Tau density estimation. Tau density on the microtubules was measured in ImageJ by drawing a rectangle around the microtubule and measuring the mean. For background-subtraction the rectangle was then moved to an area directly adjacent to the microtubule where no microtubule is present and the mean was measured again and subtracted from the mean on the microtubule.

Affinities (Tau density plotted against tau concentration). GMPCPP-lattice microtubules were immobilized on the coverslips surface and increasing concentrations of phosphorylated or dephosphorylated tau were added to the measurement chamber. The tau density was then measured on the microtubule lattice and plotted against the tau concentration in nM as a measure of the affinity of tau to the microtubule.

Fraction of phospho-tau in- or outside envelope region. Chambers were prepared as described above. 8.5 nM dephospho-tau-mCherry was mixed with 8.5 nM phospho-tau-mCherry (diluted in AB). The tau mixture was incubated on surface-immobilized microtubules for 5 min. The fraction of phospho-tau within the envelope was calculated as the density of phospho- tau in the enveloped region, divided by the total density of phospho- and

dephospho-tau within the same region. The fraction of phospho-tau outside the envelope region was calculated as the density of phospho- tau in the non-enveloped region, divided by the total density of phospho- and dephospho-tau within the same region.

Envelope disassembly rate due to Cdk5 treatment. The envelope length was measured at the start of the video (before tau removal), and after 5-45 min (see above). Envelope lengths were determined by eye and measured using ImageJ. The disassembly rate was calculated as the difference in the envelope lengths at the beginning and at the end of the video, divided by the time between the two measurements. If an envelope disappeared fully before the end of the video, the beginning length was divided by the time it took for the envelope to completely disassemble.

Gaps in disassembling envelopes. Gaps appearing during the disassembly of the tau envelopes were counted manually. The number of gaps on each envelope were then divided by the envelope length at the start of the movie and by the length (in sec) of the movie.

Tau density on GDP-microtubules. The maximum intensity projection from the last 5 frames of the video was made to eliminate the impact of slight fluorescent intensity fluctuations on the intensity measurements. The mean intensity of tau signal on microtubules was measured from these maximum intensity projections, subtracted by the mean intensity of the background and divided by 5 (number of frames). Mean intensities were measured for all tested concentrations.

Kinesin landing rate. Kinesin-1 landings were counted manually from kymographs of the kinesin channel. Kinesin-1 landings were counted when landings visually appeared to be kinesin-1 molecules (based on fluorescence intensity and size).

Katanin-mediated microtubule disassembly rate. Katanin-mediated microtubule disassembly rate was measured as the change of envelope length over time. Tau envelopes were measured at their longest length and at the end of the captured movie (t=30 min). If a tau envelope disassembled completely before t=30 min, the disappearance of the fluorescence signal marked the end of the measurement. Envelope length was measured by manually drawing a line along the envelope in ImageJ and calculating the length in nm. Subsequently, the lengths were divided by time in sec and normalized to the length of the envelope prior to disassembly (at t=0 min).

Katanin severing in envelope. Katanin severing events were counted manually from fluorescence videos. Severing events were counted when a clear gap appeared in the tau-mCherry signal and disassembly of the microtubule was observed from the newly acquired boundaries.

Normalized tau density in envelopes after katanin addition. Tau density was measured at 5 timepoints after addition of katanin. First frame after katanin addition marks t=0 min. Tau density was measured within the envelope region, and normalized to the tau density within the same envelope at t=0 min.

Live-cell experiments

Plasmids

Human tau sequence (h441-tau) N-terminally tagged with eGFP in pCDNA.4 vector was used as control tau. Tau sequence with deleted N terminus (tau 242-441) was created from control tau using one-step site-directed deletion[38]; primers Fwd: CGGCCGCACGCCTGCAGACAGCCCCCGTGCCCAT, Rev: GCAGGCGTGCGGCCGCGGCTCCGAATTCTTTGTATAGT). Human tubulin sequence (TUBA1B) fused with mScarlet was used for lentiviral and retroviral particles production. To increase the phosphorylation level, co-transfection was used with vectors pCDNA3 overexpressing Cdk5 and p25. For katanin overexpression, co-transfection of pLL vectors expressing katanin subunit p60 and GFP-tagged katanin subunit p80 was used.

Tau lysate preparation

HEK293T cells were co-transfected either with GFP-tau and empty pCDNA3 vector (1:1) or with GFP-tau and vectors pCDNA3 overexpressing Cdk5 and p25 (1:0.85:0.15) using linear Polyethylenimine (PEI; Polysciences, Inc.). Cells were harvested 48 hours after transfection by centrifugation and flash-frozen. Cell pellets were resuspended in 0.5 pellet volumes of lysis buffer (BRB80 supplemented with 1x phosphatase inhibitors (#4906845001, Sigma), 1x protease inhibitors (#04693159001, Sigma) and 0.05% Triton X-100 (# X100, Sigma)). The mixture was sonicated with three short pulses using the sonotrode MS1 (Hielscher Ultrasonics), setting “cycle” 1, “amplitude” 100% (30 kHz) on ice. The solution was transferred to 270 µl Beckman ultracentrifuge tubes and ultra-centrifuged in the Beckman 42.2 Ti rotor at 30000 x g, 4°C for 30 min in the Beckman Coulter Optima XPN-90 ultracentrifuge. The supernatant was directly used for experiments or flash-frozen in liquid nitrogen and stored at -80 °C. Lysate concentrations were measured at 488nm absorbance using NanoDrop ND-1000 spectrophotometer (Thermo Scientific).

Tau lysate imaging

Chambers were prepared as described before. Tau lysates were diluted 10x in AB buffer and added to surface-immobilized microtubules where tau envelope formation was captured for 3 min with 5 sec interval.

Elevated-pH treatment and live-cell imaging

IMCD-3 cells were transduced by lentiviral particles produced by co-transfection of HEK293T cells with lentiviral vector carrying the sequence for mScarlet-tubulin together with gag/pol and vsv-g vector (1:0.9:0.1). Medium containing lentiviral particles was collected 48 hours after transfection, filtered (0.45 µm pores), and used for transduction of IMCD-3 cells.

IMCD-3 cells expressing mScarlet tubulin were then transfected in OptiMEM media (Thermo Scientific) using Lipofectamine 2000 (Thermo Scientific) according to the manufacturer’s protocol. Cells were transfected in 8-well chambered coverslips (Ibidi), 0.5 µg DNA/well was used. Co-transfection of GFP-tau, Cdk5, and p25 was done in the ratio 1:0.85:0.15. The cells

were grown in DMEM/F12 supplemented by FBS and Penicillin/Streptomycin (Thermo Scientific). The imaging was done 24 hours after transfection.

Cells were imaged every 20 sec for 10 min. After 1 min of imaging, the media (DMEM/F12 supplemented by FBS and Penicillin/Streptomycin) was changed for the regular media with pH adjusted to 8.4 with NaOH. Imaging was performed using TIRF microscope (Apo TIRF 60x Oil DIC N2; 488+561 exposure: 300 ms) using OKO-lab chamber (37°C, 5% CO_2).

FRAP experiments

For FRAP experiments, the cells were prepared the same way as described in section 'Elevated-pH treatment and live-cell imaging'. A spinning-disk confocal microscope (Nikon CSU-W1) equiped with FRAP/photoactivation module was used to image and FRAP cells. Cells were imaged using CF Plan Apo VC 60XC WI objective (water immersion) and 488nm laser and FITC filter. Imaging was done on a single cell using 3 different settings: (1) the cell was imaged for 17 frames (100 ms exposure time, 500ms interval) before FRAP; (2) FRAP was performed on a circular region of 0.5 µm diameter; (3) the cell was imaged for 22 seconds directly after FRAP to visualize the recovery. The imaging was done at 37°C and 5% CO_2.

Cell cycle experiments

For the monitoring of tau during cell cycle, U-2 OS human cell line (ATCC HTB-96) was transfected with the GFP-tau vector using the X-tremeGENE HP reagent (Sigma Aldrich) and then selected with 200 µg/mL zeocin. GFP-positive cells were sorted by fluorescent-activated cell sorting (BD FACS Aria Fusion). Cells were then transduced with retroviral particles containing the mScarlet-tubulin. Briefly, Platinum A cells were transfected with pMXs-Puro-mScarletI-Tubulinα, particles were collected after 48 hours and applied to cells, which were selected with 2.5 µg/mL puromycin. The resulting GFP-tau/mScarlet-tubulin cell line was grown on glass-bottom dishes in Fluorobrite medium with 10% FBS and glutamine and observed on a confocal Zeiss LSM 880 microscope at 37°C and 5% CO_2.

Katanin experiment in cells – preparation

IMCD-3 cells were co-transfected with vectors for overexpression of mCherry-tau or mCherry, katanin subunit p60, katanin subunit p80-GFP, and Cdk5 and p25 or empty pCDNA3 vector (in the ratio: 1: 0.375: 0.375: 0.375: 0.375). 12 hours after transfection the cells were fixed using 4% PFA/PBS for 15 min followed by methanol at -20 °C for 2 min. Fixed cells were kept in PBS at 4 °C.

Katanin experiment in cells – immunostaining

Cells were blocked for 1 hour in 0.1% BSA/PBS and then stained with anti-β-tubulin antibody overnight (1:400; DSHB Hybridoma Product E7 deposited to the DSHB by Klymkowsky, M.[39]). After washing, cells were incubated with anti-mouse secondary antibody conjugated with Alexa-647 (Thermo Scientific). Cells were captured using a confocal microscope Leica Stellaris 8 (HC PL APO CS2 63x/1.40 OIL, WLL laser).

Live-cell image analysis

Tau lysate analysis. Microtubule lengths were measured by using the IRM signal, tau envelope lengths were measured by using the fluorescent tau signal after 3 min of incubation. The envelope coverage represents the sum of all tau envelopes lengths divided by the sum of all microtubule lengths within one field of view.

Coefficient of variation (CoV). To determine the CoV in the elevated-pH treatment experiments, a circle was drawn inside the cell, covering (most of) the area of the cell (in case of large cells, two circular areas were averaged). For monitoring GFP-tau during the cell cycle, whole cells were manually selected. The CoV was determined using ImageJ from the standard deviation of the tau fluorescent signal within the ROI, divided by the mean. In elevated-pH treatment experiment, coV was analyzed before, at t = 0 min and t = 9 min after elevated-pH treatment.

Microtubule CoV. The microtubule CoV was determined as the regular CoV, however, the ROI in this case was a line drawn on a single microtubule inside the cell. For every cell, 3 random microtubules were measured and the CoV was averaged.

Pearson's R. Cells in interphase or in mitosis were manually selected based on the presence or absence of a mitotic spindle, and Pearson's correlation coefficient between the GFP-tau and the mScarlet-tubulin channels was calculated with the Coloc 2 plug-in in ImageJ.

Tau density on microtubules. To show that the affinity of tau to the microtubule is different in different cell groups, the mean intensity of tau on the microtubule was measured before elevated-pH treatment and divided by the mean intensity of the same-size region in the cytoplasm next to the measured microtubule at the same timepoint. 25 cells were analyzed (average of 5 microtubules was used for each cell).

Mean intensity of tau in the cell. To show that the transfection of tau was comparable between the groups, the mean intensity of the GFP signal was measured in random circular regions of the cytoplasm before elevated-pH treatment.

Normalized tau density in patches. To show that the density of tau in patches is stable over time for the tau and tau-Cdk5 group, while the density of tau-ΔN is increasing, the intensity of tau in the patches at 5 different timepoints after elevated-pH treatment was analyzed. For tau-ΔN the intensity over the entire length of the microtubule was analyzed. The mean intensity in a tau positive region on the microtubule (tau patch or full microtubule) was measured and subtracted by the mean intensity of the same-size region next to the microtubule. All timepoints were normalized to the intensity of tau before the elevated-pH treatment. 10 cells were analyzed and at each timepoint the average tau density on 5 microtubules was used.

Normalized tau density in the cell. To quantify the recovery of tau signal, the mean density of tau signal on the microtubules was analyzed during the time course. The mean tau intensity in the cell (ROI comprising most of the cell) was measured at all time points and subtracted

by the intensity of the GFP signal in the cytoplasm next to the microtubules). The intensity in each time point was then normalized to the intensity before elevated-pH treatment. Both curves (control tau cells and tau-Cdk5 cells) were fitted using Matlab fitting tool using exponential recovery curve: f(x)= a-b*exp(-c*x) with exponential time constant 1/c [min].

FRAP analysis – recovery time constant. To analyze the recovery of the GFP signal on the microtubule after photobleaching, the intensity of the GFP signal in a small ROI on the microtubule in the bleached region of the cell was analyzed using ImageJ. The same-size region on the microtubule in the same cell but outside the bleached area was used as a reference (ref) and the same-size region outside the cell was used as a background (bg). 14-15 cells were analyzed. The curves were double-normalized according to the equation: $F_{frap\text{-}normalized}(t) = (F_{ref\text{-}pre}/[F_{ref}(t) - F_{bg}(t)])([F_{frap}(t) - F_{bg}(t)]/F_{frap\text{-}pre})$, where $F_{ref\text{-}pre} = \Sigma_{(t=0;t=17)} ([F_{ref}(t) - F_{bg}(t)]/f_{prebleach})$; $F_{frap\text{-}pre} = \Sigma_{(t=0;t=17)} ([F_{frap}(t) - F_{bg}(t)]/f_{prebleach})$; $f_{prebleach} = 17$; $F_{ref}(t)$ is the reference fluorescence intensity on the microtubule in the same cell but not in the bleached region; $F_{frap}(t)$ is the fluorescence intensity on the microtubule in the bleached ROI; $F_{bg}(t)$ is the fluorescence intensity in a background ROI outside the cells; $F_{ref\text{-}pre}$ is the mean fluorescence intensity of the reference ROI before the bleaching after background subtraction; $F_{frap\text{-}pre}$ is the mean fluorescence intensity of the bleached ROI before the bleaching after background subtraction. The normalized data was fitted using the Matlab fitting tool using the equation: $y = a*exp(-b*x)+c$; where b = rate constant and c = asymptote.

FRAP analysis – immobile fraction. To calculate the percentage of immobile fraction, we used the equation: Immob = $[1-(c-F_0)/(1-F_0)]*100$; where c is the asymptote (of the fitted curve), and F_0 is the normalized intensity immediately after the bleaching.

Katanin experiment – relative tubulin and katanin density. The mean density of stained tubulin signal in the transfected cell relative to the mean density of surrounding cells non-transfected with katanin was analyzed using ImageJ (average tubulin intensity of 3 circular ROIs in the cytoplasm of the transfected cell divided by the average tubulin intensity in 3 circular ROIs in 3 randomly selected cells in close vicinity to the analyzed cell). The relative tubulin density was either correlated to the relative density of the katanin signal (correlation plot with the linear regression) or plotted according to the experimental groups in a scatter plot (for this purpose only cells with relative intensity of katanin between 0.5-3 were plotted).

Mass Spectrometry

Samples were analyzed using a liquid chromatography system Agilent 1200 (Agilent Technologies) connected to the timsToF Pro PASEF mass spectrometer equipped with Captive spray (Bruker Daltonics). Mass spectrometer was operated in a positive data-dependent mode. Five microliters of peptide mixture were injected by autosampler on the C18 trap column (UHPLC Fully Porous Polar C18 2.1mm ID, Phenomenex). After 5 min of trapping at a flow rate of 20 µL/min, peptides were eluted from the trap column and separated on a C18 column (Luna Omega 3 µm Polar C18 100 Å, 150 x 0.3 mm, Phenomenex) by a linear 35 min water−acetonitrile gradient from 5% (v/v) to 35% (v/v) acetonitrile at a flow rate of 4 µL/min. The trap and analytical columns were both heated to 50°C. Parameters from the standard proteomics PASEF method were used to set timsTOF Pro. The target intensity per individual PASEF precursor was set to 6000, and the intensity threshold was set to 1500. The scan range

was set between 0.6 and 1.6 V s/ cm^2 with a ramp time of 100 ms. The number of PASEF MS/MS scans was 10. Precursor ions in the m/z range between 100 and 1700 with charge states ≥2+ and ≤6+ were selected for fragmentation. The active exclusion was enabled for 0.4 min. The raw data were processed by PeaksStudio 10.0 software (Bioinformatics Solutions, Canada). The search parameters were set as follows: enzyme – trypsin (specific), carbamidomethylation as a fixed modification, oxidation of methionine, phosphorylation (STY) and acetylation of protein N-terminus as variable modifications.

Mass spectrometry sample preparation

Tau samples. Tau with different levels of phosphorylation (phospho-tau, dephospho-tau, Bact-tau, Bact-tau-Cdk5) was prepared as stated above.

Spin down samples. 1µM phospho-tau (insect cell expressed) was diluted in Mass Spec buffer (50mM HEPES, 75mM KCl, 10 µM taxol, 10 mM dithiothreitol, 1 mM Mg-ATP) and added to taxol-stabilized microtubules to reach a final volume of 100 µl. Microtubules and tau were incubated for 10 min at room temp and centrifuged for 30 min at 18000 x g in a Microfuge 18 Centrifuge (Beckman Coulter). After centrifugation the supernatant was separated from the pellet and used as the sample indicated by the 'tau in solution'. The pellet was resuspended in a four-fold lower volume of Mass Spec buffer and centrifuged again to ensure a more homogeneous sample. After the second centrifugation, the supernatant was discarded and the pellet was resuspended in BRB80 and used as the sample indicated by the 'tau in envelopes'.

Mass Spectrometry analysis

Phosphorylation degree. For each phosphorylation site, all peptides were studied that include the specific site, phosphorylated or not. Each peptide is found with a relative intensity, that gives an indication of the density at which that peptide is detected in the sample. Each peptide can be found with the specific phosphorylation site phosphorylated or not. The sum of the relative intensities of the peptide in phosphorylated state was divided by the sum of the relative intensities of the peptide in non-phosphorylated state to obtain the phosphorylation degree of the phosphorylation site. Each tau sample was prepared as triplicates and each individual sample was analyzed separately, resulting in 3 individual phosphorylation degree values for each phosphorylation site. The graphs in the paper display the mean ± s.d. for each sample at each phosphorylation site, either plotted along the amino acid sequence of tau, or as individual phosphorylation sites.

Total relative intensity. For each phosphorylation site, all relative intensities at which the peptides covering the specific phosphorylation were summed up to get the total relative intensity.

Statistics and reproducibility

For representative plots and figures, whenever not specifically stated in the caption, all data was collected from at least three independent trials. All repeated independent experiments showed similar results and no data was excluded from the manuscript. Unless stated

otherwise, all data were analyzed manually using ImageJ (FIJI) or Matlab (R2020b). Graphs were created using Matlab R2020b and statistical analyses were performed using the same software. Major points on graphs represent data means and the error bars represent variation or associated estimates of uncertainty.

Data availability

Source data files for all figures and supplementary figures, are available with this manuscript.

Acknowledgements

We thank the members of the Lansky-Braun lab and Balastik lab for their feedback and helpful discussion and T. Šmídová and K. Konečná for their technical support. This work was supported by Czech Science Foundation grant 19–27477X to Z.L. and L.L., 21-24571S to R.W. and 23-07703S to M.Br., the project National Institute for Neurological Research (Programme EXCELES, ID LX22NPO5107) - Funded by the European Union - Next Generation EU, the Charles University Grant Agency (GAUK no. 373821 to V.S.), the project 'Grant Schemes at CU' (reg. no. CZ.02.2.69/0.0/0.0/19_073/0016935) to V.S. and V.D and by Czech Health Research Council grant no. NV18-04-00085 to M.Ba. We acknowledge the Imaging Methods Core Facility at BIOCEV, institution supported by the MEYS CR (LM2023050 Czech-BioImaging) for their support & assistance in this work, the CF Protein Production of CIISB, Instruct-CZ Centre, supported by MEYS CR (LM2023042) for protein production, CF Structural mass spectometry of CIISB, Instruct-CZ Centre, supported by MEYS CR (LM2018127) and European Regional Development Fund-Project „UP CIISB" (No. CZ.02.1.01/0.0/0.0/18_046/0015974) for mass spectometry sample analysis, the microscope facility of FGU, supported by MEYS CR (Large RI Project LM2018129 Czech-BioImaging) and ERDF (project No. CZ.02.1.01/0.0/0.0/18_046/0016045) and Vinicna Microscopy Core Facility co-financed by the Czech-BioImaging large RI project LM2023050 for their support and assistance in microscopy. Computational resources were supplied by the project "e-Infrastruktura CZ" (e-INFRA LM2018140) provided within the program Projects of Large Research, Development and Innovations Infrastructures.

Author contributions

The manuscript was conceptualized by M.Br., M.Ba., Z.L.; methods were developed by V.S., R.W., E. L., A.K., V.D.; TIRF in vitro experiments were performed by V.S., E. L., A.K.; tau lysate preparation and experiments were performed by R.W., E.L.; live-cell experiments were performed by R.W., V.D.; FRAP experiments were performed and optimized by V.S., R.W.; data were analyzed by V.S., R.W., E.L., A.K., V.D.; resources were provided by V.H., C.J.; the manuscript was written by V.S., M.Br., Z.L., with reviewing and editing by R.W., M.Ba.; visualization was done by V.S.; the project was supervised by L.L., M.Br., M.Ba., Z.L.; funding was acquired by V.S., R.W., V.D., L.L., M.Br., M.Ba., and Z.L.

Competing interests

The authors declare no competing interests.

Supplemental information

Supplementary movie captions

Movie 1 related to Fig. 1c: **1.5nM phospho-tau on taxol-stabilized microtubules.**

A time-lapse movie of 1.5 nM phospho-tau-GFP (magenta) added to surface-immobilized taxol-stabilized microtubules and imaged for 5 minutes.

Movie 2 related to Fig. 1c: **1.5nM dephospho-tau on taxol-stabilized microtubules.**

A time-lapse movie of 1.5 nM dephospho-tau-GFP (cyan) added to surface-immobilized taxol-stabilized microtubules and imaged for 5 minutes.

Movie 3 related to Fig. 1e: **10nM Bact-tau in presence of active Cdk5.**

A time-lapse movie of 10 nM Bact-tau-GFP (magenta) on surface-immobilized taxol-stabilized microtubules (black). Active Cdk5/p35 was added to the measurement chamber at t=0 min.

Movie 4 related to Fig. 1e: **10nM Bact-tau in presence of deactivated Cdk5.**

A time-lapse movie of 10 nM Bact-tau-GFP (cyan) on surface-immobilized taxol-stabilized microtubules (black). Deactivated Cdk5/p35 (control) was added to the measurement chamber at t=0 min.

Movie 5 related to Fig. 2g: **10nM Bact-tau removal in presence of active Cdk5.**

A time-lapse movie of 10 nM Bact-tau-GFP (magenta) on surface-immobilized taxol-stabilized microtubules (black). Bact-tau was removed from solution in presence of active Cdk5/p35.

Movie 6 related to Fig. 2g: **10nM Bact-tau removal in presence of deactivated Cdk5.**

A time-lapse movie of 10 nM Bact-tau-GFP (cyan) on surface-immobilized taxol-stabilized microtubules (black). Bact-tau was removed from solution in presence of deactivated Cdk5/p35.

Movie 7 related to Fig. 3a: **FRAP of tau-GFP (control) cell.**

A time-lapse movie showing an IMCD-3 cell overexpressing GFP-tau (control, cyan) on which FRAP is performed at t=0 min. GFP-tau signal was monitored for 10 seconds before FRAP and 20 seconds after FRAP.

Movie 8 related to Fig. 3a: **FRAP of tau-GFP-deltaN cell.**

A time-lapse movie showing an IMCD-3 cell overexpressing GFP-tau-ΔN (tau-ΔN) on which FRAP is performed at t=0 min. GFP-tau signal was monitored for 10 seconds before FRAP and 20 seconds after FRAP.

Movie 9 related to Fig. 3a: **FRAP of tau-GFP-Cdk5 cell.**

A time-lapse movie showing an IMCD-3 cell overexpressing GFP-tau-Cdk5/p25 (tau-Cdk5) on which FRAP is performed at t=0 min. GFP-tau signal was monitored for 10 seconds before FRAP and 20 seconds after FRAP.

Movie 10 related to Supplementary Fig. 3g (left): **pH treatment on tau (control) cell.**

A time-lapse movie showing an IMCD-3 cell overexpressing GFP-tau (control) on which elevated-pH treatment is performed at t=0 min. GFP-tau signal (left) and mScarlet-tubulin signal (right) were monitored for 10 minutes; 1 min before treatment and 9 minutes after treatment.

Movie 11 related to Supplementary Fig. 3g (middle): **pH treatment on tau-ΔN cell.**

A time-lapse movie showing an IMCD-3 cell overexpressing GFP-tau-ΔN (tau-ΔN) on which elevated-pH treatment is performed at t=0 min. GFP-tau signal (left) and mScarlet-tubulin signal (right) were monitored for 10 minutes; 1 min before treatment and 9 minutes after treatment.

Movie 12 related to Supplementary Fig. 3g (right): **pH treatment on tau-Cdk5 cell.**

A time-lapse movie showing an IMCD-3 cell overexpressing GFP-tau-Cdk5/p25 (tau-Cdk5) on which elevated-pH treatment is performed at t=0 min. GFP-tau signal (left) and mScarlet-tubulin signal (right) were monitored for 10 minutes; 1 min before treatment and 9 minutes after treatment.

Movie 13 related to Supplementary Fig. 4a (left): **Kinesin-1 molecules walking on microtubules in presence of phospho-tau envelopes.**

A time-lapse movie showing kinesin-1-GFP molecules (white) walking on taxol-stabilized microtubules partly covered by phospho-tau envelopes (magenta).

Movie 14 related to Supplementary Fig. 4a (right): **Kinesin-1 molecules walking on microtubules in presence of dephospho-tau envelopes.**

A time-lapse movie showing kinesin-1-GFP molecules (white) walking on taxol-stabilized microtubules partly covered by dephospho-tau envelopes (cyan).

Movie 15 related to Fig. 4a: **Katanin severing microtubules covered with phospho-tau envelopes.**

A time-lapse movie showing katanin-GFP (yellow) severing taxol-stabilized microtubules partly covered by phospho-tau envelopes (magenta).

Supplementary figures

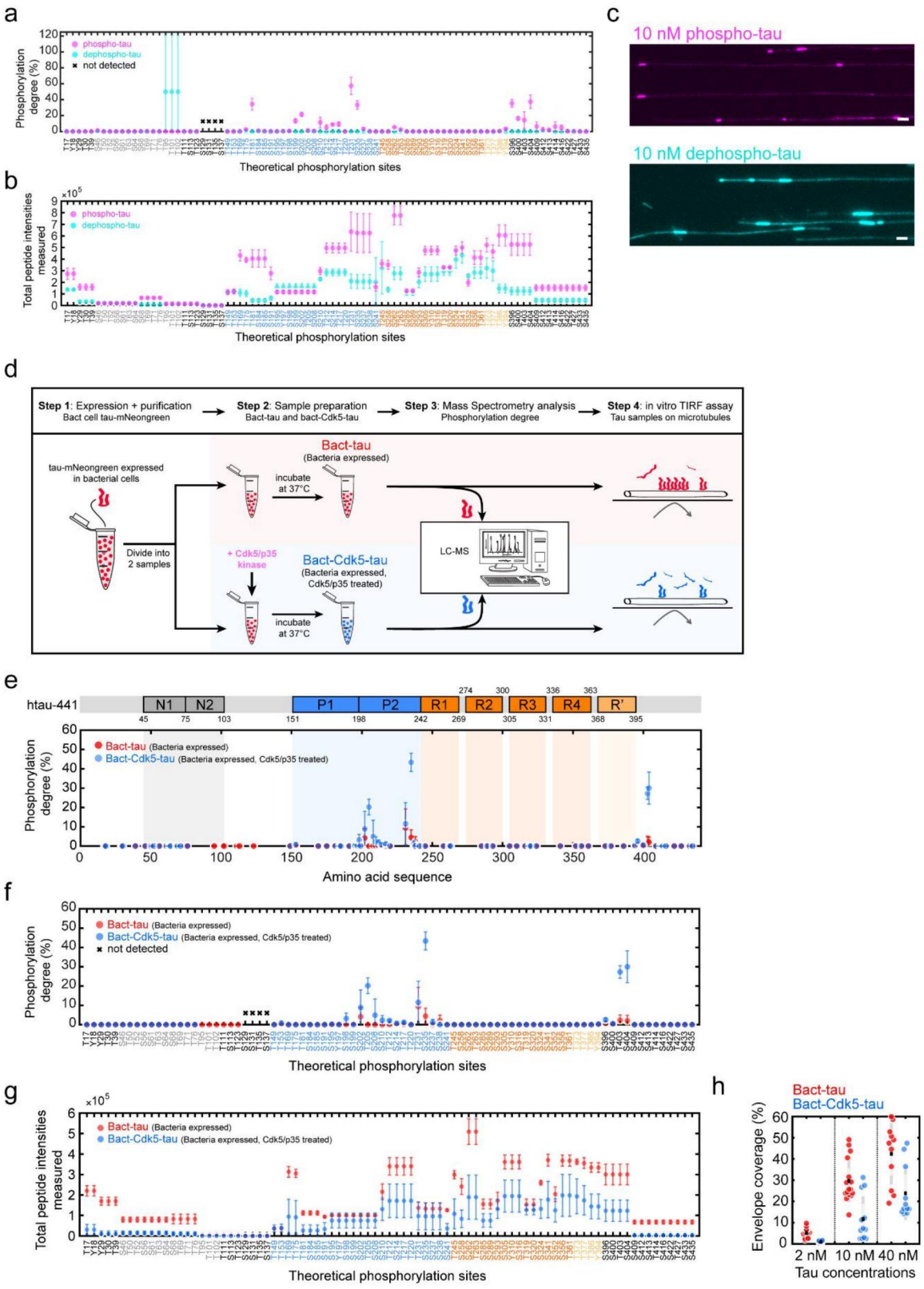

Supplementary Fig. 1: a. Mass-spectrometry-determined degree of phosphorylation of phospho-tau (magenta) and dephospho-tau (cyan). Phosphorylation degrees are presented as mean ± s.d. for each tau sample. If no peptides were detected that covered a specific

phosphorylation site, these phosphorylation sites are marked with a black cross. The color-coded legend corresponds to the domains along the tau sequence highlighted in Fig. 1b. **b**. Total relative intensities measured for all peptides covering the specific phosphorylation site, corresponding to data in a and Fig. 1b. Relative intensities are presented as mean ± s.d. for each tau sample. The color-coded legend corresponds to the domains along the tau sequence as shown in Fig. 1b. **c**. Fluorescence micrographs of 10 nM phospho-tau (left, phospho-tau in magenta) or 10 nM dephospho-tau (right, dephospho-tau in cyan) on surface-immobilized microtubules after 3 min of incubation. Scale bars: 2 μm. **d**. Schematics of sample preparation of bacterial expressed tau-mNeongreen (red), and Cdk5/p35-treated bacterial expressed tau-mNeongreen (blue). **e**. Mass-spectrometry-determined degree of phosphorylation of Bact-tau (red) and Bact-Cdk5-tau (blue). Phosphorylation degree is presented as mean ± s.d. and displayed at the location of the phosphorylation site along the amino acid sequence (schematic of the sequence is shown above the plot). The domains on the tau sequence are color-coded: N-terminal domains (N1, N2, grey), proline-rich domains (P1, P2, blue), microtubule-binding repeats (R1-R4, orange), and the domain pseudo-repeat (R', light orange). **f**. Mass-spectrometry-determined degree of phosphorylation of Bact-tau or Bact-Cdk5-tau for individual phosphorylation sites. Phosphorylation degree is presented as mean ± s.d. If no peptides were detected that covered a specific phosphorylation site, these phosphorylation sites are marked with a black cross. The color-coded legend corresponds to the domains along the tau sequence in Fig. 1e. **g**. Total relative intensities measured for all peptides covering the specific phosphorylation site, corresponding to data in e and f. Relative intensities are presented as mean ± s.d. The color-coded legend corresponds to the domains along the tau sequence as shown in Fig. 1e. **h**. Percentage of taxol-stabilized microtubules covered with a tau envelopes after 3 min incubation. Envelope coverage for Bact-tau was 5.1 ± 2.5% at 2 nM, 29.6 ± 10.1% at 10 nM, and 42.4 ± 14.4% at 40 nM (mean ± s.d., each data point represents a single field of view, n=12, 16, 11 independent experiments). Envelope coverage for Bact-Cdk5-tau was 0.9 ± 0.5% at 2nM, 11.7 ± 10.7% at 10nM, and 23.8 ± 12.6% at 40nM (mean ± s.d., each data point represents a single field of view, n=12, 12, 11 independent experiments).

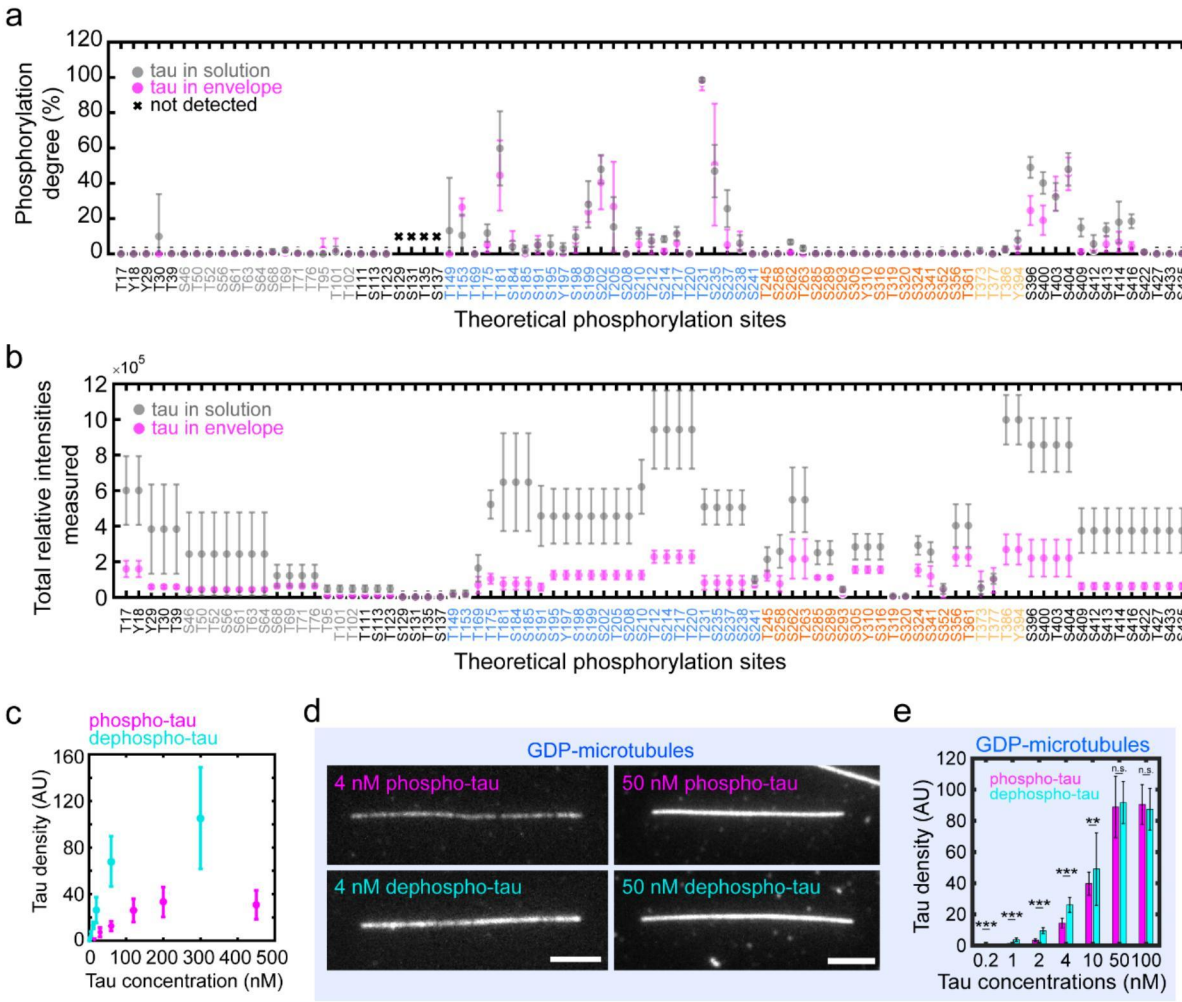

Supplementary Fig. 2: a. Mass-spectrometry-determined phosphorylation degree of spin down sample, where unbound tau was found in the supernatant (tau in solution, grey), and cooperatively bound tau found in the pellet (tau in envelope, magenta). Phosphorylation degrees are displayed as mean ± s.d. If no peptides were detected that covered a specific phosphorylation site, these phosphorylation sites are marked with a black cross. The color-coded legend corresponds to the domains along the tau sequence as shown in Fig. 2b. **b.** Total relative intensities of all peptides that covered the specific phosphorylation site, corresponding to data in a and Fig. 2b. Intensities are displayed as mean ± s.d. for unbound tau from the supernatant (tau in solution, grey), and cooperatively bound tau from the pellet (tau in envelope, magenta). The color-coded legend corresponds to the domains along the tau sequence as shown in Fig. 2b. **c**. Density of phospho-tau (magenta) or dephosho-tau (cyan) measured on GMPCPP microtubules as a function of the concentration of phospho-tau or dephosho-tau in solution (phospho-tau: n=12 fields of view in 4 independent experiments; dephospho-tau: n=9 fields of view in 3 independent experiments). **d.** Fluorescence micrographs of phospho-tau (magenta) or dephospho-tau (cyan) on glycerol-stabilized GDP-microtubules after 1 min of incubation. Scale bars: 2 µm. **e.** Concentration (nM) of phospho-tau (magenta) and dephospho-tau (cyan) plotted against the tau density (AU) on GDP-microtubules. For 0.2 nM: 0.07 ± 0.21 (phospho-tau) and 0.37 ± 0.20 (dephospho-tau) (mean ± s.d., n=36 microtubules in N=2 independent experiments, two-sided t-test: $p=1.31*10^{-8}$); 1

nM: 0.91 ± 0.36 (phospho-tau) and 3.75 ± 1.09 (dephospho-tau) (mean ± s.d., n=36 microtubules in N=2 independent experiments, two-sided t-test: $p=7.81*10^{-26}$); 2 nM: 3.43 ± 0.89 (phospho-tau) and 9.51 ± 1.92 (dephospho-tau) (mean ± s.d., n=36 microtubules in N=2 independent experiments, two-sided t-test: $p=2.53*10^{-33}$); 4 nM: 14.35 ± 3.10 (phospho-tau) and 26.12 ± 4.79 (dephospho-tau) (mean ± s.d., n=36 microtubules in N=2 independent experiments, two-sided t-test: $p=3.29*10^{-28}$); 10 nM: 39.71 ± 7.38 (phospho-tau) and 49.12 ± 23.25 (dephospho-tau) (mean ± s.d., n=51 and 57 microtubules respectively in N=3 independent experiments, two-sided t-test: p=0.0048); 50 nM: 88.88 ± 19.70 (phospho-tau) and 91.69 ± 13.45 (dephospho-tau) (mean ± s.d., n=45 and 44 microtubules respectively in N=3 independent experiments, two-sided t-test: p=0.3939); 100 nM: 90.43 ± 12.77 (phospho-tau) and 87.40 ± 13.38 (dephospho-tau) (mean ± s.d., n=20 and 30 microtubules respectively in N=1 independent experiment, two-sided t-test: p=0.4397).

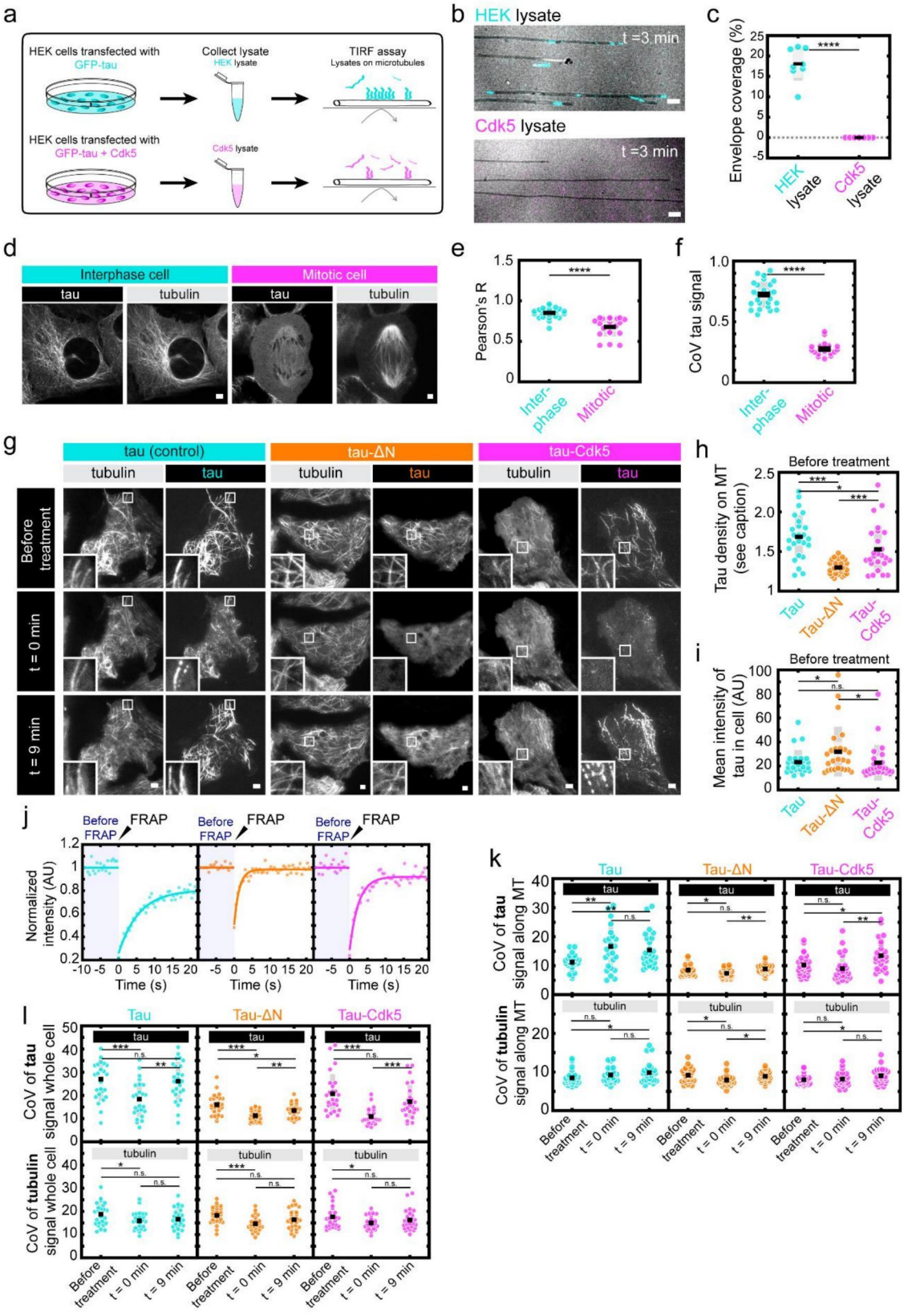

Supplementary Fig. 3: a. Schematics of preparation of lysates from HEK cells transfected with GFP-tau (HEK lysate, top, cyan) and of lysate prepared from HEK cells transfected with GFP-tau and Cdk5/p25 (Cdk5 lysate, bottom, magenta). **b**. Multichannel fluorescence micrographs of HEK lysate (top, cyan) and Cdk5 lysate (bottom, magenta) added to surface immobilized

taxol-stabilized microtubules (black) after 3 min of incubation. Scale bars: 2 µm. **c**. Percentage of taxol-stabilized microtubules covered by a tau envelope (envelope coverage) after addition of HEK lysate was 18.2 ± 3.4% (mean ± s.d., n = 8 fields of view in 8 independent experiments), and after addition of Cdk5 lysate was 0.0 ± 0.0% (mean ± s.d., n = 8 fields of view in 4 independent experiments). Two-sided t-test, $p=4.3821*10^{-10}$. **d**. Fluorescence micrographs of GFP-tau (left) and mScarlet-tubulin (right) in U-2 OS cells at different phases of the cell cycle. Cells in interphase (left panels, cyan) show higher binding of tau to microtubules compared to cells in mitosis (right panels, magenta). **e**. Pearson's R correlation coefficient between the GFP-tau and mScarlet-tubulin signal differs significantly between interphase and mitotic cells. Pearson's R in interphase cells was 0.85 ± 0.06 and in mitotic cells 0.68 ± 0.12 (mean ± s.d., interphase, n=25 cells in 3 independent experiments; mitosis, n=20 cells in 3 independent experiments). Two-sided t-test, $p=1.4224*10^{-7}$. **f**. Coefficient of variation (CoV) of the tau signal measured over the whole cell reflecting the difference between tau signal on microtubules and in cytoplasm. CoV of tau signal in interphase cells was 0.72 ± 0.11 and in mitotic cells 0.28 ± 0.06 (mean ± s.d., interphase n=25 cells in 3 independent experiments, mitosis n=19 cells in 3 independent experiments). Two-sided t-test, p=5.2528e-20. **g.** Fluorescence micrographs of cells before elevated-pH treatment (left), at t=0 min after elevated-pH treatment (middle) and t=9 min after elevated-pH treatment (right). 3 types of cells were subjected to elevated-pH treatment; control GFP-tau cells (tau, cyan), GFP-tau-ΔN cells (tau-ΔN, orange), and GFP-tau-Cdk5 cells (tau-Cdk5, magenta). Top panels represent the GFP-tau channel, bottom panels the mScarlet-tubulin channel. Scale bars: 10µm. **h.** Density of tau on microtubules before elevated-pH treatment, compared to density of tau in the cytoplasm, to give a measure of the binding affinity of tau in the different cells. Tau density on microtubules compared to cytoplasm in tau cells was 1.68 ± 0.28, in tau-ΔN cells was 1.30 ± 0.09, in tau-Cdk5 cells was 1.53 ± 0.30 (mean ± s.d., n=25 cells for each group in 4 independent experiments). Two-sided t-test p-values (left-to-right): $3.26*10^{-8}$, 0.0594, $5.89*10^{-4}$. **i.** Mean intensity of tau over the whole cell, as an indication of the expression level. Mean intensity over the wholle cell in tau cells was 23.2 ± 10.1, in tau-ΔN cells was 31.9 ± 20.8, and in tau-Cdk5 cells was 22.8 ± 14.7 (mean ± s.d., n=25 cells for each group in 4 independent experiments). Two-sided t-test p-values (left-to-right): 0.0658, 0.8901, 0.0774. **j**. Fluorescence recovery curves after FRAP for control GFP-tau cells (left, cyan); GFP-tau-ΔN cells (middle, orange); GFP-tau-Cdk5 cells (right, magenta). Normalized tau intensity within the FRAP area is plotted over time. The shaded blue area marks the period before FRAP, the black arrow indicates the timepoint at which FRAP occurred. **k.** Coefficient of variation of GFP-tau signal (top) or mScarlet-tubulin signal (bottom) measured along the microtubule lattice in GFP-tau (cyan), GFP-tau-ΔN (orange), and GFP-tau-Cdk5 cells (magenta). Coefficient of variation was measured at 3 timepoints: before elevated-pH treatment (left), at t=0 min after elevated-pH treatment (middle), and at t=9 min after elevated-pH treatment (right). **l.** Coefficient of variation of GFP-tau signal (top) or mScarlet-tubulin signal (bottom) measured over the whole cell in GFP-tau (cyan), GFP-tau-ΔN (orange), and GFP-tau-Cdk5 cells (magenta). Coefficient of variation was measured at three timepoints: before elevated-pH treatment (left), at t=0 min after elevated-pH treatment (middle), and t=9 min after elevated-pH treatment (right).

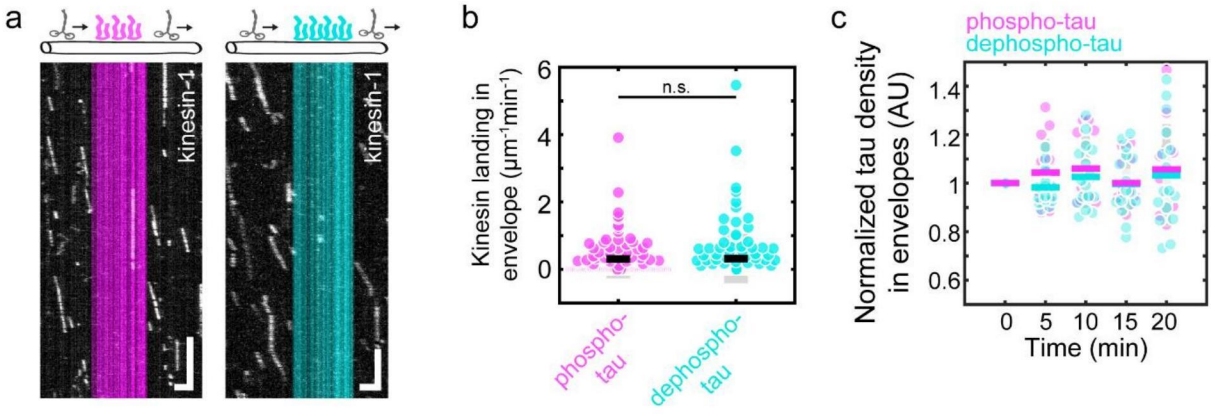

Supplementary Fig. 4: a. Fluorescence kymographs showing kinesin-1-GFP molecules (white) moving processively outside tau envelope region, independent of the phosphorylation degree of tau molecules forming the envelope (phospho-tau, left, magenta; dephospho-tau, right, cyan). Kinesin-1 landing but no processive movement was observed within the envelope boundaries. Scale bars: 2 µm, 1 s. **b**. Kinesin-1 landing rate within phospho-tau envelopes was 0.31 ± 0.58 $\mu m^{-1}min^{-1}$ and within dephospho-tau envelopes was 0.32 ± 0.73 $\mu m^{-1}min^{-1}$ (mean ± s.d., phospho-tau: n=100 envelopes in 5 experiments; dephospho-tau: n=125 envelopes in 5 experiments). Two-sided t-test, p=0.8894. **c**. Normalized tau density in envelopes after katanin addition for dephospho-tau was 0.98 ± 0.07, 1.02 ± 0.13, 1.00 ± 0.13, 1.03 ± 0.21 for 5, 10, 15, 20 minutes, respectively (mean ± s.d., n=16 envelopes in 2 individual experiments). Normalized tau density for phospho-tau was 1.04 ± 0.14, 1.06 ± 0.13, 1.00 ± 0.10, 1.06 ± 0.18 for 5, 10, 15, 20 minutes, respectively (mean ± s.d., n=13 envelopes in 4 individual experiments).

PUBLICATIONS UNRELATED TO THESIS
B

B.1 ANILLIN PROPELS MYOSIN-INDEPENDENT CONSTRICTION OF ACTIN RINGS

Kučera, O., **Siahaan, V.**, Janda, D., Dijkstra, S. H., Pilátová, E., Zatecka, E., Diez, S., Braun, M., Lansky, Z. Anillin propels myosin-independent constriction of actin rings. *Nat Commun* **12**, 4595 (2021).

Contributions as stated in the article:

Conceptualisation, M.B. and Z.L.; Methodology, O.K., M.B. and Z.L.; Investigation, O.K., V.S., D.J., S.H.D. and E.P.; Formal analysis, O.K., D.J., E.P. and V.S.; Data curation, O.K., D.J., V.S. and S.H.D.; Validation, O.K.; Resources, O.K., E.Z. and S.D.; Writing, O.K., M.B. and Z.L.; Visualisation, O.K.; Supervision, M.B. and Z.L.; Funding acquisition, M.B. and Z.L.

In detail: V.S. optimized and performed part of the TIRF experiments visualized in figure 1 (specifically figure 1k and all repetitions) and 4 (specifically data for figure 4h and all repetitions), and all experiments visualized in figure 3. All experiments done by V.S. were performed using TIRF microscopy. Additionally, part of the analysis for these experiments were done by V.S. using ImageJ and Excel.

nature COMMUNICATIONS

ARTICLE

https://doi.org/10.1038/s41467-021-24474-1 OPEN

Anillin propels myosin-independent constriction of actin rings

Ondřej Kučera[1,5], Valerie Siahaan[1], Daniel Janda[1], Sietske H. Dijkstra[1], Eliška Pilátová[1], Eva Zatecka[1], Stefan Diez[2,3,4], Marcus Braun[1✉] & Zdenek Lansky[1✉]

Constriction of the cytokinetic ring, a circular structure of actin filaments, is an essential step during cell division. Mechanical forces driving the constriction are attributed to myosin motor proteins, which slide actin filaments along each other. However, in multiple organisms, ring constriction has been reported to be myosin independent. How actin rings constrict in the absence of motor activity remains unclear. Here, we demonstrate that anillin, a nonmotor actin crosslinker, indispensable during cytokinesis, autonomously propels the contractility of actin bundles. Anillin generates contractile forces of tens of pico-Newtons to maximise the lengths of overlaps between bundled actin filaments. The contractility is enhanced by actin disassembly. When multiple actin filaments are arranged into a ring, this contractility leads to ring constriction. Our results indicate that passive actin crosslinkers can substitute for the activity of molecular motors to generate contractile forces in a variety of actin networks, including the cytokinetic ring.

[1] Institute of Biotechnology, Czech Academy of Sciences, BIOCEV, Vestec, Prague West, Czechia. [2] B CUBE – Center for Molecular Bioengineering, TU Dresden, Dresden, Germany. [3] Max Planck Institute of Molecular Cell Biology and Genetics, Dresden, Germany. [4] Cluster of Excellence Physics of Life, Technische Universität Dresden, Dresden, Germany. [5] Present address: CytoMorpho Lab, Laboratoire Physiologie Cellulaire & Végétale, Institut de recherche interdisciplinaire de Grenoble, Commissariat à l'énergie atomique et aux énergies alternatives (CEA), Grenoble, France. ✉email: marcus.braun@ibt.cas.cz; zdenek.lansky@ibt.cas.cz

Constriction of the cytokinetic actin contractile ring drives the division of most eukaryotic cells at the end of mitosis and meiosis[1,2]. The contractile ring is composed of bundles of actin filaments overlapping in mixed orientations, non-muscle myosin-II motors, crosslinking proteins and scaffolding proteins[3–5]. For a long time, it has been suggested that ring constriction is driven by myosin-propelled relative sliding of actin filaments, analogous to muscle sarcomere contraction[6,7]. Unlike muscle sarcomeres, however, the orientation of actin filaments forming the ring is disordered[8]. The sliding activity of myosin alone is thus equally likely to locally lead to contraction or extension, rendering this mechanisms insufficient to generate any net constriction of the ring[9]. Additional factors are therefore required to locally break the symmetry of the system in order to favour contractile forces[3,9–11]. Interestingly, phases of the cytokinetic ring constriction have been shown to be myosin-II-independent. For example in *C. elegans* embryos, constriction continues after conditional inactivation of myosin-II[12] or in *Drosophila* embryos a myosin-II-independent phase of the ring closure was identified during cleavage[13]. Moreover, multiple organisms lack myosin-II completely[14]. Theoretical and experimental works suggest that possible sources of the driving force underlying myosin-independent constriction mechanisms could depend on actin-crosslinking proteins and actin filament disassembly[15–21]. Direct experimental evidence, however, is scarce, leaving the myosin-independent mechanism of actin ring constriction unclear.

Here we show in a minimal reconstituted system that constriction of actin rings can be solely propelled by anillin, a non-motor actin crosslinking and scaffolding protein highly enriched in the contractile ring during cytokinesis[22–24]. Anillin, demonstrated to be required for the completion of cytokinesis in diverse organisms[25–29], is implicated in tumour growth and metastasis[30]. We found that anillin autonomously drives relative sliding of actin filaments and couples with actin filament disassembly to generate contractility. We thus demonstrate that diffusible filament crosslinkers, such as anillin, can generate contractile forces in actin networks, substituting for molecular motor activity.

Results

Anillin slides actin filaments to maximise their overlap. To study the interactions between anillin and actin filaments in vitro, we specifically immobilised sparsely rhodamine-labelled, phalloidin-stabilised actin filaments to the coverslip surface (Methods, Fig. 1a). After the addition of GFP-labelled anillin (Fig. 1b) to the experimental chamber, using TIRF microscopy, we observed anillin-GFP binding to actin filaments (Fig. 1c–e). At an anillin-GFP concentration of 0.12 nM, actin filaments were decorated by anillin-GFP molecules (Fig. 1a, f), which in accordance with previously published data[23,31] we identified as monomers (Fig. S1a). These single anillin-GFP molecules diffused along the actin filaments with a diffusion constant of $0.0088 \pm 0.0006\ \mu m^2 s^{-1}$ (linear fit coefficient ±95% confidence bounds, 268 molecules in two experiments) (Fig. S1b). When we increased the anillin-GFP concentration in solution to 12 nM and simultaneously added brightly rhodamine-labelled, phalloidin-stabilised actin filaments (mobile filaments), we observed mobile filaments landing from solution and length-wise crosslinking with the immobilised filaments forming filament bundles. In these bundles, we found mobile filaments moving diffusively along the immobilised filaments (Fig. 1g, h, Movie 1), showing that anillin-GFP generates a diffusible link between actin filaments. Strikingly, when a mobile filament landed such that it overlapped partially with the immobilised filament, we observed these mobile filaments moving unidirectionally along the immobilised filaments. Importantly, this movement was always in the direction increasing the length of the overlap between the two filaments and thus effectively contracting the elementary two-filament actin bundle (Fig. 1i, j, Movie 2). We performed this experiment also in an alternative way, not immobilising any of the filaments, but imaging the bundle formation in solution in the presence of 0.1% (w/v) methylcellulose to facilitate the imaging at a plane near the coverslip surface (Methods). Also, in this set of experiments, performed at 12 or 120 nM anillin concentrations, we observed, after initial formation of a partially overlapping two-filament bundle, relative directional sliding of the two crosslinked filaments increasing their overlap length (Fig. 1k, l, Fig. S1d, and Movie 3). The presence of anillin was required for the formation of the actin bundles and their directional sliding (Fig. S1e and Movie 4). In all experiments, we neither observed directional sliding of filaments that overlapped fully nor directional sliding decreasing the overlap length suggesting that the observed sliding is not due to residual traces of myosin motor protein in the anillin preparation (Supplementary Table 2, Methods). Blocking the motor ATPase activity by replacing ATP with the non-hydrolysable ATP analogue AMP-PNP (β,γ-Imidoadenosine 5′-triphosphate lithium salt hydrate) in presence of hexokinase did not affect the observed sliding of partially overlapping filaments in the presence of anillin-GFP (Fig. S1f, i, Methods), ruling out motor proteins as a possible source of the driving force. Furthermore, directional sliding (increasing the overlap length) did not depend on the relative orientation (structural polarity) of the bundled filaments (Fig. S1g, h), further excluding molecular motors as a source of the movements observed. We furthermore note that the presence of anillin-GFP in our experiments did not alter the length of the actin filaments (Fig. 1k, l and Fig. S1c), excluding filament dynamics as source of the movements observed. Analysing the dynamics of the sliding, we found that the overlap length started increasing immediately after the formation of the bundle. Concomitantly with the increase of the overlap length, the amount of the anillin-GFP in the overlap increased (Fig. S1j), indicating anillin-GFP binding into the newly forming overlap region. Interestingly, sliding slowed down as the overlap length and the amount of anillin in the overlap increased, leading to the overlap length reaching an equilibrium value (Fig. 1m, n and Fig. S1k, l). Combined, these data demonstrate that anillin drives directional sliding of actin filaments relative to each other, increasing the length of the overlap between the filaments and, thus, contracting the filament bundle.

Anillin generates tens of pico-Newton forces to slide actin filaments. To directly measure the forces generated by anillin in the actin bundles, we specifically attached actin filaments to two microspheres (Methods). Holding the microspheres by two traps in an optical tweezers setup, we formed a crosslinked actin bundle consisting on average of about five filaments (4.7 ± 1.3, mean ± s.d., $n = 35$ bundles, Methods) in the presence of 12 nM anillin-GFP in solution, (Fig. 2a, b, Methods, and Fig. S2a). After ~5 min, when the system reached equilibrium, we started moving the microspheres apart from each other in 100 nm steps, stretching the bundle and thus sliding the filaments within the bundle in the direction of shortening their overlaps (Fig. 2b). Simultaneously with each step-movement of the trap (each step taking ~33 µs), we observed a rapid increase in force, which then decayed within several seconds to a plateau reflecting the equilibrium between the anillin-generated force, exerted in the direction of increasing the lengths of the overlaps between the filaments in the bundle, and the external load exerted by the optical trap in the opposite direction (Fig. 2c, d, see Fig. S2b for control experiment). Since the median time constant of the force decay (1.06 s, quartiles

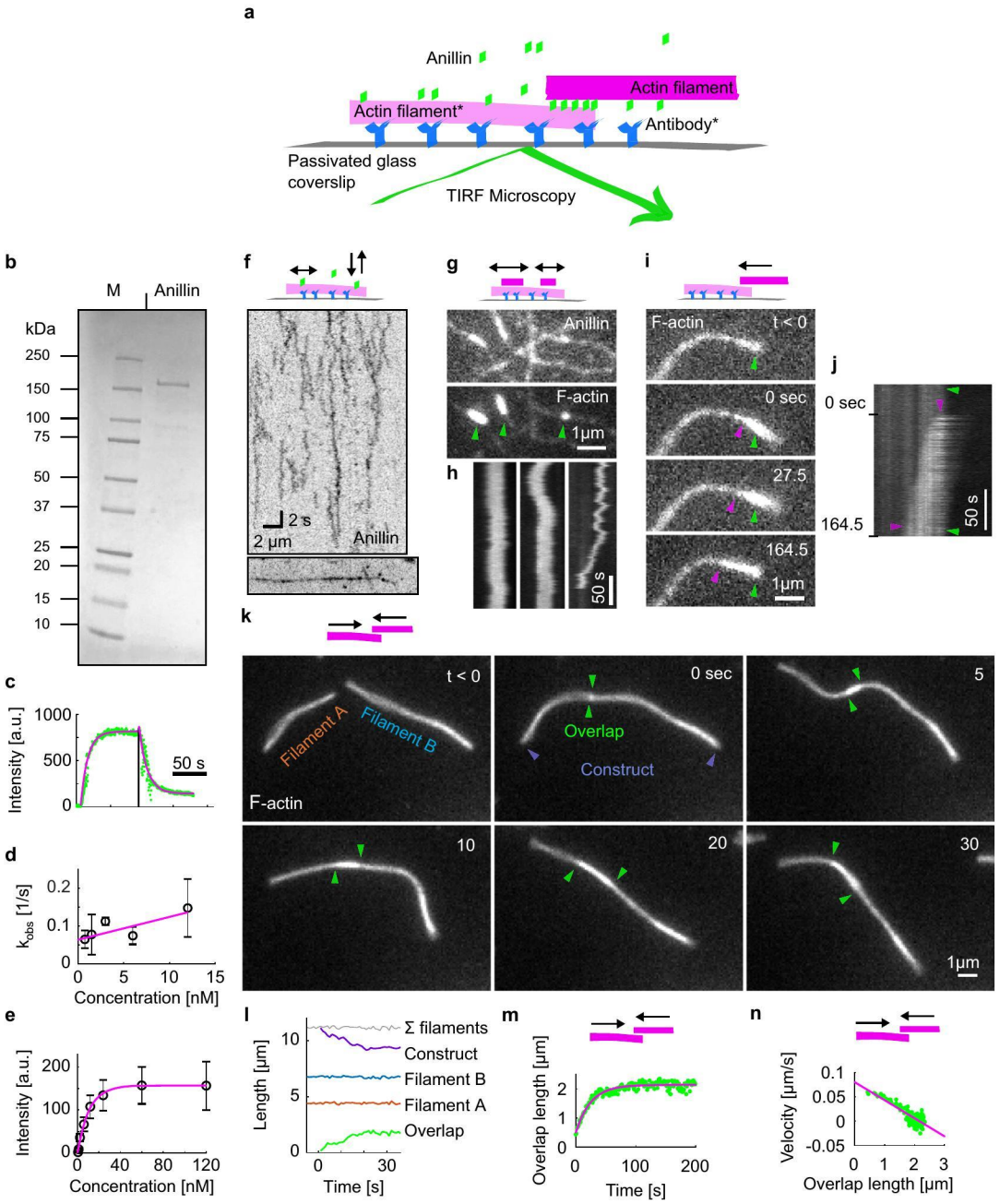

0.47 s and 2.00 s, $n = 326$ steps in 43 experiments) together with the trap movement was an order of magnitude faster than the rate of anillin unbinding from actin (Fig. 1d, Methods), we interpret this dynamic response being due to the rearrangement of anillin molecules in the overlap. The equilibrium force values increased with increasing distance between the two microspheres and thus with decreasing the overlap lengths between the filaments in the bundle ($n = 326$ steps in 43 experiments, Fig. 2c, e). On the timescale of the experiment, the decrease in the lengths of the overlaps resulted in an increase in the density of anillin-GFP in the overlaps (Fig. 2e, inset). The equilibrium force values reached up to tens of pico-Newtons before dropping suddenly, presumably when an actin filament slid apart completely from the rest of the bundle (Fig. S2c, d). When we (before the filament slid apart completely, in a situation when the bundle was pre-stretched) decreased the external load on the bundle by moving the microspheres closer together in steps of 100 nm, we immediately observed a decrease of the force, highlighting the reversibility of the process (Fig. 2d). We thus conclude that at constant anillin concentration, anillin molecules crosslinking actin filaments can autonomously generate substantial forces, which increase with decreasing lengths of the overlaps between the filaments and thus with increasing density of anillin crosslinkers in the overlap.

To test how the generated force depends on changes in the anillin concentration, we used the setup described above with an actin-anillin bundle suspended between two microspheres. We first pre-stretched the actin-anillin bundle by moving the microspheres apart such that the force readout was nonzero, and then we decreased the concentration of anillin-GFP in solution from 12 to 1 nM while keeping the distance between the microspheres constant (Methods). We then observed the force generated by anillin decreasing over time, presumably as

Fig. 1 Anillin slides actin filaments to maximise their overlap. a Schematic representation of the experimental setup. The asterisk denotes components used only in experiments with immobilised filaments. **b** SDS gel of anillin-GFP used in this study. This experiment was repeated three times with similar results. **c**, Kinetics of the anillin-GFP binding/unbinding to/from actin filaments. A temporal profile of the fluorescence signal of the anillin-GFP along an actin filament shows a typical first-order growth upon addition of 6 nM anillin-GFP and first-order decay after the washout. The loading experiment was repeated 15 times (three experiments) with similar result. **d** Concentration profile of the observed kinetics of anillin-GFP binding. The linear fit to the mean values ($R^2 = 0.64$) was used to estimate the unbinding rate of anillin from actin filaments, $k_{off} = 0.06\ s^{-1}$, 95% confidence interval 0.03–0.10 s^{-1} ($n = 15$ measurements in three experiments). Error bars represent mean ± s.d. **e** Concentration profile of the steady-state density of anillin-GFP on actin filaments (right). Michaelis–Menten fit to the mean values ($R^2 = 0.98$) was used to estimate the dissociation constant, $K_d = 7.82$ nM, 95% confidence interval 5.53–10.11 ($n = 12$–36 measurements per concentration in three experiments). Error bars represent mean ± s.d. **f** Intensity-inverted kymograph showing single anillin-GFP molecules diffusing along an actin filament (filament shown below the kymograph). **g** Fluorescence micrographs showing three short mobile actin filaments (indicated by green arrowheads) crosslinked by anillin-GFP to long, sparsely fluorescently labelled, and immobilised actin filaments (see Movie 1). **h** Kymographs show the diffusion of the mobile actin filaments from the micrograph in **g** along the immobilised filaments (see Movie 1). **i** Time-lapse micrographs and a kymograph, **j**, showing anillin-driven sliding of a mobile actin filament (bright) along an immobilised filament (dim), increasing the overlap between the two actin filaments (see Movie 2). Green and magenta arrowheads indicate the ends of the immobilised and mobile filaments, respectively. This experiment was repeated five times (eight events observed) with similar results. **k** Time-lapse micrographs showing anillin-driven sliding of two mobile actin filaments along each other, increasing the overlap between the two actin filaments (see Movie 3). Arrowheads indicate the ends of the filaments. This experiment was repeated 15 times (24 events observed) with similar results. **l** Time-traces of the lengths of the two filaments, the length of the overlap and the length of the bundle construct shown in the micrographs in **k**. The bundle contracts as the overlap length increases, while the lengths of the two filaments are constant. **m** A typical time trace of the overlap expansion (green dots) reaching an equilibrium value (magenta line represents an exponential fit (Methods) to the data). **n** Velocity of the overlap expansion decreases with increasing overlap length. Green points represent an exemplary event, magenta line is a linear fit to the data.

anillin-GFP was unbinding from the overlap (Fig. 2f and see Fig. S2f for control experiment). Conversely, increasing the anillin-GFP concentration in the measurement chamber from 1 to 12 nM while keeping the distance between the microspheres constant resulted in a gradual increase in the anillin-generated force, presumably due to anillin-GFP binding into the overlap (Fig. 2g and Fig. S2g).

Combined these experiments show that at constant anillin concentration, anillin molecules in the overlap generate force, which is inversely proportional to the length of the overlap between the filaments and thus proportional to the density of anillin crosslinkers in the overlap. Additional increase or decrease in the concentration of anillin results in an additional increase or decrease of the generated force, respectively. Importantly, these forces are always directed such that they increase the overlap lengths between actin filaments in the bundle and, consequently, result in the contraction of the filament bundle.

Anillin couples with actin disassembly to generate directed filament sliding. As actin depolymerisation is an important factor for the constriction of the cytokinetic ring, we wondered how depolymerisation of actin filaments will affect the observed anillin-driven filament sliding. We employed the experimental setup described in Fig. 1, using a mixture of Atto647-labelled, phalloidin-stabilised actin filaments and rhodamine-labelled non-stabilised actin filaments in the presence of 12 nM anillin-GFP and not immobilising any of the filaments. To enhance the disassembly of the non-stabilised filaments, we used 80–200 nM latrunculin A[32] leading to the non-stabilised actin filaments disassembling at a rate of 1.2 ± 1.1 monomer/s, (mean ± s.d., $n = 13$). Similar to the experiment in Fig. 1, we observed anillin-dependent crosslinking of the filaments leading to the formation of actin bundles, which contracted over time. Strikingly, however, in this experiment, we did not observe only sliding of partially overlapping filaments as described above, but we also observed sliding of filaments that overlapped fully. This sliding was observed when the retreating tip of a disassembling non-stabilised actin filament reached the end of a stabilised filament crosslinked to the disassembling filament by anillin (Fig. S3 and Movie 5). The stabilised filament then followed the retreating tip of the non-stabilised actin filament (Fig. 3a, b and Movies 6, 7) such that the velocity of its sliding matched the rate of filament disassembly (correlation coefficient 0.90 ± 0.06, mean ± s.d., $n = 13$ events in nine experiments) (Fig. 3c–e). Consequently, full overlaps were maintained between the stabilised filaments and the disassembling filaments to which they were crosslinked (Fig. 3a, b and Fig. S3). We hypothesise that as the disassembly of one of the filaments transiently shortens the overlap length, the concurrent anillin-driven sliding described in the experiments presented in Fig. 1 compensates this shortening, maintaining the overlap length. This process, leading to the sliding of actin filaments along with the tip of a depolymerising filament, is thus an efficient mechanism that converts actin filament depolymerisation into sliding-driven contraction of actin bundles.

Anillin promotes the formation of actin rings and drives their constriction. To study the anillin-driven sliding of actin filaments in networks of higher complexity, we increased the actin filament density in solution, while not immobilising any of the filaments. Initially, we used non-stabilised actin filaments. We found that anillin, similar as septins[33], promotes the formation of actin-filament rings with several micrometres in diameter (Fig. 4a, b and Fig. S4a, b, Methods). We note that further increasing the density of actin filaments in solution resulted in a formation of dense actin networks (Fig. S5). The rings, which we observed throughout the volume of the microscopy chamber, typically consisted of three to eight actin filaments colocalising with anillin-GFP (Methods). Importantly, time-lapse imaging of these rings revealed that they constrict over time (Fig. 4b–d and Movie 8). The circumference of the rings decreased asymptotically (Fig. 4c–e), enabling us to quantify the circumference of the maximally constricted ring. The constriction varied substantially, with constriction after 300 s reaching up to 20% of the initial circumference, maximum asymptotical constriction reaching 100 % and the maximum constriction rate reaching 0.034 μm s^{-1} (Fig. 4f, h and Fig. S4c). The spread in the data likely reflects the spread in the initial lengths of the overlaps between the filaments forming the rings, as well as the spread in the number of these filaments. While most of the rings ($n = 18$, out of total 26 rings in 16 experiments) constricted during the time of the experiment, in some cases ($n = 8$), we did not observe any significant constriction. We interpret these as rings that already reached their maximum constriction before the beginning of our observation. To test the contribution of actin disassembly in the constriction process, we additionally studied the constriction

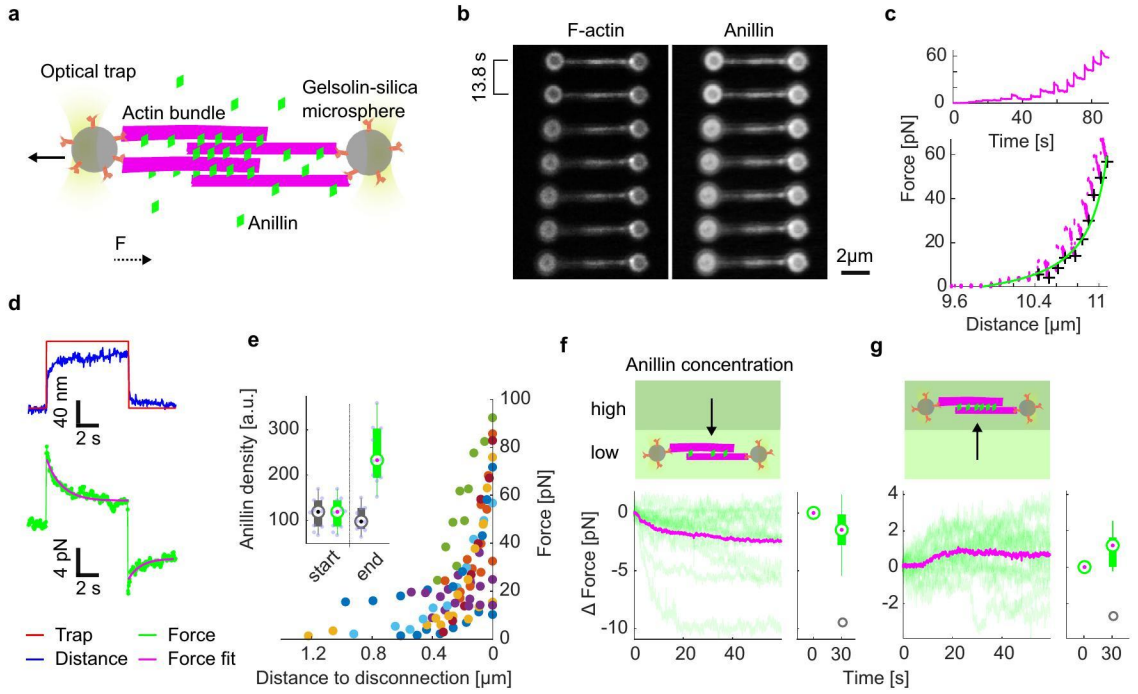

Fig. 2 Anillin generates tens of pico-Newton forces to slide actin filaments. a Schematic representation of the experimental setup. **b** Time-lapse fluorescence micrographs showing an actin bundle attached between two silica microspheres. The bundle is being stretched as the left microsphere is pulled leftwards by an optical trap. **c** Typical force time-trace (top) and the force-distance curve (bottom) corresponding to stretching of an anillin-actin filament bundle (experimental data points—magenta). Asymptotic forces of individual stretching steps, calculated by fitting an exponential to the force decays (as shown in **d**), are indicated by black crosses. These increase hyperbolically with increasing distance between the microspheres, and thus with decreasing overlap length L. The green line represents ~$1/L$ fit to the data. **d** Temporal response of the construct to stretching and relaxation; the left optical trap is moved 100 nm away from the right trap and then, after ~7 s, moved back to the original position. The temporal profile of the longitudinal position of the left optical trap is shown together with the detected distance between the microspheres (top) and the detected force (bottom). **e** The detected force increased with decreasing overlap length before the filaments slid apart completely (distance to disconnection = 0). All events longer than six steps are plotted ($n = 11$ experiments indicated by different colours). Inset, anillin density in the overlap (fluorescence intensity of anillin per unit length of the overlap) at the start and the end of the bundle stretching. Grey boxplots represent raw data, green boxplots represent data after photobleaching correction (see Fig. S2e for the photobleaching estimation) ($n = 10$ experiments). Corresponding data points overlay the boxplots. **f**, **g** Force response of a pre-stretched actin-anillin bundle to a decrease (**f**) or increase (**g**) of anillin-GFP concentration. Schematic representation of the experiment (top) and temporal experimental data (bottom). Decrease of the concentration ($n = 15$ events in 14 experiments), increase of the concentration ($n = 15$ events in 14 experiments). Green curves are the experimental data, mean temporal profile is shown in magenta. Box and whisker plots show a significant decrease or increase in force between time points 0 and 30 s after a decrease (one-sided Wilcoxon test, $p = 0.02$) or increase (one-sided Wilcoxon test, $p = 0.03$) of anillin-GFP concentration. In **e**-**g** data were represented as boxplots. Central marks represent median, top and bottom edges of the box indicate the 75th and 25th percentiles, respectively. Whiskers extend the most extreme points that are not considered outliers. Outliers are marked as grey circles.

dynamics of anillin-actin rings consisting of filaments stabilised by rhodamine-phalloidin. We found that the constriction was significantly slower ($P = 0.0044$), with constriction after 300 s of up to about 5% of the initial circumference and maximum constriction rate of 0.006 μm s^{-1} (Fig. 4f–h, $n = 12$ rings in ten experiments). However, the maximum asymptotical constriction reached 100%, similarly to the rings formed by disassembling actin filaments. Consistently, the addition of latrunculin to rings of non-stabilised actin filaments led to higher asymptotic constriction (Fig. 4g, h). These results are in agreement with our data on linear bundles, where we observed that depolymerisation of actin filaments promotes the contraction of the bundle. Combined these experiments show that rings of actin filaments can constrict without the action of nucleotide hydrolysing molecular motors, solely driven by forces generated by passive actin crosslinkers. This constriction is enhanced by actin-filament disassembly.

Discussion

We here show that the passive, non-motor, actin crosslinker anillin can drive the contraction of actin bundles through directed filament sliding. Depletion interactions[34–37] did not contribute to this phenomenon, as filaments did neither bundle nor slide in the absence of anillin in our control experiments (Fig. S1e). Actin filaments were sliding also in the absence of ATP, ruling out the remnants of myosin in our anillin-GFP preparation as the possible sources of sliding. Importantly, we observed only sliding of partially overlapping filaments and the sliding was always directed such that the length of the overlap between the filaments increased; both findings ruling out molecular motors as possible source of the movement. Anillin diffuses along actin filaments (Fig. 1f), creating a diffusible link between actin filaments (Fig. 1g, h), and is retained in overlaps that transiently shorten (Fig. 2e, inset), suggesting that anillin molecules in the overlaps can be described as particles of an ideal gas confined in the overlap, analogous to diffusible crosslinkers in microtubule systems[38,39]. We observed that the anillin-generated force is inversely proportional to the overlap length (Fig. 2c, e) and, considering that anillin unbinding on the experimental timescale was negligible, thus proportional to the density of anillin in the overlap, as expected for an ideal gas[38]. Increasing or decreasing the concentration of anillin in our trapping experiment while keeping the distance between the traps constant, resulted in an increase or

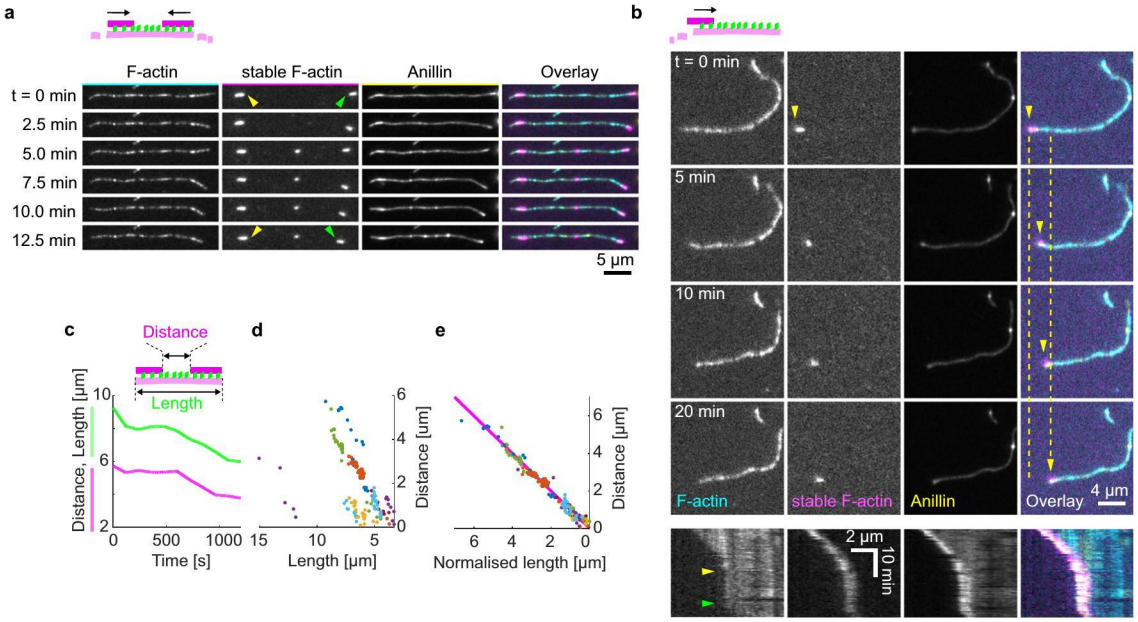

Fig. 3 Anillin couples with actin disassembly to generate directed filament sliding. a Fluorescence time-lapse micrographs showing two short phalloidin-stabilised actin filaments sliding along with the retreating ends of a non-stabilised disassembling actin filament (see Movie 6). Arrowheads indicate the inner ends of the two stabilised actin filaments coming closer to each other. **b** Fluorescence time-lapse micrographs showing one short phalloidin-stabilised actin filament sliding along with the retreating end of a non-stabilised disassembling actin filament. Below, multicolour fluorescence kymograph of the event, showing that transient pauses in the disassembly (beginning and end of the pause indicated by yellow and green arrowheads) result in transient pauses in the filament sliding (see Movie 7). **c** Typical time-traces of the length of the non-stabilised actin filament (green) and the distance between the two short stabilised filaments (magenta) moving with the ends of the non-stabilised actin filament. **d**,**e** The distance between the stabilised actin filaments decreases linearly with the length of the disassembling actin filament ($n = 12$ events in nine experiments, colours denote individual events).

decrease of the anillin-generated force, respectively. Using the analogy of the ideal gas, we interpret this observation as an increase or decrease in the anillin 'pressure' in the overlap after increasing or decreasing the number of particles in a constant volume. Combined, our results thus suggest that the anillin-generated force is of an entropic origin[40] (Fig. 5a). The ability of monomeric anillin (Fig. S1a) to bundle actin filaments (Fig. 1), and to generate entropic force in partially overlapping actin bundles (Fig. 2), apparently originates from its possession of multiple actin-binding sites[41], highlighting the importance of multivalency for the process[42]. An additional force component is likely associated with energetically favourable binding of the anillin crosslinkers into the overlap. At anillin concentrations of 12 nM used in this study, anillin molecules, collectively, can generate forces in the order of 10 pN in a bundle of about five filaments. These forces are comparable to forces generated by myosins; single Myosin-II stall force is about 2 pN[43,44], suggesting that anillin crosslinkers can generate forces relevant in the context of the cytokinetic ring.

Motion of filament-associated proteins along the surface of cytoskeletal filaments induces frictional forces[45]. During the relative sliding of actin filaments, anillin molecules have to collectively reorganise within the overlap, likely moving along the surfaces of the two filaments, which will thus result in the generation of frictional forces acting against the forces driving the movement. Frictional forces increase with the increasing number of crosslinkers coupling the two filaments, and with the crosslinker density[38,39,46–48]. The generation of friction can thus explain the observed slowdown in filament sliding concomitant with the increase of anillin molecules in the overlap when the overlap length increases (Fig. 1m, n). Similarly, friction will likely play a role in the observed slowdown of the ring constriction (Fig. 3c–f). Circular constraints within the ring may also contribute to the deceleration of the constriction as the decrease of the diameter of the ring requires stronger bending of its constituting filaments[33,37,49]. Dependent on the crosslinker stiffness and their interaction potential, the crosslinker induced friction generated between sliding filaments can exhibit highly non-linear scaling with the crosslinker number and density[46]. As the entropic force driving the contraction scales linearly with the crosslinker density, friction might become prohibitive at high anillin concentrations. Although we could not test the mechanism at elevated anillin concentrations due to technical reasons, these considerations suggest the existence of an anillin concentration optimal for the constriction. While below this concentration the bundling of the filaments would be inefficient, and the contractile forces low, above this concentration the frictional forces might become prohibitive and the filament sliding would stall. This notion is in accordance with in vivo observations showing that intermediate levels of anillin enable maximum speed of contraction of the cytokinetic ring in *C. elegans* zygote[17].

Anillin is required for the ingression of the cytokinetic furrow and the completion of cytokinesis[26,29,50]. Depletion of anillin leads to slowdown of the ingression and cytokinesis failure[27,28]. In this context anillin is thought of mostly as a scaffolding element and a regulator of myosin-driven contractility. However, our experiments show that anillin is an autonomous generator of contractile forces. Furthermore, actin filament depolymerisation in various, albeit not all, organisms[51] plays an important role during the constriction of the cytokinetic ring. Blocking actin depolymerisation, e.g. with drugs or by impairing the actin-depolymerising and severing enzyme cofilin, leads to defective ring constriction[21,52–54]. Moreover, decreased levels of cofilin or anillin resulted in similar effect in *Drosophila* embryos, namely a delayed switch to the myosin-independent phase of the constriction[13], suggesting that actin filament depolymerisation, in concert with anillin might drive myosin-independent constriction of the cytokinetic ring. We here provide direct evidence that anillin crosslinkers efficiently couple

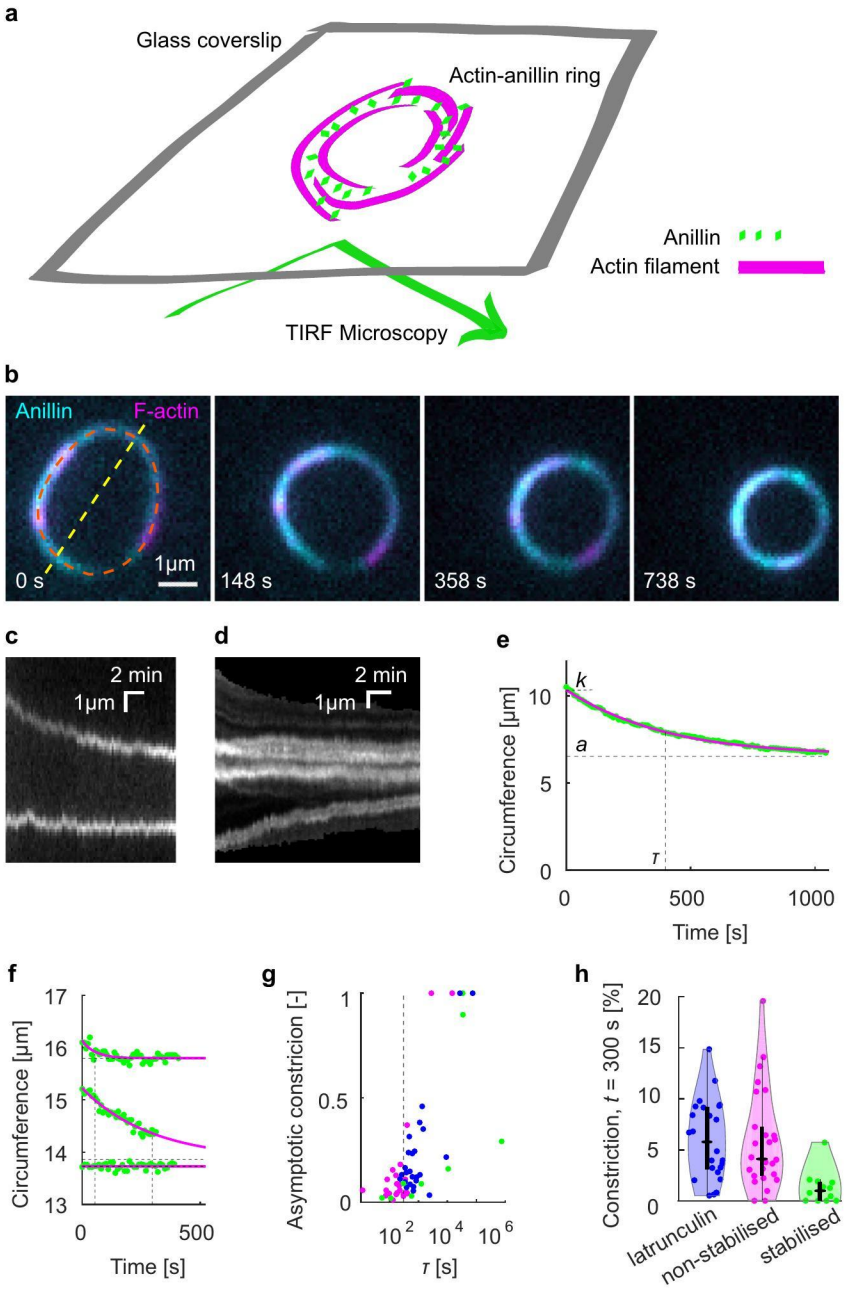

Fig. 4 Anillin promotes the formation of actin rings and drives their constriction. a Schematic representation of the assay geometry. **b** Multicolour time-lapse micrographs of the anillin-actin ring, showing the ring constriction over time (see Movie 8). **c** Kymograph along the yellow dashed line (diameter) in **b** of the constricting anillin-actin ring. **d** Kymograph along the orange dashed line (circumference) in **b** of the constricting anillin-actin ring showing the relative sliding of fluorescently sparsely labelled (speckled) filaments, which form the ring. Relative sliding is visualised by the relative motion of fluorescent speckles. **e** Time trace of the circumference of the ring shown in **b**. Green dots represent experimental data and the solid magenta curve an exponential fit. Dashed lines indicate the fit parameters (τ time constant, k initial circumference, a asymptotical circumference). **f** Exemplary time-traces of fast (top), slow (centre) and not (bottom) constricting rings. Identical graphical representation as in **e**. See Fig. S4c for the time traces of all events. **g** Relation between the time constant and the relative asymptotic constriction ($1 - (a/k)$). Each dot represents one ring formed either by non-stabilised (magenta, $n = 26$ in 16 experiments) or stabilised (green, $n = 12$ in 10 experiments) actin filaments, or non-stabilised actin filaments in the presence of latrunculin (blue, $n = 25$ in 7 experiments). Fits leading to asymptotical constriction higher than 1 were cut off to 1 ($n = 5$). Events with higher time constants than 10^6 s, all having zero asymptotic constriction, are not shown ($n = 5$). $\tau = 300$ s is highlighted by vertical dashed line. **h** Percentage of the constriction at $t = 300$ s for all observed rings of stabilised and non-stabilised actin filaments, or non-stabilised actin filaments in the presence of latrunculin ($n = 63$). Individual data points are accompanied by violin plots, and black boxplots: Central marks represent median, top and bottom edges of the box indicate the 75th and 25th percentiles, respectively. Whiskers extend the 95% confidence intervals.

with actin filament disassembly to generate contractile forces (Fig. 5b, c). This mechanism is reminiscent of the experimentally observed mechanism driving chromosome movement during the anaphase of cell division by coupling the chromosomes' kinetochores to depolymerising microtubule ends by biased diffusion[55–57] as proposed earlier theoretically[58]. Analogously, the diffusion of anillin is likely biased away from depolymerising actin filament ends, resulting in directional sliding of crosslinked filaments with the depolymerising end. We hypothesise that severing of actin filaments might promote this process, by increasing the

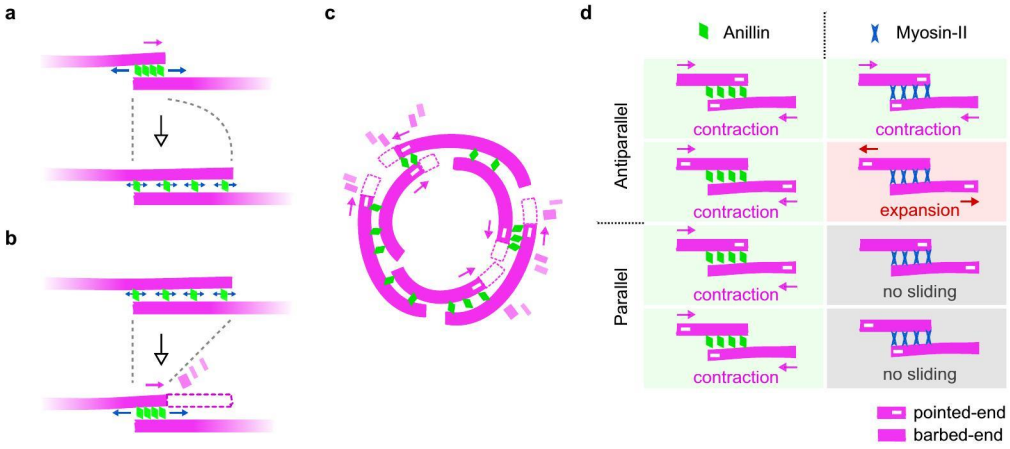

Fig. 5 Mechanism and properties of anillin-driven actin contractility. a Entropic expansion of anillin molecules confined between two partially overlapping actin filaments leads to filament sliding which maximises the length of the overlap and contracts the bundle (top). Sliding ceases when the entropic forces come to an equilibrium with forces opposing the sliding, such as frictional forces between the filaments (bottom). **b** Filament disassembly (for clarity, only one filament is shown to disassemble) transiently shortens the overlap, resulting in further sliding through entropic anillin expansion, again maximising the overlap length. **c** When actin filaments are organised in a ring geometry with mixed actin-filament polarities, anillin-propelled contraction of actin bundles will lead to ring constriction. **d** Comparison of actin contractility driven by diffusible crosslinkers such as anillin (left column) and molecular motors such as myosin (right column). While the entropic expansion of the crosslinkers in the overlap always leads to contraction, irrespective of the relative orientation of the actin filaments (filament polarities indicated by −), the action of motors is governed by the polarity of the filaments[11] and may result in contraction, extension or no sliding.

number of filament ends, which can trigger at these positions additional anillin-mediated filament sliding and accelerate the bundle contraction.

Molecular motor-driven sliding of filaments depends on the relative polarities of the filaments in the bundle[11] (Fig. 5d). In a disordered actin array, such as in the cytokinetic ring, myosin motors alone are thus equally likely to locally generate contractile or extensile forces. Additional mechanisms are needed to break the symmetry of the process, locally favouring the contractile forces to drive the overall net constriction of the ring. In this context, various factors are currently under debate (reviewed extensively in refs. [3,10,11]), such as the difference in behaviour of actin filaments under compressive and extensile forces[59,60], inhomogeneous distribution of myosin motors[19,61–63] or membrane anchoring of actin filaments[44]. Importantly, connectivity between actin filaments mediated by actin crosslinker α-actinin facilitates myosin-driven contraction of actin rings in vitro[9]. We here show that anillin-generated forces always act in the direction increasing the overlap length, contracting the actin bundle. Anillin will thus generate assisting forces in overlaps, which are locally contracted by myosin and resisting forces in overlaps, which are locally extended by myosin. Therefore, anillin-generated forces might constitute an element breaking the symmetry for myosin-dependent force generation in the cytokinetic ring and thus, in concert with myosin, drive its constriction. This notion is consistent with in vivo results showing that, in *Drosophila* embryos, lack of anillin results in a complete stall of myosin-driven contraction in the myosin-dependent phase of the ring constriction[13].

While the previous observations of the entropic cytoskeletal contractility were limited to two cytoskeletal filaments, here we demonstrate that diffusible cytoskeletal crosslinkers can generate forces in networks of higher complexity, such as bundles or rings, as hypothesised previously[64]. We show directly that actin crosslinkers can drive the contraction of actin filament bundles and can couple with actin filament disassembly to enhance this effect. We propose that this mechanism can (i) underpin the in vivo observed myosin-independent constriction of cytokinetic rings and (ii) break the symmetry of the randomly oriented actin-myosin system in the ring enabling myosin-dependent constriction of the ring. A recent finding that anillin promotes tensile forces in the apical actomyosin networks of *X. laevis* embryonal epithelium[65] suggests that analogous mechanism might also be employed in other actin structures. We propose that crosslinker-dependent contractility of filamentous networks is a fundamental mechanism readily available in actin-based cytoskeletal structures, likely contributing to various cellular movements.

Methods

Proteins. *Homo sapiens* anillin (GeneBank accession number: BC070066) cDNA was purchased (BC070066-seq-TCHS1003-GVO-TRI, BioCat GmbH Heidelberg, Germany), PCR amplified (for primers used see Supplementary Table 1) and ligated into an AscI-NotI-digested pOCC destination vector[66] containing a C-terminal GFP tag followed by a 3 C PreScission Protease cleavage site and a 6xHis-tag. The protein was expressed in SF9 insect cells using the opensource FlexiBAC baculovirus vector system[66]. The insect cells were harvested after 4 days by centrifugation at 300x*g* for 10 min at 4 °C in an Avanti J-26S ultracentrifuge (JLA-9.1000 rotor, Beckman Coulter). The cell pellet was resuspended in 5 ml ice-cold phosphate buffered saline (PBS) and stored at −80 °C for further use. For cell lysis, the insect cells were homogenised in 30 ml ice-cold His-Trap buffer (50 mM Na–phosphate buffer, pH 7.5, 5% glycerol, 300 mM KCl, 1 mM $MgCl_2$, 0.1% Tween-20, 10 mM BME and 0.1 mM ATP) supplemented with 30 mM imidazole, Protease Inhibitor Cocktail (cOmplete, EDTA free, Roche) and benzonase to the final concentration of 25 units/ml, and centrifuged at 45,000 × *g* for 60 min at 4 °C in the Avanti J-26S ultracentrifuge (JA-30.50Ti rotor, Beckman Coulter). The cleared cell lysate was incubated in a lysis buffer-equilibrated Ni-NTA column (HisPur Ni-NTA Superflow Agarose, Pierce, VWR) for 2 h at 4 °C on a rotator. The Ni-NTA column was washed with the wash buffer (His-Trap buffer supplemented with 60 mM imidazole) and the protein was eluted with the elution buffer (His-Trap buffer supplemented with 300 mM Imidazole). The fractions containing anillin-GFP were pooled, diluted 1:10 in the His-Trap buffer and the purification tag was cleaved overnight with 3 C PreScisson protease. The solution was reloaded onto a Ni-NTA column to further separate the cleaved protein from the 6xHis-tag. The protein was concentrated using an Amicon ultracentrifuge filter and flash-frozen in liquid nitrogen. Protein concentration was measured using Bradford assay (23236, Thermo Scientific) and microplate reader spectrometer (CLARIOstar, BMG Labtech, Germany).

The constitutively active (*R. norvegicus*, amino acids 1–430) recombinant C-terminal eGFP-hexa-histidine tagged kinesin-1 was expressed in *E. coli* BL21-CodonPlusVR (DE3)-RIPL (Stratagene) induced with 0.5 mM IPTG for 16 h at 18° C. Harvested cells were resuspended in buffer A (50 mM sodium phosphate buffer pH 7.5, 1 mM $MgCl_2$, 10 mM 2-mercaptoethanol, 300 mM NaCl, 0.1% Tween-20 w/vol, 10% glycerol w/vol, 30 mM imidazole and EDTA-free protease inhibitors (Roche)) and lysed using an EmulsiFlex high pressure homogeniser (Avestin) at 4 °

C. Crude lysate was centrifuged at 20,000x*g* at 4 °C and the supernatant was loaded on Ni-NTA resin (Qiagen). The resin was washed with buffer A containing 60 mM imidazole. The protein was eluted in buffer A containing 300 mM imidazole, snap frozen and stored in −80°C.

To determine whether there are residual traces of non-muscle myosin-II in the preparation of anillin-GFP expressed in SF9 insect cells (*S. frugiperda*, taxid 7108), we performed proteomic mass spectrometry analysis of the preparation. To the sample, we added 100 mM TEAB (triethylammonium bicarbonate) containing 2% SDC (sodium deoxycholate), 10 mM TCEP and 50 mM chloroacetamide to the final volume of 100 µl. Samples were lysed, reduced and alkylated in one step at 95 °C for 10 min and digested with 1 µg of trypsin at 37 °C overnight. After digestion, samples were acidified with TFA to 1% final concentration. SDC was removed by extraction to ethylacetate[67], and peptides were desalted using in-house made stage tips packed with C18 discs (Empore), according to Rappsilber[68].

Nano reversed-phase column (EASY-Spray column, 50 cm × 75 µm ID, PepMap C18, 2 µm particles, 100 Å pore size) was used for LC/MS analysis. Mobile phase buffer A was composed of water and 0.1% formic acid. Mobile phase B was composed of acetonitrile and 0.1% formic acid. Samples were loaded onto the trap column (Acclaim PepMap300, C18, 5 µm, 300 Å Wide Pore, 300 µm x 5 mm) at a flow rate of 15 µl/min. Loading buffer was composed of water, 2% acetonitrile and 0.1% trifluoroacetic acid. Peptides were eluted with a gradient of B from 4 to 35% over 60 min at a 300 nl/min flow rate. Eluting peptide cations were converted to gas-phase ions by electrospray ionisation and analysed on a Thermo Orbitrap Fusion (Q-OT- qIT, Thermo). Survey scans of peptide precursors from 350 to 1400 m/z were performed at 120 K resolution (200 m/z) with a 5×10^5 ion count target. Tandem MS was performed by isolation at 1,5 Th with the quadrupole, HCD fragmentation with a normalised collision energy of 30, and rapid scan MS analysis in the ion trap. The MS 2 ion count target was set to 10^4, and the max injection time was 35 ms. Only those precursors with charge state 2–6 were sampled for MS 2. The dynamic exclusion duration was set to 45 s with a 10 ppm tolerance around the selected precursor and its isotopes. Monoisotopic precursor selection was turned on. The instrument was run in top speed mode with 2 s cycles[69].

All data were analysed and quantified with the MaxQuant software (version 1.6.10.43)[70]. The false discovery rate (FDR) was set to 1% for both proteins and peptides, and we specified a minimum length of seven amino acids. The Andromeda search engine was used for the MS/MS spectra search against the Anillin sequence and database of expression system—*Spodoptera frugiperda* database (downloaded from Uniprot on July 2020, containing 26 645 entries). Precursor mass tolerance was set to 4.5 ppm, and MSMS match tolerance to 0.5 Da. Enzyme specificity was set as C-terminal to Arg and Lys, also allowing cleavage at proline bonds and a maximum of two missed cleavages. Carbamidomethylation of cysteine was selected as fixed modification and N-terminal protein acetylation and methionine oxidation as variable modifications. The 'match between runs' feature of MaxQuant was used to transfer identifications to other LC-MS/MS runs based on their masses and retention time (maximum deviation 0.7 min), and this was also used in quantification experiments. Data analysis was performed using Perseus 1.6.10.43 software[71]. To identify myosin-II among the proteins detected in the preparation, we performed Blast (blastp: protein vs. protein) of the amino acid sequence of *D. melanogaster* non-muscle myosin-II (uniprot Q99323 and flybase FBgn0265434) against the *S. frugiperda* genome and found GSSPFG00012506001-PA to be the protein with the highest identity (80% identities, 89% positives). Blasting the GSSPFG00012506001-PA sequence in UNIPROT against the Arthropoda database gave us the UniProt protein ID number A0A2H1WPK0, which was searched in the mass spectrometry results (please refer to Supplementary Table 2 for the relevant excerpt; the full table is included in the supplementary dataset).

Unlabelled rabbit muscle actin (AKL99, Cytoskeleton, Inc., USA) and rhodamine-labelled rabbit muscle actin (AR05, Cytoskeleton, Inc., USA) was resuspended to final concentration of 10 mg/ml in general actin buffer (GAB; 5 mM TRIS-HCl pH 8, 0.2 mM $CaCl_2$) supplemented with 0.2 mM ATP, 5% (w/v) sucrose and 1% (w/v) dextran. For experiments with fluorescently labelled non-stabilised filaments, rhodamine-labelled actin was diluted with the unlabelled actin above in a 1:10 ratio. The actin was then aliquoted, flash-frozen and stored in −80 °C. Actin filaments were polymerised by mixing the aliquoted actin (0.32 mg/ml final concentration) with polymerisation buffer (5 mM Tris-HCl pH 8.0, 0.2 mM $CaCl_2$, 50 mM KCl, 2 mM $MgCl_2$, 1 mM ATP) and, optionally, phalloidin (15 µM final concentration) for filament stabilisation and additional labelling. Biotinylated phalloidin (biotin-XX phalloidin, B7474, Thermo Fisher Scientific), fluorescence-labelled phalloidin (rhodamine-phalloidin, R415, Thermo Fisher Scientific, or Atto647 phalloidin, 65906, Sigma) or a 3:4 mixture of both were used in the experiments. Phalloidin-stabilised filaments were polymerised overnight at 4 °C and remained stable for at least 2 months. Non-stabilised filaments were grown in the polymerisation solution in the absence of phalloidin for ~30 min. They were employed from 5 min to 5 h after the polymerisation. For use in the assays, actin filaments were diluted in a ratio between 1:10 and 1:300, depending on the experiment.

Fluorescently-labelled microtubules were polymerised from 4 mg/ml porcine tubulin (80% unlabelled and 20% Alexa Fluor 647 NHS ester-labelled; Thermo Fisher Scientific) for 2 h at 37 °C in BRB80 (80 mM PIPES, 1 mM EGTA, 1 mM $MgCl_2$, pH 6.9) supplemented with 1 mM $MgCl_2$ and 1 mM GMPCPP (Jena Bioscience, Jena, Germany). The polymerised microtubules were centrifuged for 30 min at 18,000 x *g* in a Microfuge 18 Centrifuge (Beckman Coulter, Brea, CA) and the pellet was resuspended in BRB80 supplemented with 10 µM taxol (BRB80T).

Fluorescence imaging. The imaging was carried out in flow channels assembled from glass coverslips held together by parafilm spacers. Dichlorodimethylsilane-treated glass was passivated by 1% F127 pluronic copolymer (P2443, Sigma) for at least 30 min. Attachment of actin filaments stabilised by biotin-phalloidin was performed in channels that were incubated with an anti-biotin antibody solution (1 mg/ml in PBS, B3640, Sigma) prior to passivation. All channels were washed with 40 µl of the assay buffer upon passivation.

Actin filaments (either labelled by rhodamine or stabilised by rhodamine-phalloidin or Atto647 phalloidin) and anillin-GFP were imaged using an inverted microscope (Ti-E Eclipse, Nikon) equipped with 60x and 100×1.49 N.A. oil immersion objectives (CFI Apo TIRF and HP Apo TIRF, respectively, Nikon) in a TIRF (total internal refraction fluorescence) regime. The GFP and rhodamine fluorophores were sequentially excited by a laser on the wavelengths of 488 and 567 nm or 561 nm, respectively. FITC and TRITC fluorescence filter cubes were used, and the fluorescence was recorded using a CCD camera (iXon Ultra DU888, Andor Technology) or a CMOS camera (sCMOS ORCA 4.0 V2, Hamamatsu Photonics). The imaging setup was controlled by NIS Elements software (Nikon). The frame rate ranged between 1 frame per 10 ms to 1 frame per minute - time is indicated as time scale bars in kymographs, or as timestamps in time-lapse micrographs. The experiments were performed at room temperature.

Anillin binding and diffusion assay. Actin filaments stabilised by biotin-phalloidin were attached to anti-biotin antibodies on a glass coverslip. The channel was then washed with twice the channel volume of HEPES-based imaging buffer (20 mM HEPES, 2 mM $MgCl_2$, 1 mM EGTA, pH 7.2 KOH, 10 mM DTT, 20 mM D-glucose, 0.1 % Tween-20, 0.5 mg/ml Casein, 1 mM ATP, 0.22 mg/ml Glucose Oxidase and 0.02 mg/ml Catalase) before the HEPES-based imaging buffer with 0.12 nM anillin-GFP was flushed into the channel.

The oligomeric state of the anillin-GFP was determined from the fluorescence intensity of individual molecules diffusing on the biotin-immobilised actin filaments. This signal was compared with the fluorescence intensity of a single kinesin-1-GFP molecules immobilised on microtubules in the presence of AMP-PNP (in the absence of ATP). Kinesin-1-GFP was used as a standard due to its known dimeric state and therefore two-step photobleaching intensity profile[72]. Biotin-labelled microtubules were immobilised in the flow channel similarly to the actin filaments. The concentration of the kinesin-1-GFP was adjusted such that individual molecules bound to microtubules were detectable.

Kinetic properties of anillin-GFP unbinding from actin filaments was estimated from the temporal profile of the fluorescence intensity integrated along the contour of immobilised actin filaments upon the introduction, or washout of anillin-GFP, to or from, the imaging chamber. This process was repeated with various concentrations (from 0.12 to 12 nM) of the anillin-GFP in order to obtain a concentration profile. A complementary determination of the dissociation constant, K_d, was obtained from a concentration series (from 0.12 to 120 nM) of the steady-state densities of anillin-GFP on the actin filament.

Actin filament sliding assay. Biotin-phalloidin-stabilised actin filaments were introduced in the flow channel as described above. The channel was subsequently washed with the imaging buffer. Then, non-biotinylated actin filaments diluted in the imaging buffer containing 12 nM anillin-GFP were flushed into the channel. These filaments formed bundles with the biotin-phalloidin-stabilised filaments attached to the glass surface.

In an alternative experiment, ~1 µl of actin filaments followed by 15 µl of the imaging buffer with 0.1% methylcellulose (0.1 % w/v final concentration, 4000 cps at 2%, M0512, Sigma, supplemented with 30 mM NaCl final concentration) were first introduced into the flow channel. After initial imaging, the channel was flushed with imaging buffer containing 12 nM anillin-GFP and 0.1% methylcellulose. Filaments that remained in the channel after the flush were observed forming bundles. A control experiment was performed in the imaging buffer where ATP was replaced with 1 µM AMP-PNP, a non-hydrolysable analogue of ATP that prevents the enzymatic activity of molecular motors dependent on ATP-hydrolysis. Hexokinase (20 units/ml, Sigma H4502-1KU) was added to this buffer to remove any remnants of ATP. In this experiment, 0.5 mg/ml BSA (bovine serum albumin) was used instead of casein to block non-specific interactions.

Actin filament disassembly assay. Latrunculin-driven disassembly experiments were performed by introducing long unlabelled non-stabilised actin filaments into the flow channel, followed by short rhodamine-phalloidin stabilised actin filaments and 12 nM anillin-GFP in the GAB imaging buffer (GAB buffer with 10 mM DTT, 20 mM D-glucose, 0.1% Tween-20, 0.5 mg/ml Casein, 1 mM ATP, 0.8 mM PIPES, 0.22 mg/ml Glucose Oxidase and 0.02 mg/ml Catalase) supplemented with 0.1% methylcellulose and 80–200 nM latrunculin A (L12370, Thermo Fisher Scientific).

Actin ring constriction assay. For the ring constriction experiments, actin filaments were diluted 1:10 in the imaging buffer supplemented with 12 nM anillin-GFP and 0.1% methylcellulose. The final mixture was immediately transferred into the flow channel for imaging. We tested the robustness of the constriction under various buffer conditions. Ring constrictions were observed in both HEPES-based and GAB-based imaging buffers, with or without an additional supplement of 50 mM KCl. The data were pooled into two groups based on the properties of the actin filaments (phalloidin stabilised vs. non-stabilised) since the statistical testing (two-sample *t*-test at the significance level 0.05) did not reject the hypothesis that the constrictions rates within these groups come from distributions of equal means.

Optical trapping assay. Correlative force measurements and microscopy were performed on an optical tweezers setup equipped with confocal fluorescence imaging and microfluidic system (c-Trap, LUMICKS, The Netherlands). The continuous-wave optical tweezers were operated in a dual-trap regime. The force was measured by a position sensitive detector (PSD) in two dimensions on both beads with an acquisition rate of 50 kHz. The force was low-pass filtered to 30 Hz for storage and analysis by the controlling software (see below). The trap stiffness was calibrated using the thermal spectrum method (Scanary v. 3.3.0, LUMICKS, The Netherlands) under zero flow condition. The experiments were performed at room temperature. The force resolution of our experiment was around 100 fN at 30 Hz, with a theoretical limit of 34 fN for a typical trap stiffness of 6.55×10^8 pN/m and the corner frequency of 10.94 kHz. The system measured the distance between the beads by a built-in bright-field optical tracking with a resolution below 3 nm at 100 Hz.

The microspheres, actin filaments, imaging buffers and proteins were simultaneously flushed in the four-channel air-pressure driven microfluidic system in a laminar flow mode, ensuring that the solutions did not mix. The microfluidic system was passivated by BSA (0.1% in PBS) and F127 Pluronic no longer than 100 h before the experiment.

Actin filaments stabilised with rhodamine-phalloidin were attached to microspheres using barbed-end-binding protein gelsolin. Gelsolin-coated microspheres were prepared using a previously published protocol[35]. Briefly, the 1.01-µm-diameter carboxylated silica microspheres (SC04000, Bangs Beads) were activated by amine-reactive crosslinker chemistry using NHS (N-hydroxysuccinimide, 130672-5 G, Sigma) and functionalized by gelsolin (HPG6-A, Cytoskeleton).

To form the actin bundles (Fig. S2a), we modified a method described previously[35]. Two microspheres were captured in two traps. These microspheres were moved to the actin channel (actin filaments stabilised by rhodamine-phalloidin in the GAB imaging buffer) where ends of the filaments were attached to both of the microspheres. These constructs were then moved to the channel with 2xPBS imaging buffer (274 mM NaCl, 5.4 mM KCl, 3.6 mM KH_2HPO_4, 16 mM Na_2HPO_4, 0.1 mM $CaCl_2$, 10 mM DTT, 20 mM D-glucose, 0.1% Tween-20, 0.5 mg/ml Casein, 1 mM ATP, 0.22 mg/ml glucose oxidase and 0.02 mg/ml Catalase) where we used a flow reversal for transient sideways binding of filaments to the opposite microsphere. This construct was immediately moved to the channel with 12 nM anillin-GFP in the GAB imaging buffer, where gelsolin-dependent severing of the sideway attached filaments occurred, and the anillin-GFP formed the actin bundle at the same moment. The flow in the channels was then stopped, and the force response of the construct to stretching and relaxation was measured as follows.

The microspheres were moved relative to each other in the direction of the bundle using the Trap Stepper utility of the c-trap software (v. 3.6.1, LUMICKS, The Netherlands), with 100 nm step size and 3 µm/s speed. The distance of the microspheres was measured using bright-field microscopy, and the visualisation of the actin filaments and anillin-GFP was provided by built-in scanning confocal microscope with 488 and 561 nm excitation lasers. The number of actin filaments in the bundle was estimated from the intensity of the fluorescence signal of the rhodamine-phalloidin. The acquisition was controlled by Scanary software (v. 3.3.0, LUMICKS, The Netherlands).

The response of the bundle to a change of the anillin-GFP concentration was measured in a five-channel microfluidic system. Similarly, as above, the actin-anillin bundle was formed and pre-stretched in 12 nM anillin-GFP channel. The construct was then moved to the channel with 1 nM anillin-GFP concentration. Due to the different geometry of the channels, the experiment was performed in the flow of about 1 µl/min to prevent mixing of the low and the high concentration anillin-GFP channels. Control experiments were performed to exclude the effects of the flow on the accuracy of the force measurement (Fig. S2f). The acquisition was controlled by Bluelake software (v 1.5, LUMICKS, The Netherlands).

Image and data analysis. The oligomeric state of anillin-GFP and its diffusion behaviour were quantified using FIESTA[73] for the tracking of single molecules and @msdanalyzer MATLAB tool[74] for data analysis. The background signal was calculated from the areas directly adjacent to the actin filaments or microtubules and subtracted from the fluorescence intensities for quantification. The binding kinetics of anillin-GFP was estimated from the time constant of the first-order fit to the temporal step-response concentration profiles using MATLAB (Mathworks) procedures. These profiles were measured as the anillin-GFP fluorescence intensity integrated along the contour of immobilised actin filaments upon the introduction or washout of anillin-GFP to, or from the flow chamber (see Fig. 1c). The dissociation constant was calculated from the concentration profile of the steady-state fluorescence intensity of anillin-GFP along the contour of actin filaments using the Michaelis–Menten kinetics.

The lengths of the actin filament overlaps, as well as the circumferences of the rings, were measured manually in FiJi[75]. The circumferences of the rings were measured through the centre of the contour. Kymographs were generated using MultiKymograph plugin in FiJi or a custom-made MATLAB routine (circular kymograph in Fig. 4d). The data were analysed by self-written MATLAB scripts. Exponential decays in increasing and decreasing forms, $y = k \pm a\left(1 - e^{-\frac{t}{\tau}}\right)$ and $y = ae^{-\frac{t}{\tau}}$, respectively, were used to fit transient events. The overlaps between two filaments were identified as regions of approximately double the actin signal intensity as compared to single filaments. The velocities of sliding or disassembly were calculated as a change of the overlap length or filament length, respectively, with respect to time. Violin plots were generated using scripts by Bastian Bechtold. Boxplots were generated using MATLAB. Raw images were treated with automatic brightness/contrast enhancement routine (as implemented in FiJi) for presentation purposes. Temporal profiles of the force and distance observed in the optical trapping assay were analysed in MATLAB.

Reproducibility and data exclusion. All replication attempts that did not suffer from technical problems (such as improper channel passivation or malfunction of the instruments) were successful. All experiments were independently repeated at least three times, if not stated otherwise. The number of experiments, i.e. the number of individually filled channels in the case of microscopy assays and the number of constructs assembled de novo in the case of optical trapping assay, is indicated in the text.

Reporting Summary. Further information on research design is available in the Nature Research Reporting Summary linked to this article.

Data availability

Source Data are available with this paper. The dataset, including the source data underlying the figures, is deposited at figshare, https://doi.org/10.6084/m9.figshare.14725188. Further information and requests for reagents can be directed to and will be fulfilled by Zdenek Lansky (zdenek.lansky@ibt.cas.cz). Source data are provided with this paper.

Received: 6 January 2021; Accepted: 21 June 2021;
Published online: 28 July 2021

References

1. Schroeder, T. E. Cytokinesis: filaments in the cleavage furrow. *Exp. Cell Res.* **53**, 272–318 (1968).
2. Fujiwara, K. & Pollard, T. D. Fluorescent antibody localization of myosin in the cytoplasm, cleavage furrow, and mitotic spindle of human cells. *J. Cell Biol.* **71**, 848–875 (1976).
3. Pollard, T. D. & O'Shaughnessy, B. Molecular mechanism of cytokinesis. *Annu. Rev. Biochem.* **88**, 12.1–29 (2019).
4. DeKraker, C., Boucher, E. & Mandato, C. A. Regulation and assembly of actomyosin contractile rings in cytokinesis and cell repair. *Anat. Rec.* **301**, 2051–2066 (2018).
5. Mangione, M. C. & Gould, K. L. Molecular form and function of the cytokinetic ring. *J. Cell Sci.* **132**, jcs226928 (2019).
6. Huxley, H. E. & Hanson, J. Changes in the cross-striations of muscle during contraction and stretch and their structural interpretation. *Nature* **173**, 973–976 (1954).
7. Huxley, A. F. & Niedergerke, R. Structural changes in muscle during contraction. *Nature* **4412**, 971–973 (1954).
8. Kamasaki, T., Osumi, M. & Mabuchi, I. Three-dimensional arrangement of F-actin in the contractile ring of fission yeast. *J. Cell Biol.* **178**, 765–771 (2007).
9. Ennomani, H. et al. Architecture and connectivity govern actin network contractility. *Curr. Biol.* **26**, 616–626 (2016).
10. Murrell, M., Oakes, P. W., Lenz, M. & Gardel, M. L. Forcing cells into shape: the mechanics of actomyosin contractility. *Nat. Rev. Mol. Cell Biol.* **16**, 486–498 (2015).
11. Cheffings, T. H., Burroughs, N. J. & Balasubramanian, M. K. Actomyosin ring formation and tension generation in eukaryotic cytokinesis. *Curr. Biol.* **26**, R719–R737 (2016).
12. Davies, T. et al. High-resolution temporal analysis reveals a functional timeline for the molecular regulation of cytokinesis. *Dev. Cell* **30**, 209–223 (2014).
13. Xue, Z. & Sokac, A. M. Back-to-back mechanisms drive actomyosin ring closure during Drosophila embryo cleavage. *J. Cell Biol.* **215**, 335–344 (2016).
14. Hammarton, T. C. Who needs a contractile actomyosin ring? The plethora of alternative ways to divide a protozoan parasite. *Front. Cell. Infect. Microbiol.* **9**, 1–30 (2019).

15. Weirich, K. L. et al. Liquid behavior of cross-linked actin bundles. *Proc. Natl Acad. Sci. USA* **114**, 2131–2136 (2017).
16. Chen, S., Markovich, T. & MacKintosh, F. C. Motor-free contractility in active gels. *Phys. Rev. Lett.* **125**, 208101 (2020).
17. Descovich, C. P. et al. Crosslinkers both drive and brake cytoskeletal remodeling and furrowing in cytokinesis. *Mol. Biol. Cell* **29**, 622–631 (2018).
18. Bun, P., Dmitrieff, S., Belmonte, J. M., Nédélec, F. J. & Lénárt, P. A disassembly-driven mechanism explains F-actin-mediated chromosome transport in starfish oocytes. *Elife* **7**, 1–27 (2018).
19. Oelz, D. B., Rubinstein, B. Y. & Mogilner, A. A combination of actin treadmilling and cross-linking drives contraction of random actomyosin arrays. *Biophys. J.* **109**, 1818–1829 (2015).
20. Sun, S. X., Walcott, S. & Wolgemuth, C. W. Cytoskeletal cross-linking and bundling in motor-independent contraction. *Curr. Biol.* **20**, R649–R654 (2010).
21. Mendes Pinto, I., Rubinstein, B., Kucharavy, A., Unruh, J. R. & Li, R. Actin depolymerization drives actomyosin ring contraction during budding yeast cytokinesis. *Dev. Cell* **22**, 1247–1260 (2012).
22. Zhang, L. & Maddox, A. S. Anillin. *Curr. Biol.* **20**, 135–136 (2010).
23. Field, C. M. & Alberts, B. M. Anillin, a contractile ring protein that cycles from the nucleus to the cell cortex. *J. Cell Biol.* **131**, 165–178 (1995).
24. Paolo D'Avino, P. How to scaffold the contractile ring for a safe cytokinesis - lessons from Anillin-related proteins. *J. Cell Sci.* **122**, 1071–1079 (2009).
25. Piekny, A. J. & Maddox, A. S. The myriad roles of Anillin during cytokinesis. *Semin. Cell Dev. Biol.* **21**, 881–891 (2010).
26. Goldbach, P. et al. Stabilization of the actomyosin ring enables spermatocyte cytokinesis in Drosophila. *Mol. Biol. Cell* **21**, 1482–1493 (2010).
27. Oegema, K., Savoian, M. S., Mitchison, T. J. & Field, C. M. Functional analysis of a human homologue of the Drosophila actin binding protein anillin suggests a role in cytokinesis. *J. Cell Biol.* **150**, 539–551 (2000).
28. Straight, A. N., Field, C. M. & Mitchison, T. J. Anillin binds nonmuscle myosin II and regulates the contractile ring. *Mol. Biol. Cell* **16**, 1–13 (2005).
29. Zhao, W. M. & Fang, G. Anillin is a substrate of anaphase-promoting complex/cyclosome (APC/C) that controls spatial contractility of myosin during late cytokinesis. *J. Biol. Chem.* **280**, 33516–33524 (2005).
30. Naydenov, N. G., Koblinski, J. E. & Ivanov, A. I. Anillin is an emerging regulator of tumorigenesis, acting as a cortical cytoskeletal scaffold and a nuclear modulator of cancer cell differentiation. *Cell. Mol. Life Sci.* **78**, 621–633 (2020).
31. Matsuda, K., Sugawa, M., Yamagishi, M., Kodera, N. & Yajima, J. Visualizing dynamic actin cross-linking processes driven by the actin-binding protein anillin. *FEBS Lett.* **594**, 1237–1247 (2020).
32. Kueh, H., Brieher, W. & Mitchison, T. Dynamic stabilization of actin filaments. *Proc. Natl Acad. Sci. USA* **105**, 16531 (2008).
33. Mavrakis, M. et al. Septins promote F-actin ring formation by crosslinking actin filaments into curved bundles. *Nat. Cell Biol.* **16**, 322–334 (2014).
34. Lau, A. W. C., Prasad, A. & Dogic, Z. Condensation of isolated semi-flexible filaments driven by depletion interactions. *Europhys. Lett.* **87**, 48006 (2009).
35. Ward, A. et al. Solid friction between soft filaments. *Nat. Mater.* **14**, 583–588 (2015).
36. Hilitski, F. et al. Measuring cohesion between macromolecular filaments one pair at a time: depletion-induced microtubule bundling. *Phys. Rev. Lett.* **114**, 1–6 (2015).
37. Sanchez, T., Kulic, I. M. & Dogic, Z. Circularization, photomechanical switching, and a supercoiling transition of actin filaments. *Phys. Rev. Lett.* **104**, 65–68 (2010).
38. Lansky, Z. et al. Diffusible crosslinkers generate directed forces in microtubule networks. *Cell* **160**, 1159–1168 (2015).
39. Braun, M. et al. Changes in microtubule overlap length regulate kinesin-14-driven microtubule sliding. *Nat. Chem. Biol.* **13**, 1245–1252 (2017).
40. Odde, D. J. Mitosis, Diffusible Crosslinkers, and the ideal gas law. *Cell* **160**, 1041–1043 (2015).
41. Jananji, S. et al. Multimodal and polymorphic interactions between anillin and actin: their implications for cytokinesis. *J. Mol. Biol.* **429**, 715–731 (2017).
42. Braun, M., Diez, S. & Lansky, Z. Cytoskeletal organization through multivalent interactions. *J. Cell Sci.* **133**, jcs234393 (2020).
43. Norstrom, M. F., Smithback, P. A. & Rock, R. S. Unconventional processive mechanics of non-muscle myosin IIB. *J. Biol. Chem.* **285**, 26326–26334 (2010).
44. Stachowiak, M. R. et al. Mechanism of cytokinetic contractile ring constriction in fission yeast. *Dev. Cell* **29**, 547–561 (2014).
45. Bormuth, V., Varga, V., Howard, J. & Schäffer, E. Protein friction limits diffusive and directed movements of kinesin motors on microtubules. *Science* **325**, 870–873 (2007).
46. Wierenga, H. & Wolde, P. R. Ten. diffusible cross-linkers cause superexponential friction forces. *Phys. Rev. Lett.* **125**, 78101 (2020).
47. Walcott, S. & Sun, S. X. Active force generation in cross-linked filament bundles without motor proteins. *Phys. Rev. E Stat. Nonlin. Soft Matter Phys.* **82**, 1–4 (2010).
48. Walcott, S. & Sun, S. X. A mechanical model of actin stress fiber formation and substrate elasticity sensing in adherent cells. *Proc. Natl Acad. Sci. USA* **107**, 7757–7762 (2010).
49. Gittes, F., Mickey, B., Nettleton, J. & Howard, J. Flexural rigidity of microtubules and actin filaments measured from thermal fluctuations in shape. *J. Cell Biol.* **120**, 923–934 (1993).
50. Hickson, G. R. X. & O'Farrell, P. H. Anillin: a pivotal organizer of the cytokinetic machinery. *Biochem. Soc. Trans.* **36**, 439–441 (2008).
51. Mishra, M. et al. In vitro contraction of cytokinetic ring depends on myosin II but not on actin dynamics. *Nat. Cell Biol.* **15**, 853–859 (2013).
52. Kaji, N. et al. Cell cycle-associated changes in slingshot phosphatase activity and roles in cytokinesis in animal cells. *J. Biol. Chem.* **278**, 33450–33455 (2003).
53. Ono, K., Parast, M., Alberico, C., Benian, G. M. & Ono, S. Specific requirement for two ADF/cofilin isoforms in distinct actin-dependent processes in Caenorhabditis elegans. *J. Cell Sci.* **116**, 2073–2085 (2003).
54. Somma, M. P., Fasulo, B., Cenci, G., Cundari, E. & Gatti, M. Molecular dissection of cytokinesis by RNA interference in Drosophila cultured cells. *Mol. Biol. Cell* **13**, 2448–2460 (2002).
55. Akiyoshi, B. et al. Tension directly stabilizes reconstituted kinetochore-microtubule attachments. *Nature* **468**, 576–579 (2010).
56. Gestaut, D. R. et al. Phosphoregulation and depolymerization-driven movement of the Dam1 complex do not require ring formation. *Nat. Cell Biol.* **10**, 407–414 (2008).
57. Gardner, M. K. & Odde, D. J. Dam1 complexes go it alone on disassembling microtubules. *Nat. Cell Biol.* **10**, 379–381 (2008).
58. Hill, T. L. Theoretical problems related to the attachment of microtubules to kinetochores. *Proc. Natl Acad. Sci. USA* **82**, 4404–4408 (1985).
59. Lenz, M., Thoresen, T., Gardel, M. L. & Dinner, A. R. Contractile units in disordered actomyosin bundles arise from F-actin buckling. *Phys. Rev. Lett.* **108**, 1–5 (2012).
60. Murrell, M. P. & Gardel, M. L. F-actin buckling coordinates contractility and severing in a biomimetic actomyosin cortex. *Proc. Natl Acad. Sci. USA* **109**, 20820–20825 (2012).
61. Vavylonis, D., Wu, J. Q., Hao, S., O'Shaughnessy, B. & Pollard, T. D. Assembly mechanism of the contractile ring for cytokinesis by fission yeast. *Science* **319**, 97–100 (2008).
62. Kruse, K. & Jülicher, F. Actively contracting bundles of polar filaments. *Phys. Rev. Lett.* **85**, 1778–1781 (2000).
63. Liverpool, T. B. & Marchetti, M. C. Bridging the microscopic and the hydrodynamic in active filament solutions. *Europhys. Lett.* **69**, 846–852 (2005).
64. Braun, M., Lansky, Z., Hilitski, F., Dogic, Z. & Diez, S. Entropic forces drive contraction of cytoskeletal networks. *BioEssays* **38**, 474–481 (2016).
65. Arnold, T. R. et al. Anillin regulates epithelial cell mechanics by structuring the medial-apical actomyosin network. *Elife* **8**, e39065 (2019).
66. Lemaitre, R. P., Bogdanova, A., Borgonovo, B., Woodruff, J. B. & Drechsel, D. N. FlexiBAC: a versatile, open-source baculovirus vector system for protein expression, secretion, and proteolytic processing. *BMC Biotechnol.* **19**, 1–11 (2019).
67. Masuda, T., Tomita, M. & Ishihama, Y. Phase transfer surfactant-aided trypsin digestion for membrane proteome analysis. *J. Proteome Res.* **7**, 731–740 (2008).
68. Rappsilber, J., Mann, M. & Ishihama, Y. Protocol for micro-purification, enrichment, pre-fractionation and storage of peptides for proteomics using StageTips. *Nat. Protoc.* **2**, 1896–1906 (2007).
69. Hebert, A. S. et al. The one hour yeast proteome. *Mol. Cell. Proteom.* **13**, 339–347 (2014).
70. Cox, J. et al. Accurate proteome-wide label-free quantification by delayed normalization and maximal peptide ratio extraction, termed MaxLFQ. *Mol. Cell. Proteomics* **13**, 2513–2526 (2014).
71. Tyanova, S. et al. The Perseus computational platform for comprehensive analysis of (prote)omics data. *Nat. Methods* **13**, 731–740 (2016).
72. Hirokawa, N. et al. Submolecular domains of bovine brain kinesin identified by electron microscopy and monoclonal antibody decoration. *Cell* **56**, 867–878 (1989).
73. Ruhnow, F., Zwicker, D. & Diez, S. Tracking single particles and elongated filaments with nanometer precision. *Biophys. J.* **100**, 2820–2828 (2011).
74. Tarantino, N. et al. Tnf and il-1 exhibit distinct ubiquitin requirements for inducing NEMO-IKK supramolecular structures. *J. Cell Biol.* **204**, 231–245 (2014).
75. Schindelin, J. et al. Fiji: an open-source platform for biological-image analysis. *Nat. Methods* **9**, 676–682 (2012).

Acknowledgements

We thank Andrew Ward for hints on actin crosslinking in the optical tweezers, the Protein Facility of MPI-CBG, Yulia Bobrova and Veronika Vanova for technical support, Karel Harant and Pavel Talacko from the Laboratory of Mass Spectrometry, BIOCEV, Faculty of Science of the Charles University, for performing the proteomic and mass

spectrometric analysis, and Laurent Blanchoin for critical reading of the manuscript. This study was supported by the projects nos. 19-27477X to Z.L. and 20-04068 S to M.B. from the Czech Science Foundation, projects 'Introduction of New Research Methods to BIOCEV' (CZ.1.05/2.1.00/19.0390) and 'BIOCEV – Biotechnology and Biomedicine Centre of the Academy of Sciences and Charles University' (CZ.1.05/1.1.00/02.0109) from the European Regional Development Fund, and by the institutional support of the Czech Academy of Sciences (RVO: 86652036). We acknowledge CMS-Biocev (Biophysical techniques) supported by MEYS CR (LM2015043), the Centre of Imaging Methods core facility, Faculty of Science, Charles University, supported by the Czech-BioImaging through MEYS CR (LM2015062 and CZ.02.1.01/0.0/0.0/16_013/0001775), and the Structural mass spectrometry core facility of CIISB, Instruct-CZ Centre, supported by MEYS CR (LM2018127). D.J. and E.P. carried out this research partly as a project work at the Faculty of Biomedical Engineering of the Czech Technical University in Prague.

Author contributions

Conceptualisation, M.B. and Z.L.; Methodology, O.K., M.B. and Z.L.; Investigation, O.K., V.S., D.J., S.H.D. and E.P.; Formal analysis, O.K., D.J., E.P. and V.S.; Data curation, O.K., D.J., V.S. and S.H.D.; Validation, O.K.; Resources, O.K., E.Z. and S.D.; Writing, O.K., M.B. and Z.L.; Visualisation, O.K.; Supervision, M.B. and Z.L.; Funding acquisition, M.B. and Z.L.

Competing interests

The authors declare no competing interests.

Additional information

Supplementary information The online version contains supplementary material available at https://doi.org/10.1038/s41467-021-24474-1.

Correspondence and requests for materials should be addressed to M.B. or Z.L.

Peer review information *Nature Communications* thanks Rae Robertson-Anderson and other, anonymous, reviewers for their contributions to the peer review of this work. Peer review reports are available.